University of New Orleans Theses and Dissertations

Dissertations and Theses

5-21-2005

Fabrication of Three-Dimensionally Ordered Nanostructured Materials Through Colloidal Crystal Templating

Lianbin Xu
University of New Orleans

Follow this and additional works at: https://scholarworks.uno.edu/td

FABRICATION OF THREE-DIMENSIONALLY ORDERED NANOSTRUCTURED
MATERIALS THROUGH COLLOIDAL CRYSTAL TEMPLATING

A Dissertation

Submitted to the Graduate Faculty of the
University of New Orleans
in partial fulfillment of the
requirements for the degree of

Doctor of Philosophy
in
The Department of Chemistry

by

Lianbin Xu

B.S., Nankai University, 1991
M.S., Peking University, 1994
M.S., University of New Orleans, 2003

May 2004

ACKNOWLEDGEMENTS

TABLE OF CONTENTS

LIST OF TABLES

LIST OF FIGURES

ABSTRACT

The void spaces in colloidal crystals (opals, three-dimensional (3D) close-packed arrays of silica nanospheres) and their replicas are used as templates in the fabrication of new nanostructured materials. 3D ordered nanomeshes and nanosphere arrays are readily obtained by chemical and/or electrochemical methods.

Using silica opal templates, metals or polymers are infiltrated into the interstices between the silica nanospheres. Subsequent dissolution of the opals with HF solution produces open 3D mesh structures. Metal (such as Ni, Co, Fe, Pd, Au, Ag, and Cu) and conductive polymer (such as polyaniline) meshes are obtained by electrochemical deposition approach, while the nonconductive polymer (such as poly(methyl methacrylate) (PMMA)) meshes are synthesized by chemical polymerization method.

Some new types of meshes are fabricated by the conversion of metal meshes and polymer meshes. NiO meshes are formed by oxidizing Ni meshes in the air. The NiO meshes exhibit higher volume occupation fraction than Ni meshes and the nanocrystalline sizes of NiO particles can be adjusted by the oxidation temperature. Due to the mechanical flexibility of polymer meshes, the compression of PMMA meshes produces deformed PMMA meshes which contain oblate pores.

These meshes can be again served as templates to prepare new types of colloidal crystals (nanosphere arrays) and specific nanocomposites. By the use of poorly

conductive NiO mesh or PMMA mesh arrays as templates, 3D periodic metal nanosphere arrays, such as those of Ni, Co, Au and Pd, are readily fabricated by the electrodeposition method. Metal/NiO or Metal/PMMA composites can also be obtained if the templates are left intact.

The magnetic behavior of metal (such as Ni and Co) meshes and sphere arrays has been investigated. These nanoscale arrays show significantly enhanced coercivities compared with bulk metals, due to the size effect of the nanometer dimensions of the components in meshes and sphere arrays. Angle-dependent magnetic properties of Ni and Co sphere array membranes exhibit out-of-plane anisotropy.

CHAPTER 1

INTRODUCTION

1.1 Template-Directed Synthesis

The "template-directed synthesis" method involves synthesizing a desired material within the pores of a host structure, such as a nanoporous membrane, and presents a number of interesting and useful characteristics. First, this method is a very general approach to the manufacturing of nanostructured materials and can be used to prepare different shapes like tubes, wires and meshes composed of different materials like metals, semiconductors, ceramics, carbon, polymers, and other materials. Also, this approach is promising because it can be used to fabricate nanostructures with very small sizes, which is still difficult to form with a conventional lithographic process. Furthermore, the nanostructured materials prepared in this way can be dimension-controllable and well-defined. Finally, the nanostructures like tubes, wires and meshes synthesized within the pores can be freed from the template membrane and collected.

Template-directed method was developed by Possin, who reported the fabrication of metal nanowires as small as 40 nm in diameter in etched particle tracks which was formed in mica in 1970.[1] Later, Williams and Giordano refined Possin's method and they described the preparation of 8 nm diameter metal nanowires in 1984.[2] Since late 1980s, due to the extensive interest in nanomaterials, Martin and other researchers have fabricated nanostructured wires and tubes by using porous

membranes with one-dimensional (1D) channels as a template.[3-9] The widely-used

templates containing 1D nanoholes are anodic alumina membranes and track-etched

polymeric membranes. Figure 1.1a shows the model for a porous alumina membrane

containing 1D nanoholes. Figure 1.1b reveals a transmission electron microscopy

(TEM) image of a cutout of a thin membrane surface with *ca.* 50 nm pores.[10] The

nanoholes in porous alumina membrane can be infiltrated with other materials like

metals, ceramics and polymers, and freestanding nanowires or nanotubes can be

conveniently obtained by etching away the alumina template with strong bases or

acids. A lot of other nanoporous materials like nanochannel array glass membrane,[11]

mesoporous zeolite membrane[9,12,13] and cleaved graphite surface[14] have also been used

as templates to prepare nanowires and nanotubes.

Recently, the template-directed synthesis method has been extended to

fabricate three-dimensionally (3D) ordered nanostructured materials by the use of

opals (also called colloidal crystals) and inverse opals (also called meshes or

macroporous materials) as templates.[15-23] The colloidal crystals consist of 3D ordered

silica or latex spheres. A variety of materials like metals, ceramics, polymers, carbon,

and silicon can be infiltrated into the void spaces between the colloidal spheres. The

original colloidal spheres are subsequently removed, leaving behind a new type of

materials, so called inverse opals, macroporous materials or meshes, whose pores

preserve the long-range periodic structure of the original colloidal crystals. Figure 2a

and 2b show the model of opal[24] and inverse opal,[25] respectively, and Figure 2c shows

the schematic of the replication of colloidal crystal structure into porous materials.

The inverse opal can be further used as a template to fabricate 3D ordered nanosphere

arrays. These 3D ordered arrays of nanospheres and their replicas (porous networks)

a)

b)

100 nm
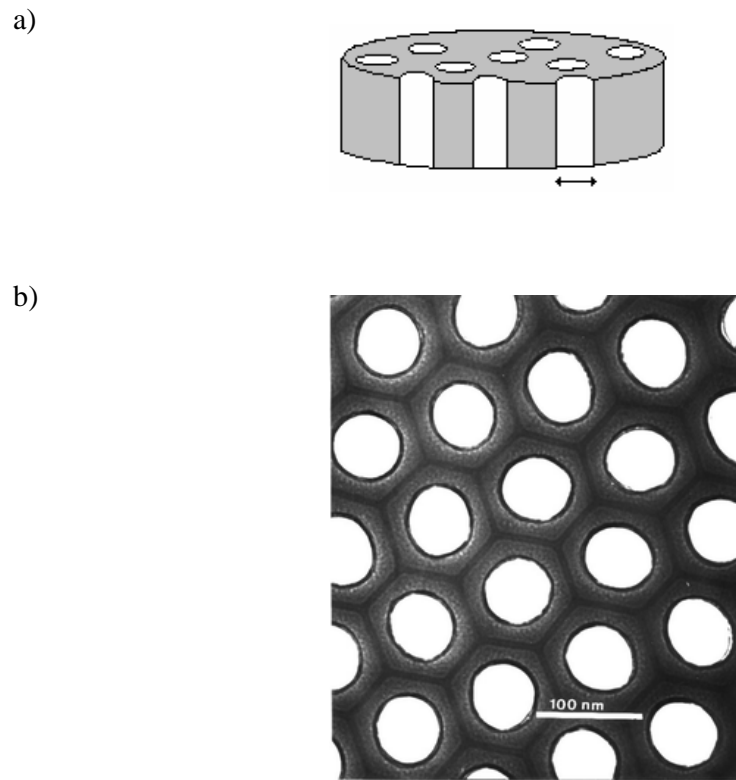
Figure 1.1 a) Model of porous alumina membrane containing one-dimensional
nanoholes, b) TEM image of a thin alumina membrane ion milled showing
hexagonally ordered, *ca.* 50 nm pores (adapted from Ref. 10).

a)

b)

c)

opal   infiltrated opal   inverse opal
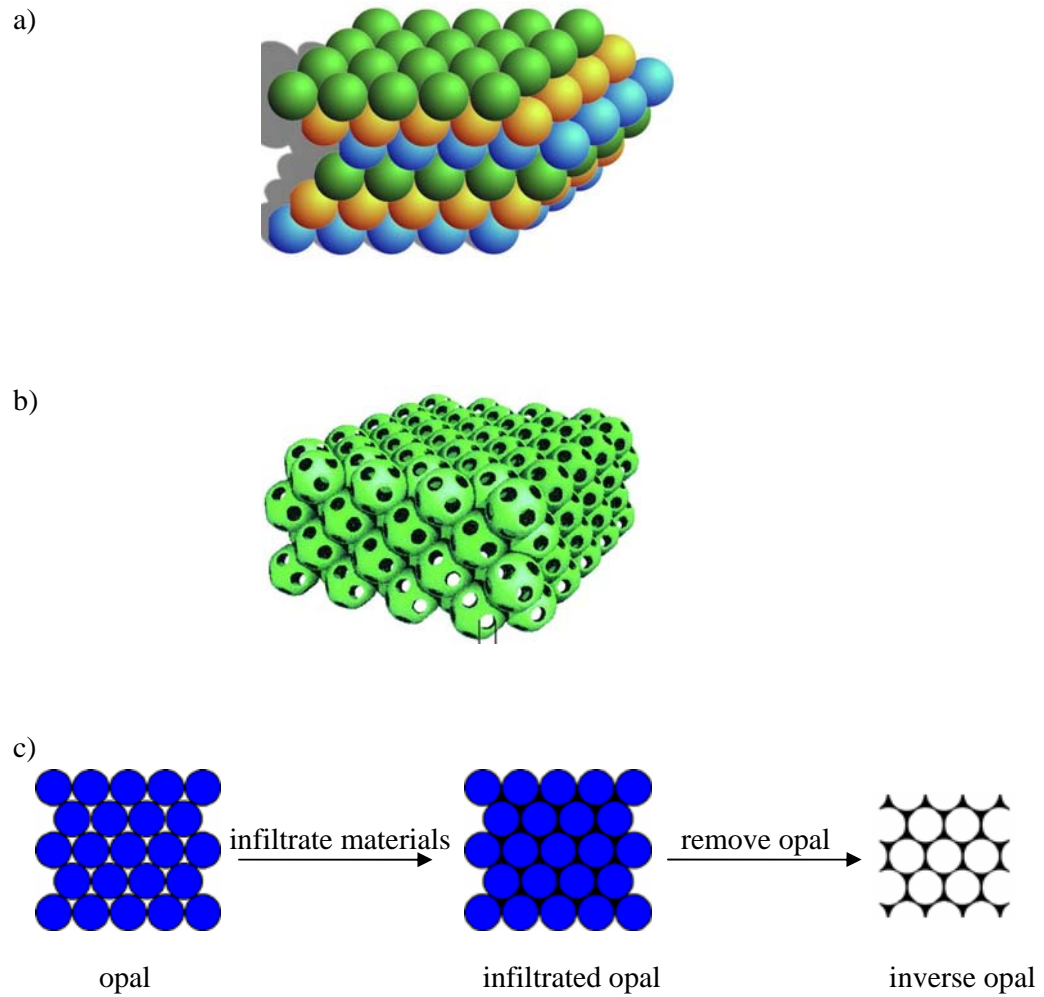
Figure 1.2 a) Model of opal consisting of three-dimensionally ordered colloidal
              spheres (adapted from Ref. 24), b) model of inverse opal having three-
              dimensionally ordered porous structure (adapted from Ref. 25),
              c) schematic of the replication of colloidal crystal structure into porous
              materials.

are of great interest for applications in a variety of areas, including photonics,

magnetics, catalysis, separations, and sensing.[15-23, 26]

1.2 Colloidal Crystals

1.2.1 Synthesis of Colloidal Crystals

Natural opals are precious gems formed in either a sedimentary or a volcanic

environment and are composed of a cubic close packed (ccp) arrangement of

amorphous silica spheres. The spheres may range in size between 150 and 900 nm,

but have a narrow size distribution (around 5%). The opals (colloidal crystals) can

also be synthesized from monodisperse colloids through self-assembly. Figure 1.3

shows a partial list of the colloidal systems and their typical range of critical

dimensions.[27]

Silica spheres and latex polymer spheres, mainly polystyrene (PS) and

poly(methyl methacrylate) (PMMA), are two major types of colloids used for the

colloidal crystal assembly due to their high monodispersity and relative cheapness.

Monodisperse silica colloids are usually prepared by the method developed by Stöber

et al.[28] They hydrolyzed a dilute solution of tetraethyl orthosilicate (TEOS) in ethanol

at high pH and produced uniform silica spheres with diameters ranging from 50 nm to

2 µm by adjusting the temperature, pH and concentrations of the reactants. Uniform

latex spheres like PS and PMMA spheres are mainly synthesized by emulsion

polymerization method.[29-31] Some monodisperse colloidal spheres can also be

commercially obtained from a number of companies, such as Nissan Chemical

Industries, Duke Scientific, and Alfa Asear.[16]

Colloidal crystals are formed by assembling the silica or latex spheres into

close-packed structures. A diversity of methods, including gravity sedimentation,
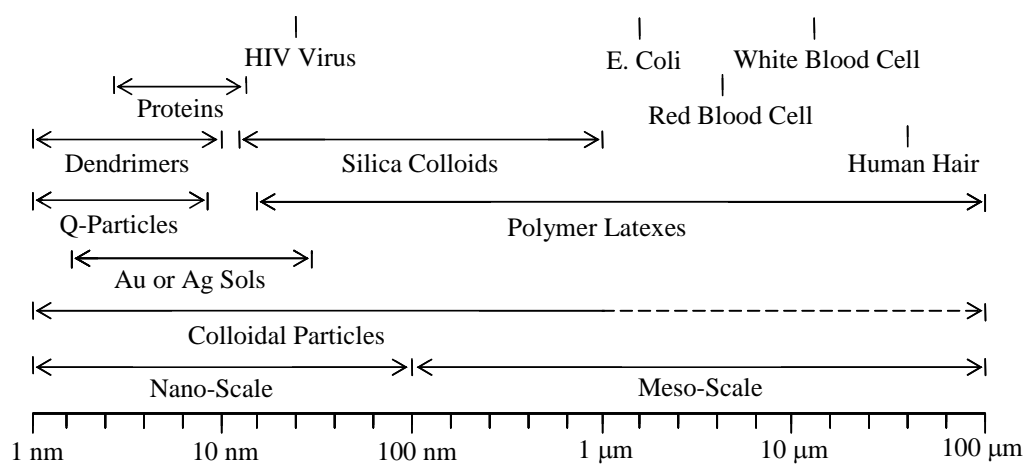
Figure 1.3 A list of some representative colloidal systems and their typical ranges of dimensions (adapted from Ref. 27).

centrifugation, vertical deposition, templated deposition, electrophoresis, patterning, controlled drying, and melt compression have been developed to construct close-packed silica or latex spheres.[16,23,32,33]

The simplest but most commonly used method for colloidal assembly is gravity sedimentation.[34-37] Figure 1.4 shows a schematic view for making colloidal crystals by gravity sedimentation. Dilute suspensions (~ 1 wt.%) of colloids having a dispersion smaller than 5% are placed in a container, then sedimentation occurs driven by gravity. The sedimentation method produces thick opal and the success of this method depends on tight control over several parameters such as the size and density of the colloidal spheres, as well as the rate of sedimentation. The colloidal spheres can always settle completely to the bottom of the container when the size and density of these spheres are sufficiently high. When the sphere size is too small, the deposition rate is small, too, and no sedimentation occurs in a reasonable time; but if the spheres are too large or the sedimentation rate is too fast, bad-quality assembly is achieved. Monodisperse silica colloids are most commonly applied in sedimentation due to the high density of amorphous silica. A major disadvantage of the sedimentation method is that it has very little control over the morphology of the top surface and the number of layers of the 3D crystalline arrays. Also sedimentation relying solely on gravity is a very slow process, typically requiring weeks or months, especially if sphere diameters are smaller than 300 nm.

Recently, Jiang *et al.* developed a good and easy method, so called vertical deposition, to form thin film colloidal crystals.[38] They placed a glass slide into a scintillation vial containing silica alcosol and covered the vial with a crystallizing dish to allow the slow evaporation of solvent. Closed-packed layers of silica spheres were then formed on the glass slide. The thickness of the layer deposited depends on the
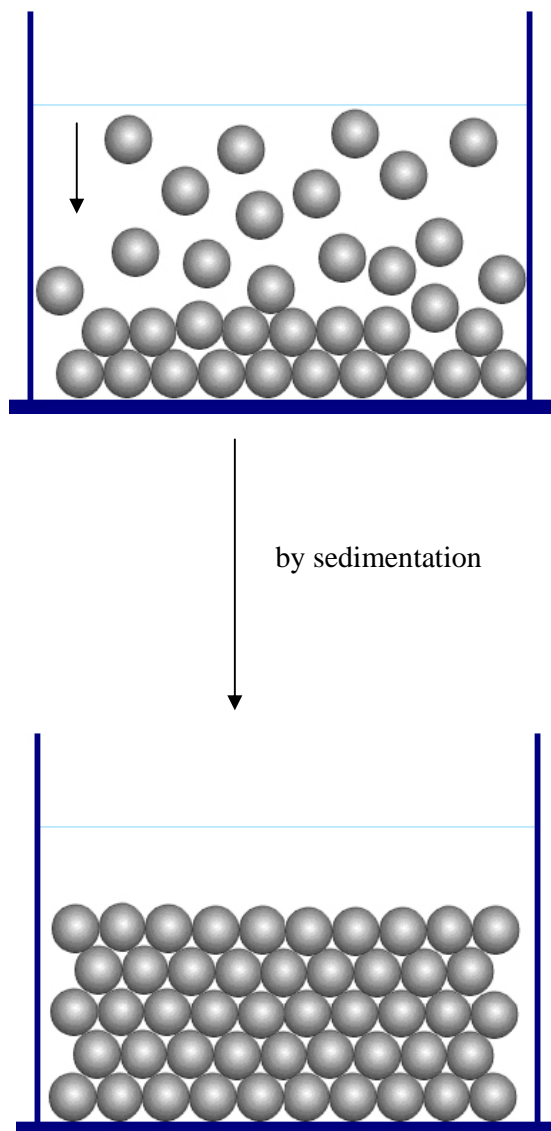
Figure 1.4 Schematic for making three-dimensionally ordered silica or latex spheres by gravity sedimentation.

colloidal concentration and sphere diameter. Thick films up to hundreds of layers could be obtained by multiple dip coating and drying cycles.

The colloidal crystals just after assembly contain a considerable amount of water, both physically and chemically bound, and the spheres in the colloidal crystals are held just by relatively weak forces. For later applications creaking or disrupting the structure is always a problem. Thermal treatment can be applied to enhance the mechanical properties of colloidal crystals. Usually, silica opals are sintered by heat treatment in air (drying at 100-150°C)[39] or thermal annealing (700-750°C),[25] and latex opals can be strengthened by heating above their glass transition temperature (T_g).[40]

1.2.2 Structure of Opal

Usually opals have a cubic-close-packed (ccp) structure with a face-centered-cubic (fcc) lattice. The fcc structure has a preference over the hexagonal-close-packed (hcp) structure due to a slight difference in the energy of the colloidal spheres stacking in the fcc and hcp arrangement as described in the calculations by Woodcock.[41,42] In fcc crystals, the stacking sequence for spheres follows ABCABC, and in hcp it is ABABAB.[43,44] In both structures, the spheres take up a volume fraction of 0.7405.[45] Since the opals undergo a thermal treatment after assembly, which leads to the formation of small necks between the spheres, the filling fraction for spheres slightly increases.[25]

In fcc structure, there are two types of interstice (or void), namely tetrahedral interstice and octahedral interstice, between the spheres.[43,44] Figure 1.5 shows the structure of voids in fcc lattice.[46] The dimensions for the octahedral interstice, tetrahedral interstice and the interconnect minimum (triangular interstice between three spheres contacted to each other) are 0.414D, 0.225D, and 0.155D (D is the sphere diameter) in diameter, respectively.[43,44]
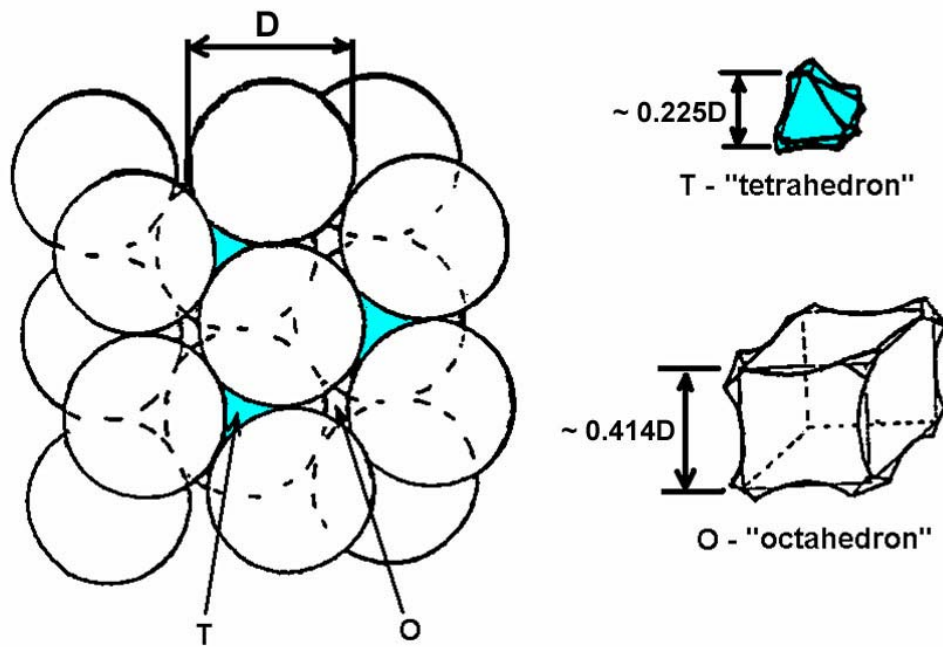
Figure 1.5 Structure of voids in fcc opal (adapted from Ref. 46).

1.3 Infiltration Methods

Three-dimensional nanoscale porous structure (mesh, or inverse opal) can be fabricated by infiltrating materials into the voids between the spheres in opal, and then extracting the opal template by HF solution (for silica opals), or organic solvents (such as dichloromethane, toluene, and acetone) and calcinations (for latex opals). Since the late 1990's, a variety of methods have been employed to fabricate inverse opals. The most popular are electrodeposition, sol-gel hydrolysis, chemical polymerization, and chemical vapor deposition (CVD) techniques.

Electrodeposition: First, a layer of metal like Cu is deposited on one-side of opal pieces or opals are deposited on conducting substrates like conductive ITO (indium tin oxide) glass to make opal template working electrodes. Then the opal template electrodes are immersed in plating solutions versus a counter electrode like Pt wire, and materials grow inside opals galvanostatically or potentiostatically. A number of inverse opals, such as metal,[47-52] semiconductor,[53-58] and conductive polymer[59-61] meshes have been fabricated by electrodeposition. Electrodeposition is an effective method for producing the inverse opals, due to the nearly complete filling of the channels of opal templates and easy control of the extent of materials growth.

Sol-Gel Hydrolysis: Opals are soaked in alcoholic solutions containing alkoxide precursors. The precursors are penetrated into the voids of opals through capillary force. Then the opals filled with alkoxide precursors are allowed for hydrolysis and then drying. The penetration/reaction/drying process is repeated for many times to ensure the voids of opals are sufficiently filled. A wide range of porous oxides, such as SiO_2,[30,62-67] GeO_2,[68] metal oxides (e.g. TiO_2, ZrO_2, Al_2O_3, SnO_2, Eu_2O_3, Nd_2O_3, and Sm_2O_3),[69-87] binary oxides (e.g. $BaTiO_3$,[88] and $PbTiO_3$[89]) and multinary oxides (e.g. $(Pb,La)(Zr,Ti)O_3$[90] have been obtained by this method.

Chemical Polymerization: Opals are filled with a liquid monomer containing small amount of initiator, and polymerization is carried out by heating or ultraviolet (UV) illumination. This method produces high-quality polymer meshes, including polyurethane,[91-94] poly(divinylbenzene) (PDVB),[95,96] poly(ethyleneglycol dimethacrylate) (PEDMA),[95] poly(acrylate methacrylate) (PAM),[93] poly(methyl methacrylate) (PMMA),[94,97] polystyrene (PS),[94,98] poly(*p*-phenylenevinylene) (PPV),[99] and epoxy resin.[100]

Chemical Vapor Deposition: Opals are filled with gaseous precursors and deposition is performed by thermal treatment. This technique can produce dense inverse opal structures by virtue of the gaseous precursors' ability to penetrate the pore network of colloidal crystals. The fabrications of carbon,[25] SnS_2,[101,102] Pt and Pt-Pd alloy[103] inverse opals and technologically important Si[104-106] and Ge[107] inverse have been reported.

Other approaches for inverse opal formation include nanoparticle infiltration (e.g. metals,[108-110] CdS,[111] SiO_2,[112] and TiO_2[112]), salt-precipitation and chemical conversion (e.g. metal oxides,[113,114] and Sb_2S_3[115]), electroless deposition (e.g. metals),[116] polymerization and pyrolysis (e.g. carbon),[25,117-121] melt infiltration (e.g. low melting-point metals, semi-metals, and alloys),[122-124] adsorption and chemical conversion (e.g. metals,[125] $Sr_{0.5}Sm_{0.5}CoO_3$[126]), oxidation or reduction (e.g. NiO,[127,128] metals,[113,129] alloys,[130] and Ge[68]), electrophoresis (e.g. SiO_2 and TiO_2),[131] solvothermal synthesis (e.g. CdS),[132] spraying (e.g. metals and Si),[133] and atomic layer deposition (e.g. tungsten nitride).[134] These methods can also be conveniently extended to the fabrication of new types of colloidal crystals (three-dimensionally periodic sphere arrays) by using inverse opals as templates.[97,127,128,135,136]

1.5 Potential Applications

So far, the area of inverse opals and their replicas is relatively new, and most of the studies have concentrated on the fabrication and basic characterization of these new types of materials. However, due to their unique structures with 3D periodicity, inverse opals (nanoscale porous networks) and their replicas have promising applications in a number of fields, including photonics, magnetics, separations, catalysis, etc.

Photonics: Probably the most important application of colloidal crystals and inverse opals is using as photonics crystals. Photonic crystals (also called photonic band gap materials) are structures in which the refractive index is a periodic function in space.[137-142] In the very same way as for electrons in a periodic potential, forbidden bands can occur for electromagnetic waves in a periodic refractive index structure. A complete 3D photonic band gap material is a material in which light in a band of frequencies cannot propagate whatever the polarization or the direction of propagation. In 3D photonic crystals, diamond and fcc structures are the representative sturtures. Materials with fcc structures (such as opals) receive considerable attention due to their easy and low cost fabrication. However, fcc opals don't have a complete photonic band gap because of their low refractive indices (silica ~ 1.4, PS ~ 1.5, PMMA ~ 1.5). In order to open a complete band gap, the dielectric contrast or refractive index between low and high dielectric regions must be sufficiently high (refractive index ratio > 2.85).[143] Inverse opals also have fcc structures and it is possible to obtain high dielectric contrast inverse opals by filling high refractive index materials such as Si and Ge (refractive index: Si ~ 3.8, Ge ~ 4.1) in the voids of opals and then extracting the opals. Such materials (Si and Ge meshes) showing full photonic band gap in near-IR region have recently been successfully fabricated.[104-107] Many applications of

photonic crystals lie in areas of waveguides, microcavity lasers, dielectric mirrors, optical chips, etc.[137-142]

Magnetics: Colloidal template synthesis offers the potential of a low-cost preparation method for nanoscale patterned magnetic media.[144] The 3D magnetic metal (such as Fe, Co, Ni, $Ni_{50}Fe_{50}$ alloy) meshes and sphere arrays have significantly enhanced coercivity than related bulk materials, due to their periodic nanoscale structures.[47,52,97,144] A notable advantage is that these materials are stable with no supports or surfactants needed. Also, it is found that Co/CoO mesh systems show interesting exchanging bias phenomena,[145] i.e. the shift of the hysteresis loop of the ferromagnet along the field axis caused by the exchange coupling of ferromagnetic and antiferromagnetic films across their common interface.[146]

Separations: The pore size of inverse opals can range from < 100 nm to > 1000 nm, depending on the original opal templates. The uniformity and the interconnection of the close-packed pores make some of these materials usable for applications in separation, filtration and immobilization.[93]

Catalysis: The applications in catalysis benefit from the open porous structures and high surface areas of these materials. The large enough pores allow rapid mass transport, while the high surface area is good for using as support for catalytically active species. Promising directions are the synthesis of silica inverse opals with zeolitic micro- or mesoporous frameworks and doping and modification of the surfaces of the pore walls.[30,64,147,148]

Other potential applications include sensors (gas sensors,[85] biosensors,[98] and pH sensors[149]), porous electrodes,[150] solar cells,[151] and thermoelectric materials.[152] Further developments are expected for this exciting new area in the near future.

1.4 Dissertation Structure

This dissertation consists of five chapters. Chapter 2 describes the electrochemical preparation of metal meshes by the use of silica opals as templates. Microstructures and magnetic characterization of the metal meshes are discussed. In Chapter 3, the fabrications of NiO meshes, conductive polyaniline meshes, nonconductive PMMA meshes and compressed PMMA meshes are presented. In Chapter 4, the two-step template synthesis of metal sphere arrays (metallic colloidal crystals) is presented. Opals are used as the first-step templates for the fabrication of inverse opals (NiO mesh and PMMA mesh). Poorly-conductive inverse opals are used as the further templates to grow metal sphere arrays by electrodeposition. Angle-dependent magnetic properties of Ni and Co sphere arrays are discussed. The last chapter is a summary of the work presented in this dissertation.

CHAPTER 2

ELECTRODEPOSITION AND CHARACTERIZATION OF

ORDERED NANOSCALE METAL MESHES

2.1 Introduction

Porous metals that are three-dimensionally (3D) periodic in structure have gained extensive attention because of their wide range of applications, including their use as photonic crystals,[153-158] nano-patterned magnets,[144,159] electrochemical sensors,[160] and surface-enhanced Raman spectroscopy (SERS) substrates.[161] Traditionally, such ordered and hierarchical metals are fabricated by lithography methods. However, the application of lithography methods is limited due to the cost and difficulty to obtain nanoscale materials.[140] Recently, colloidal crystal template methods have been developed to fabricate 3D porous materials with submicron to nanometer scale.

By the use of opals as templates, metals can be infiltrated into the void spaces between close-packed silica or latex spheres in opals. Subsequent removal of the opal templates produces open 3D mesh structures. Using the opal template method, the dimensions of the pores can be easily controlled by changing the size of the silica or latex spheres in the templates.

A number of techniques, such as nanoparticle infiltration,[108-110] reduction of oxide meshes,[113,129,130] melt infiltration,[122-124] adsorption and reduction,[125] spraying,[133] chemical vapor deposition (CVD),[103] electroless deposition,[116] and

electrodeposition[47-52,162,163] have been applied to infiltrate metals into opal templates. Among these methods, the electrodeposition technique is an effective route to fill metals in the complex porous channels of opal templates since electrodeposition occurs from the electrode surface out through the overlying template and the extent of growth can be controlled by varying the deposition conditions such as current, potential and time. Also, electrodeposition gives a high density in-filling of the interstices between the spheres of opal template and results in true "volume templating" of the structure, rather than surface templating of the material around the surface of the template spheres.

Previously, electrodeposition was applied to fabricate nanowires and nanotubes by the use of membranes with one-dimensional (1D) pore structures as templates.[6] Later, the electrochemical deposition technique was extended to synthesize 3D porous structures (meshes) using opal templates. Braun *et al.*[53] first described the fabrication of CdS and CdSe meshes by electrodeposition and subsequently the electrochemical synthesis of metal meshes was reported by a couple of groups.[47-49] Our group was one of the first to fabricate 3D metal meshes by electrodeposition.[47] In this chapter, we describe the electrochemical preparation, microstructural and magnetic characterization of 3D periodical nanoscale metal meshes.

2.2 Experimental Section

2.2.1 Materials

All solvents and chemicals were of reagent quality and were used as received. $CoSO_4 \cdot 7H_2O$ (99.998%, Aldrich), H_3BO_3 (99.8%, EM Science), NaCl (100.2%, J. T. Baker), $FeSO_4 \cdot 7H_2O$ (99.6%, J. T. Baker), L-ascorbic acid (99%, Aldrich),

$CuSO_4 \cdot 5H_2O$ (99.16%, Mallinckrodt), HF solution (48%, Aldrich), acetone (99.7%, Mallinckrodt).

2.2.2 Synthetic Opals

Synthetic opals were obtained from our collaborators Prof. Ray H. Baughman and Anvar A. Zakhidov at University of Texas at Dallas. Silica membranes (opal) were prepared by published methods.[164-166] Silica spheres with a diameter of *ca.* 290 nm, 220 nm and 180 nm diameters were initially prepared from hydrolysis of tetraethoxysilane (TEOS). The spheres were then formed into close-packed lattices through a sedimentation process over several months. This precipitate was then sintered at 120°C for 2 days and then 750°C for 4 hours, producing a robust opalescent piece that could be readily cut into smaller sections.

2.2.3 Fabrication of Opal Membrane Electrode

Figure 2.1 shows the fabrication procedure for the opal membrane electrode. Electrodes were formed from the opal pieces (typically 7 x 10 x 1.5 mm) by first depositing about 1.0 µm thick gold film on one side of the piece by magnetron sputtering. A length of wire was attached to the gold backing with silver paste (Ted Pella, Inc.) and the gold/wire side of the electrode, as well as the edges, was sealed off with insulating glue (Scotch Super Strength, 3M).

2.3.4 Synthesis of Metal Meshes (Inverse Opals)

2.2.4.1 Electroplating Solutions

The commercial *Ni* (Nickel Sulfamate RTU, $Ni(H_2NSO_3)_2$ solution, pH ~ 4.0), *Pd* (Pallaspeed VHS, 3.97% $(NH_2CH_2CH_2NH_2)_2PdSO_4$ solution, containing 5.3 g/liter palladium, pH ~ 6.0), *Au* (Orotemp 24 RTU, $KAu(CN)_2$ solution, containing 8.2 g/liter gold, pH ~ 8.0), and *Ag* (1025 silver process, $KAg(CN)_2$ solution, containing 30 g/liter silver, pH ~ 12.0) electroplating solutions were obtained from Technic Inc.

opal

Sputter Deposit
Au film

Au film

Make Electric
Contact with Ag
Paste and Cu Wire

Cover Au Film with
Insulating Glue

insulating glue

Cu wire
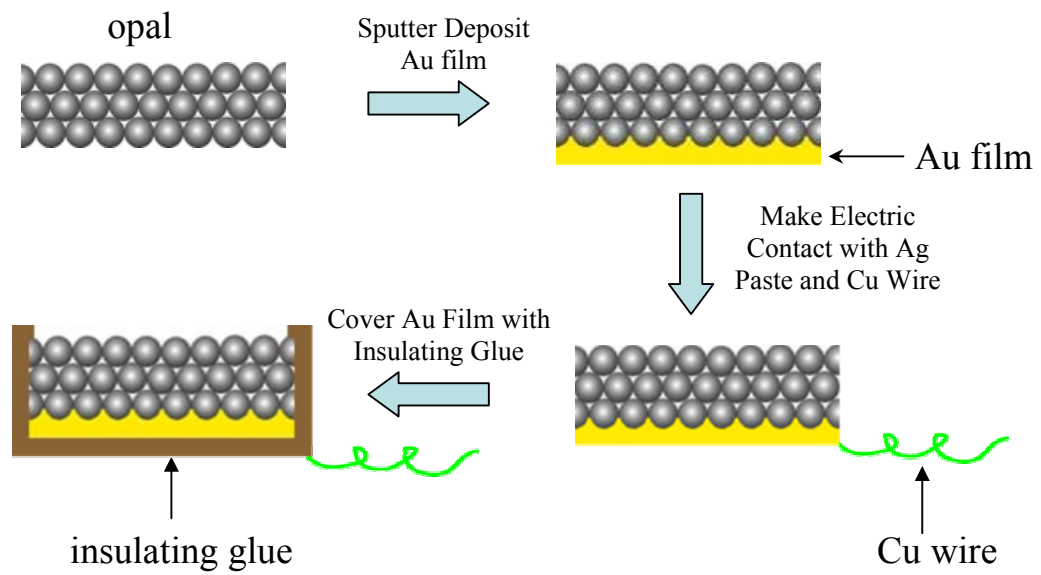
Figure 2.1. Schematic of opal membrane electrode fabrication.

Co plating solution: 200 g/liter $CoSO_4 \cdot 7H_2O$, 6 g/liter NaCl, 40 g/liter H_3BO_3,

pH ~ 3.5

Fe plating solution: 120 g/liter $FeSO_4 \cdot 7H_2O$, 40 g/liter H_3BO_3, 1g/liter L-ascorbic

acid, pH ~ 3.5

Cu plating solution: 50 g/liter $CuSO_4 \cdot 5H_2O$, and 6.2 g/liter H_3BO_3, pH ~ 4.5

2.2.4.2 Infiltration of Metals into Opals

Figure 2.2 shows the set-up for electrodeposition of metal in opal membrane. The opal membrane working electrode was immersed into metal plating solution with a platinum wire counter electrode. Electrodeposition was carried out using an EG&G Model 263A Potentiostat/Galvanostat by a constant current method. Usually, the current density was smaller than 0.50 mA/cm^2 and the deposition time was larger than 24 hours.

2.2.4.3 Removal of Opal Templates

After deposition, the opal templates were washed thoroughly with distilled water and the insulating glue layers peeled off. To remove the silica matrix, the metal-opal pieces were soaked in a 2% HF solution for 12 hours. This resulted in a black (for Ni, Pd, Co, Fe), brown (for Au, Cu), and white (for Ag) opalescent metal mesh membranes. Then the metal meshes were washed in turn with distilled water and acetone and dried for later characterization.

2.2.5 Characterization

2.2.5.1 Scanning Electron Microscopy Characterization

Scanning electron microscopy (SEM) and energy dispersive X-ray spectroscopy (EDX) analysis were performed on a JEOL JSM 5410 SEM. The samples were affixed to conductive carbon tape and loaded on specimen mounts for
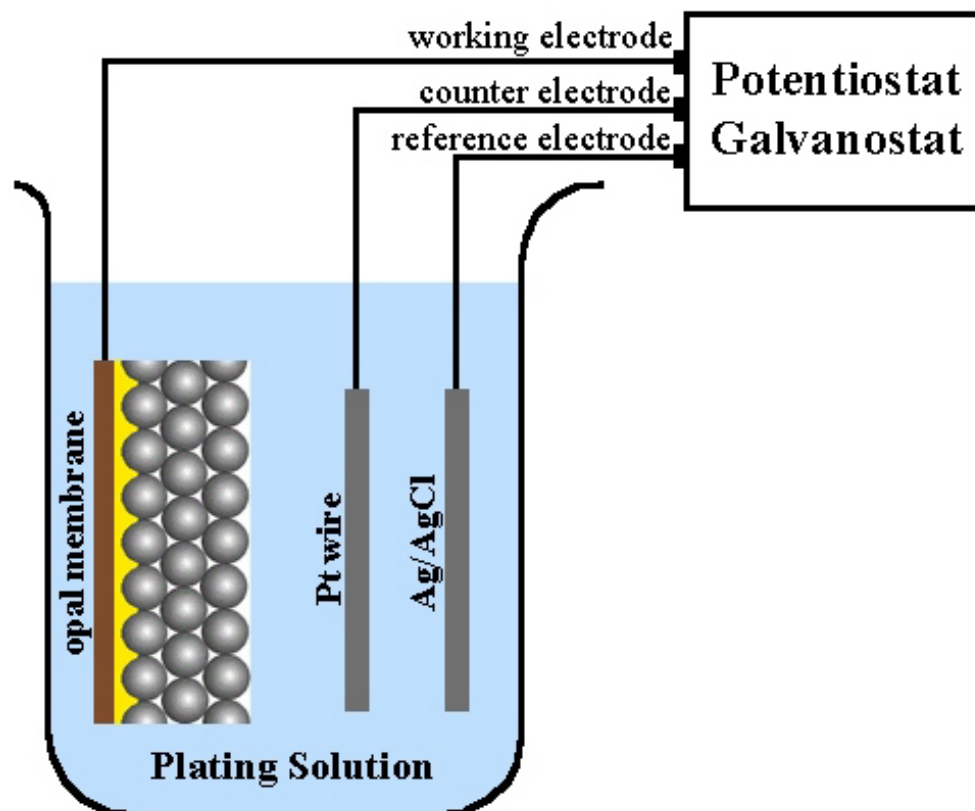
Figure 2.2. Set-up for electrodeposition of metal in opal membrane.

SEM. For non-conducting samples like opal, a thin-layer (~ 4 nm) of Au was sputtered onto the surface of samples before the SEM observation.

2.2.5.2 Transmission Electron Microscopy Characterization

Transmission electron micrographs (TEM) and electron diffraction patterns were obtained by using a JEOL 2010 TEM operating at 200 kV. The samples were prepared by mounting small pieces of mesh on TEM copper grid and directly loaded in TEM for observation.

2.2.5.3 Optical Images

Optical picture were taken by a Sony DSC-S75 digital camera with 3.3-megapixel CCD, 3× optical zoom lens and 2× digital zoom under a white light illumination.

2.2.5.4 Magnetic Properties

Magnetic measurements on the nickel meshes and bulk Ni film were performed on an MPMS-5S superconducting quantum interference device (SQUID) magnetometer. The sample was fixed between two pieces of KAPTON tape and placed in a commercially available soda straw. The temperature dependence of magnetization (zero-field-cooled and field-cooled curves) was obtained according to the following procedure. The sample was cooled at first to 2 K without any external magnetic field. Then a magnetic of 1000 Oe was applied and the magnetization was recorded as the temperature slowly rose to 350 K. The procedure was then repeated, but this time the sample was cooled in a field (1000 Oe) to 2 K. The temperature was again increased from 2 K to 350 K. No correction for the diamagnetic contribution of the sample holder was taken into account because it was by at least three orders of magnitude smaller than the response generated from the Ni meshes.

The field dependence of magnetization (hysteresis loop) was studied at various temperatures (2 K, 10 K, 300 K and 350 K) in external fields up to $\pm$ 50,000 Oe. To produce a hysteresis loop, a sample was cooled to a specific temperature. Once the desired temperature was achieved, measurements of the sample's moments as a function of field began. The field was slowly swept from -50,000 Oe to 50,000 Oe and then back to -50,000 Oe.

2.3 Results and Discussion

2.3.1 Chronopotentiogram for Electrodeposition

Figure 2.3 is a typical chronopotentiogram for the electrodeposition of Ni into opal membrane with 290 nm diameter silica spheres at applied constant current density of 0.50 mA/cm^2. The potential-time curve shows a slight overpotential at the first stage of electrodeposition, then eventually the potential reaches a steady state. The stable plating potential indicates homogeneous growth of Ni within the opal membrane, thus the volume of Ni deposited can be controlled by varying the plating time. Based on Faraday's Law, the thickness (t_{Ni}) of deposited Ni mesh can be estimated from equation 2.1:

$$t_{Ni} = \frac{[\text{No. of Coulombs of Ni(II)] (atomic weight of Ni)}}{2 \times 96{,}485 A \rho_{Ni} P} \qquad (2.1)$$

where A is the area of opal membrane, ρ_{Ni} is the density of Ni metal, and P is the porosity of opal membrane. The sphere filling fraction of opal with cubic close-packed structure is 0.74,[45] then the porosity of opal is 0.26. The estimated growth rate of Ni mesh at plating current density of 0.50 mA/cm^2 is only 2.4 μm/hour, as is similar to what is observed. The control of current density is very important in the electrodeposition of metal meshes. Usually, a low plating current density ($\leq$ 0.50
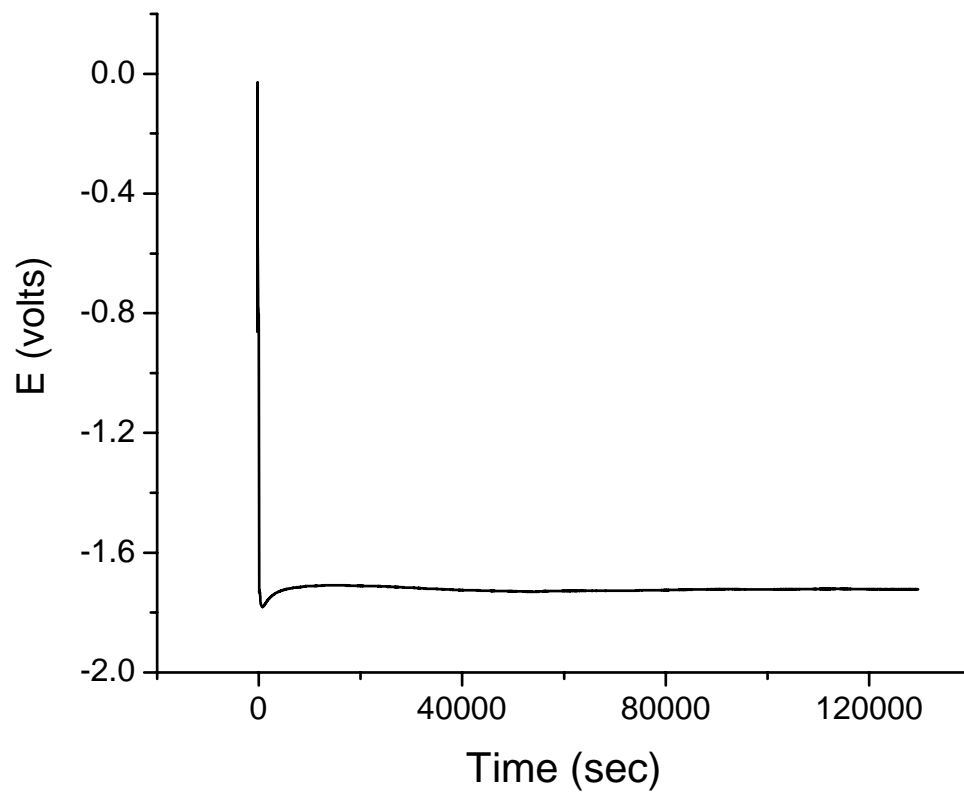
Figure 2.3. Chronopotentiogram for the electrodeposition of Ni into opal membrane.

mA/cm^2) is used for the uniform growth of Ni within the opal membrane due to the

much lower Ni^{2+} diffusion rate inside complex nanoporous channels of opal. A

current density of 1.0 mA/cm^2 was attempted, but this resulted in very uneven Ni

deposition. For some metals like Pd and Au, even smaller current density is needed

for uniform metal growth, possibly due to their much lower plating concentrations.

2.3.2 Microstructure of Metal Meshes

2.3.2.1 Scanning Electron Microscopy Characterization

  This electrodeposition method produces well-defined metal meshes. The

electrodeposition starts from the bottom Au microelectrode, fills the void space

between the close-packed silica spheres of opal and grows toward the opal membrane

surface. Figure 2.4 shows a cross-sectional SEM picture of opal membrane consisting

of three-dimensionally ordered silica spheres with 290 nm diameter ($\times$ 10,000

magnification). As can be seen from the picture, (111) and (100) orientations of silica

spheres and stacking faults are present in the original opal, which will be replicated in

the metal mesh. Figure 2.5a shows a cross-sectional view of Ni infiltrated opal near

the electrode side (Au film side). The electrodeposited Ni (white dots) fills the void

space of opal. Due to the sintering process in the formation of opal, small necks are

produced between the close-packed SiO$_2$ spheres.[25] The small necks make the

adjacent SiO$_2$ spheres connect to each other, and thus allow the silica spheres to be

chemically removed after electrodeposition. Figure 2.5b shows a section of a

palladium metal mesh (x 10,000) after dissolution of the silica spheres by dilute HF

solution. The lighter network in the image represents the metal mesh, and the dark

parts correspond to the air spheres (void space) that were previously occupied by

silica spheres. This image highlights the packing variation for the original silica

spheres. Different regions corresponding to (100) and (111) orientations can be
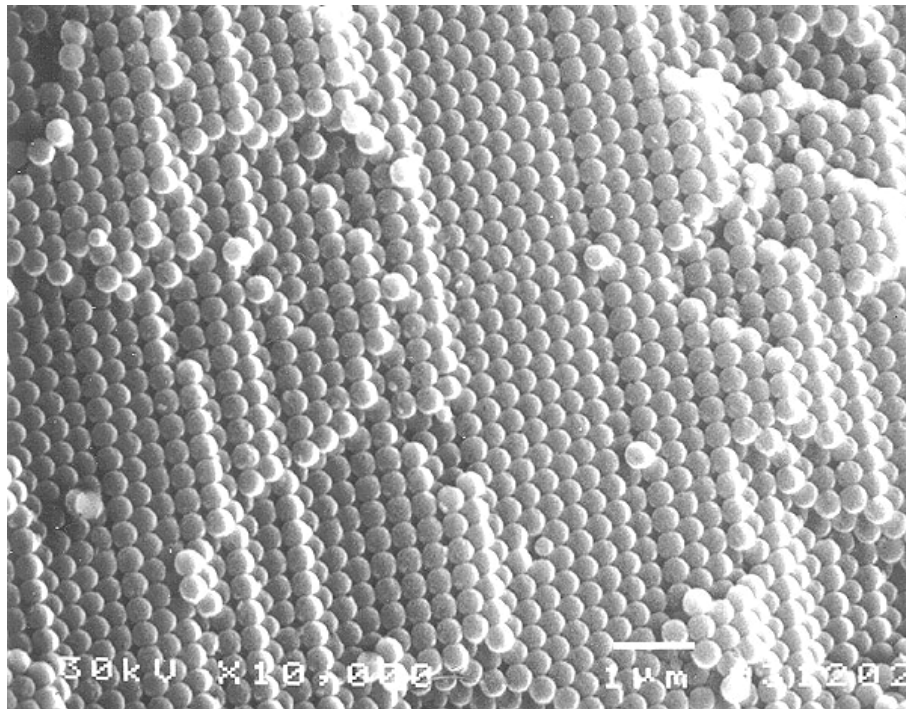
Figure 2.4. SEM picture of opal consisting of ordered silica spheres with 290 nm diameter (× 10,000).

a)

b)
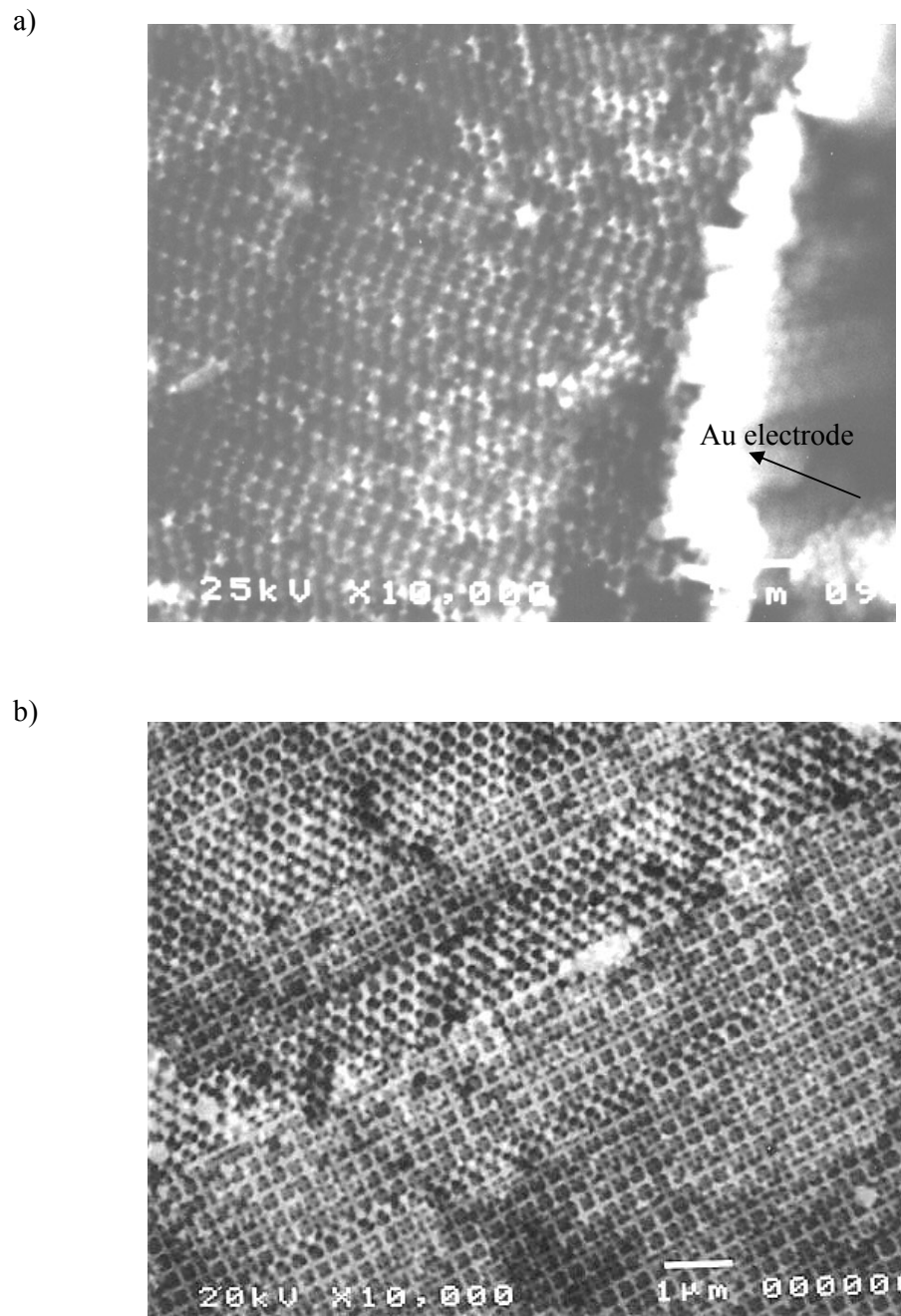
Figure 2.5. SEM pictures of a) cross-sectional view of Ni infiltrated 290 nm opal near the electrode side (× 10,000), b) top view of a piece of three-dimensionally periodic Pd mesh with 290 nm pores (× 10,000).

observed. At the boundaries between the (100) and (111) direction regions, the

regions can be seen clearly to be very well connected together. There are no transition

regions between them. Furthermore, it is observed that a triangular and a cross pattern

below each pore of the first layer of (111) and (100) direction region, respectively,

indicating that the metal mesh forms a three-dimensionally periodic structures. Since

the sphere filling fraction of opal with cubic close-packed structure is 0.74, the filling

factor of metal in the mesh structure is 0.26. Thus the metal meshes are materials with

high porosity.

Figures 2.6, 2.7 and 2.8 are SEM top views of predominately the (100), (110),

and (111) planes, respectively. Different magnification of metal meshes is presented

on these images. Based on these images, the diameter of air spheres (void space in the

meshes) is estimated to be 290 ± 10 nm, agreeing well with the diameter of original

silica spheres in opal, which indicates that the metal mesh does not contract after the

removal of opal. As can be seen very clearly from Figure 2.6a, a regular cross pattern

lies below the pores in the first layer, indicating the three-dimensional periodicity of

metal meshes. Figure 2.6b is a higher magnification ($\times$ 50,000) of the (100) plane.

The square features are essentially cubes with concave sides that arise from filling the

octahedral sites in the close-packed structure. Each cube is connected to eight other

cubes through its vertices via tetrahedra (Figure 2.9). The structure is akin to the

fluorite structure (CaF_2) where the calciums, representing the cubes, are eight

coordinate and the fluorides, representing the tetrahedra, are four coordinate. Relative

to the structure of close-packed spheres with diameter D, the diameters of octahedral,

tetrahedra and interconnect minimum are 0.414D, 0.225D, and 0.155D,

respectively.[43,44] Then for 290 nm diameter opal, one would calculate minimum

a)
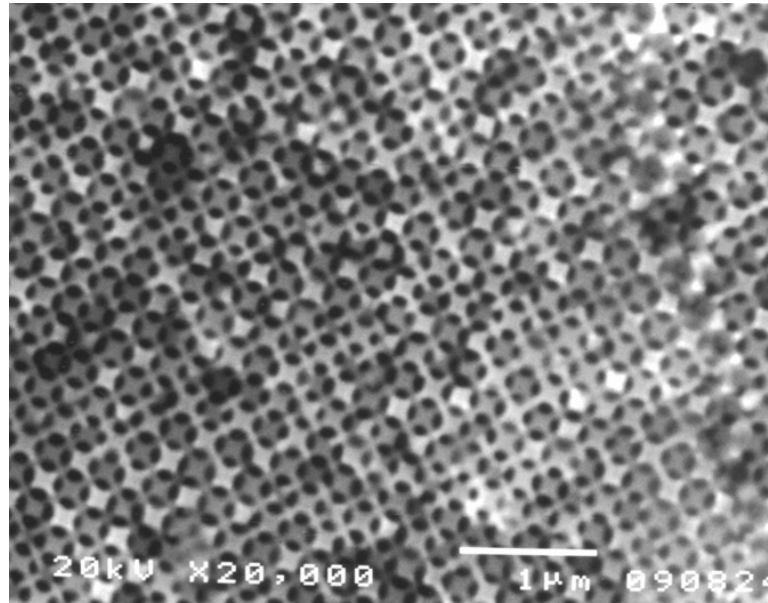
b)
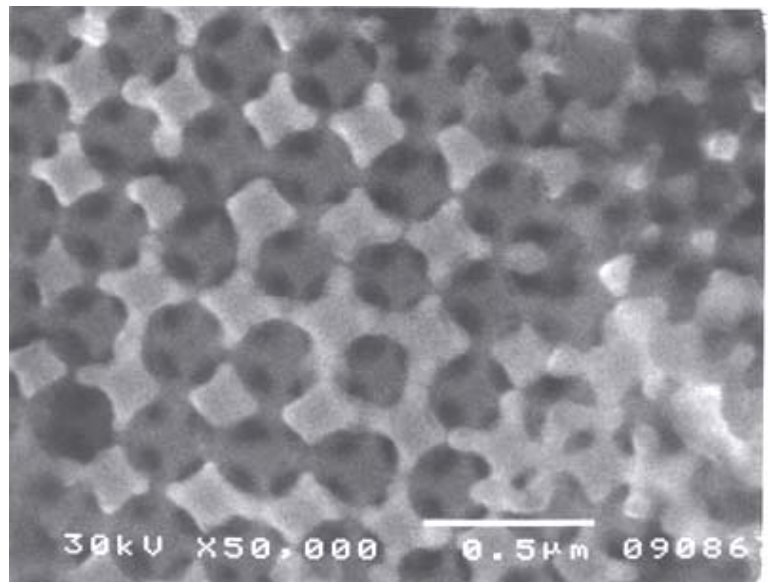
Figure 2.6. Top view SEM pictures of 290 nm Ni meshes with predominately (100) orientation at magnification of a) × 20,000, b) × 50,000.

a)
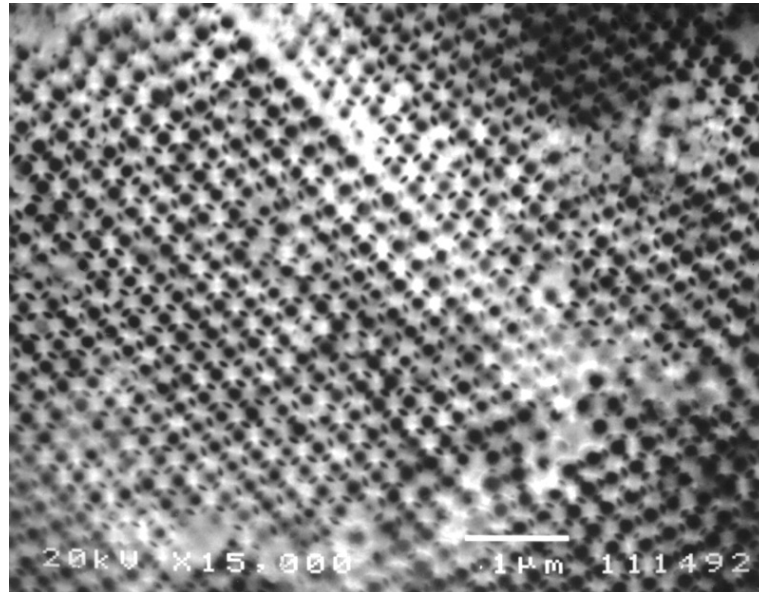
b)
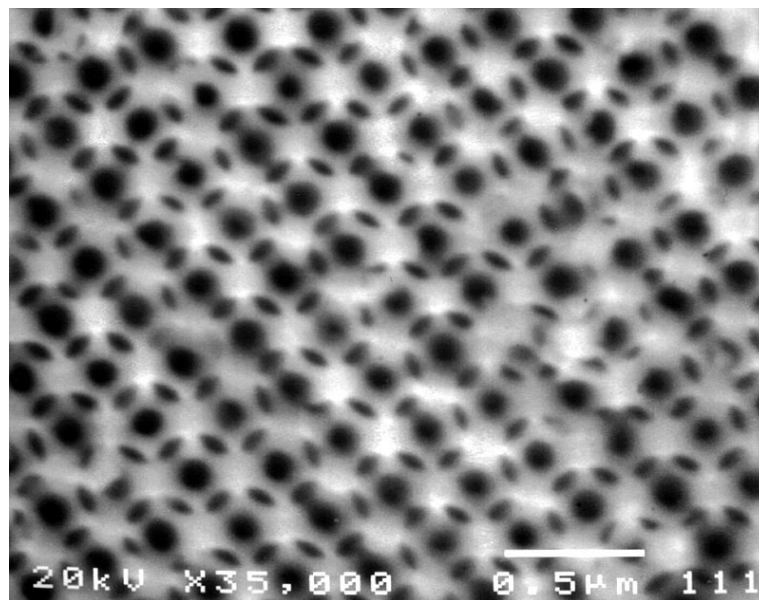
Figure 2.7. Top view SEM pictures of 290 nm Ni meshes with predominately (110) orientation at magnification of a) × 15,000, b) × 35,000.

a)

b)
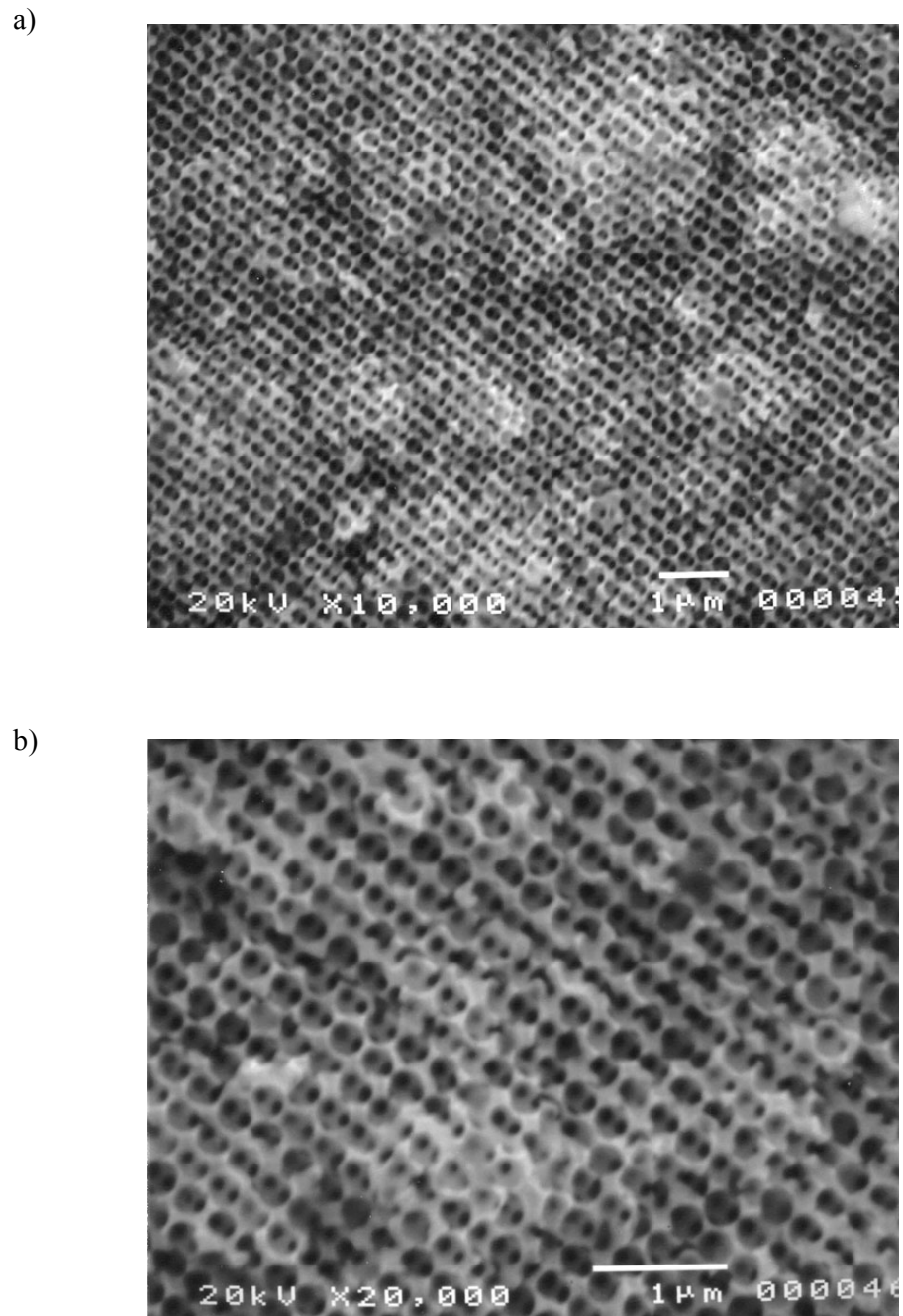
Figure 2.8. Top view SEM pictures of 290 nm Au meshes with predominately (111) orientation at magnification of a) × 10,000, b) × 20,000.

a)

b)
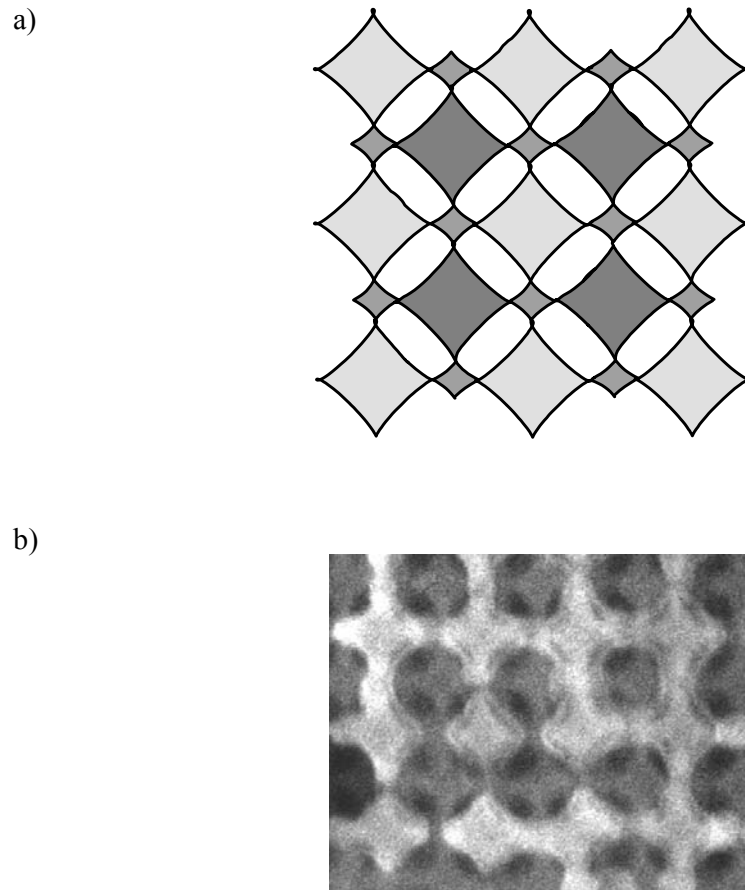
Figure 2.9. a) Illustration of square motif seen in Figure 2.6 (the lighter regions are the
closer and the darker regions are progressively further away), b)
corresponding (100) SEM picture of Ni mesh.

diameters of approximately 120 nm, 65 nm, and 45 nm for the cubes, tetrahedra and interconnects, respectively, and this is observed.

The periodic metal meshes with 220 nm and 180 nm pores can also be fabricated by the use of 220 nm and 180 nm opals as templates, respectively. Figure 2.10a shows the SEM picture of 220 nm Pd mesh ($\times$ 20,000) and Figure 2.10b is the image of 180 nm Ni mesh ($\times$ 10,000).

Sometimes, the surface layers of mesh lack long-range periodicity. Some areas of the mesh appear nodular. This effect is not due to disorder in the opal, but rather because of uneven deposition. Such a phenomenon was also observed by Braun *et al.* in the electrodeposition of macroporous CdS (CdS mesh).[54] This effect can be more apparent by the view of metal mesh in a larger area. Figure 2.11a shows the low magnification ($\times$ 2,000) top view of Pd mesh with 290 nm pores fabricated by 3-day electrodeposition at a current density of 0.25 mA/cm^2. Due to the uneven growth, the Pd mesh shows a cauliflower-like surface. The mountain-like cross-sectional SEM image verifies the uneven deposition in Pd mesh (Figure 2.11b). When opal with smaller voids is used as template, the electrodeposition becomes more uneven. Figure 2.12a and 2.12b show the top view SEM pictures of Pd mesh with 220nm pores and 180 nm pores, respectively. Both meshes were fabricated at a current density of 0.25 mA/cm^2 over a 3-day period, same condition as Pd mesh with 290 nm pores. It is seen that the growth of 220 nm mesh is more uniform than that of 180 nm mesh, but more uneven than that of 290 nm mesh.

The current density also plays a very important role in the growth of metal meshes. When the current density decreases, the growth of metal meshes becomes more uniform. Figure 2.13a and 2.13b show the surface of Au meshes obtained at current density of 1.0 mA/cm^2 and 0.20 mA/cm^2, respectively. Apparently, the

a)
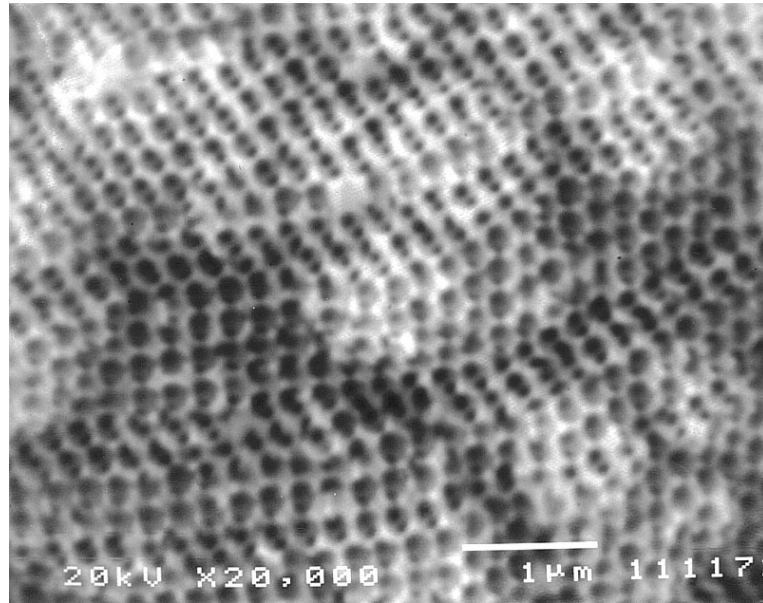
b)
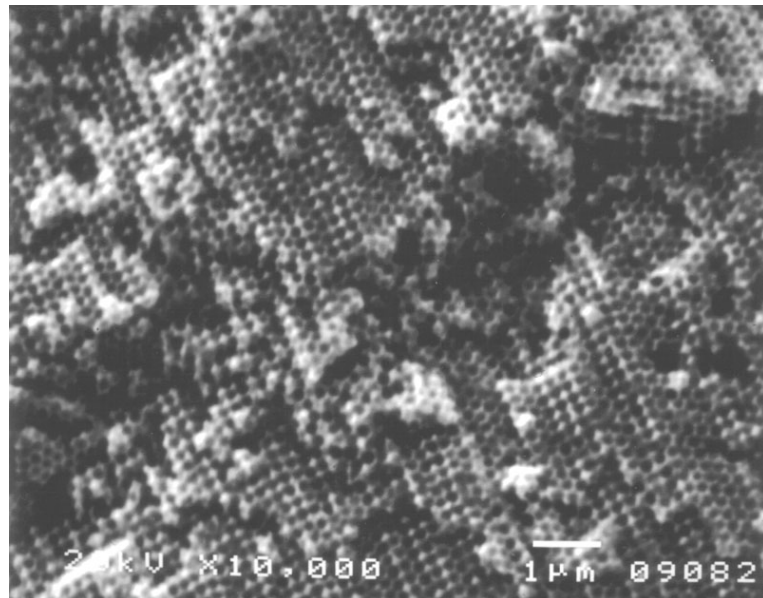
Figure 2.10. Top view SEM pictures of a) 220 nm Pd meshes (× 20,000),
b) 180 nm Ni mesh (× 10,000).

a)
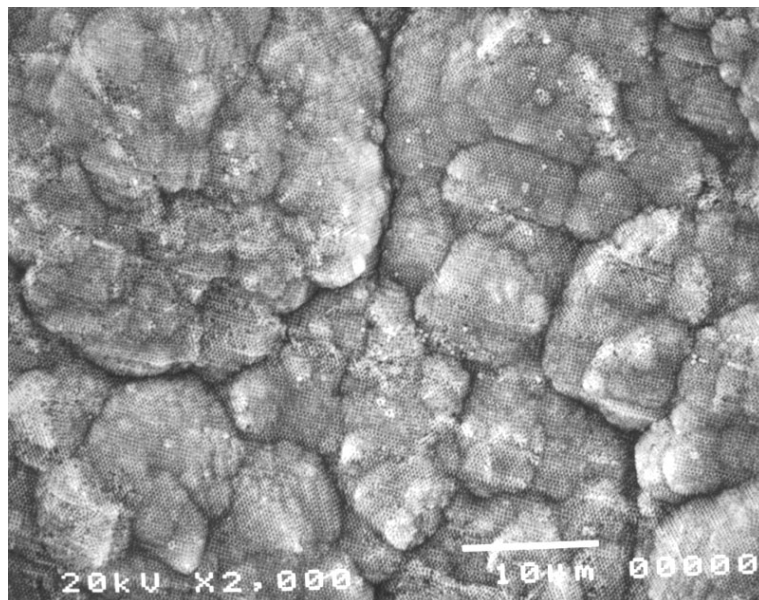
b)
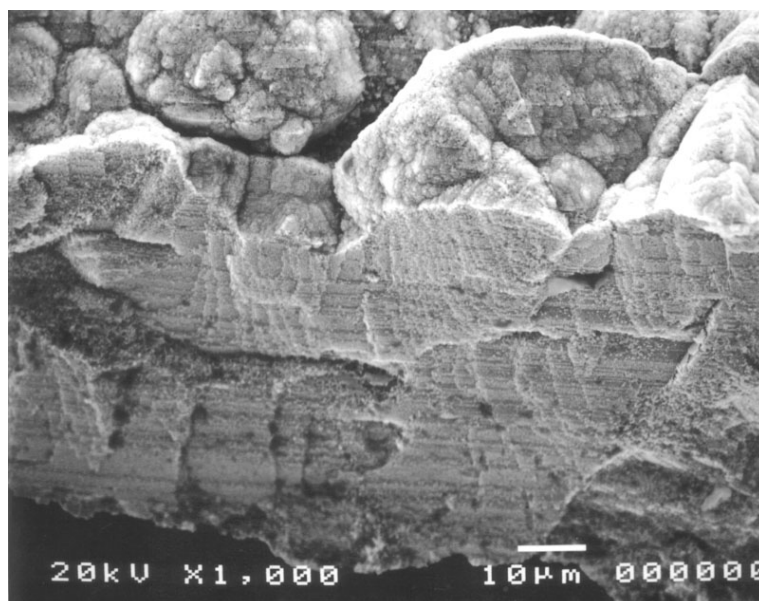
Figure 2.11. SEM pictures of 290 nm Pd mesh. a) top view showing cauliflower-like surface ($\times$ 2,000), b) cross-sectional view, $\times$ 1,000.

a)
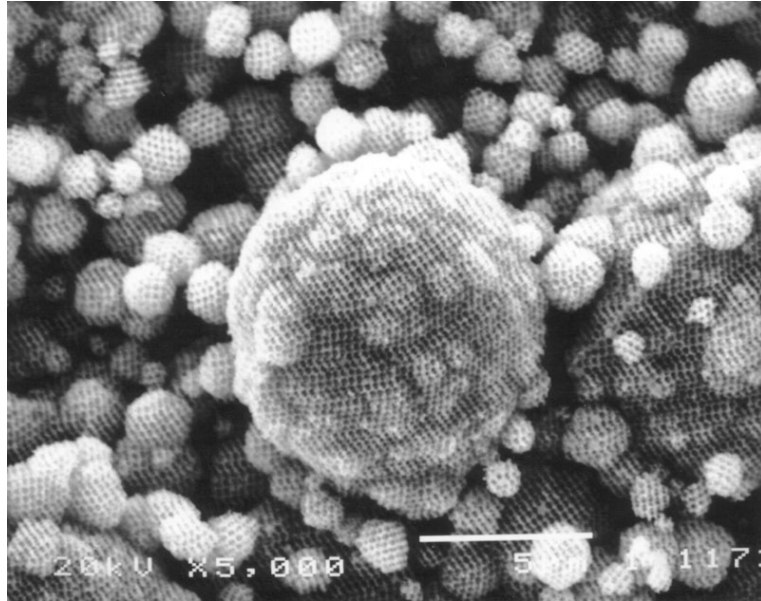
b)
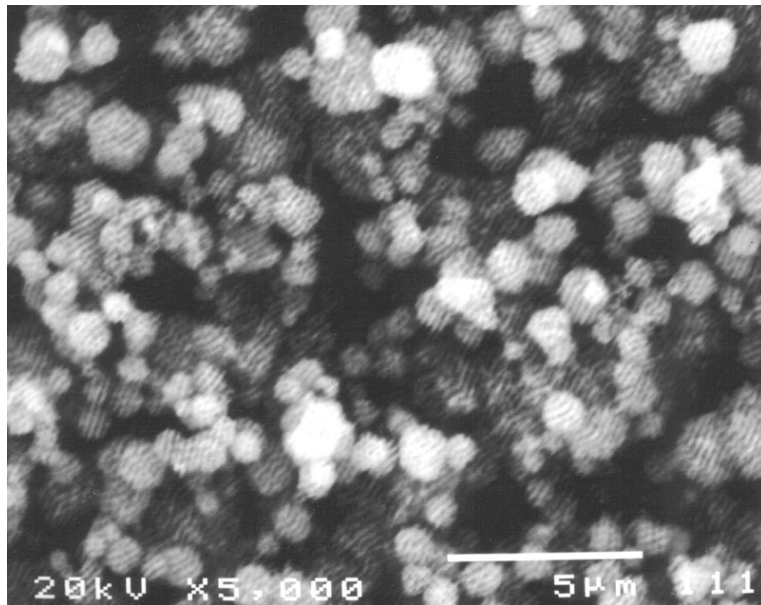
Figure 2.12. Top view SEM images of a) 220 nm Pd mesh ($\times$ 5,000),
b) 180 nm Pd mesh ($\times$ 5,000).

a)
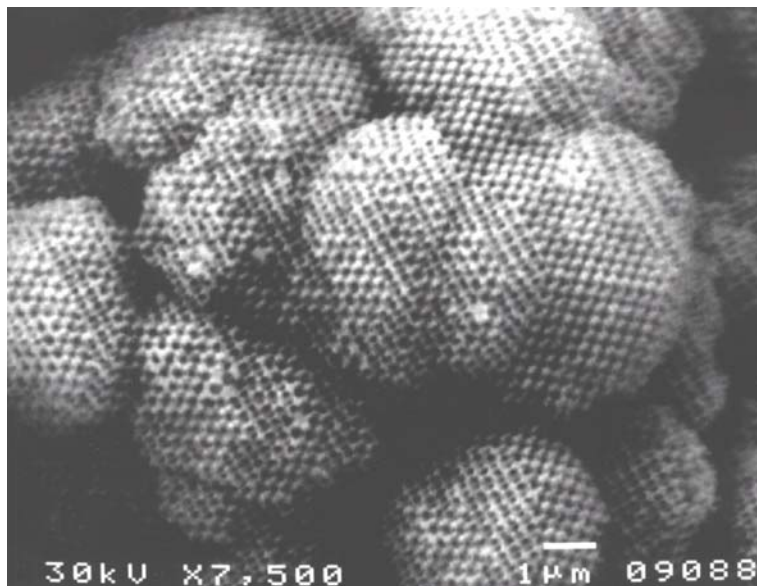
b)
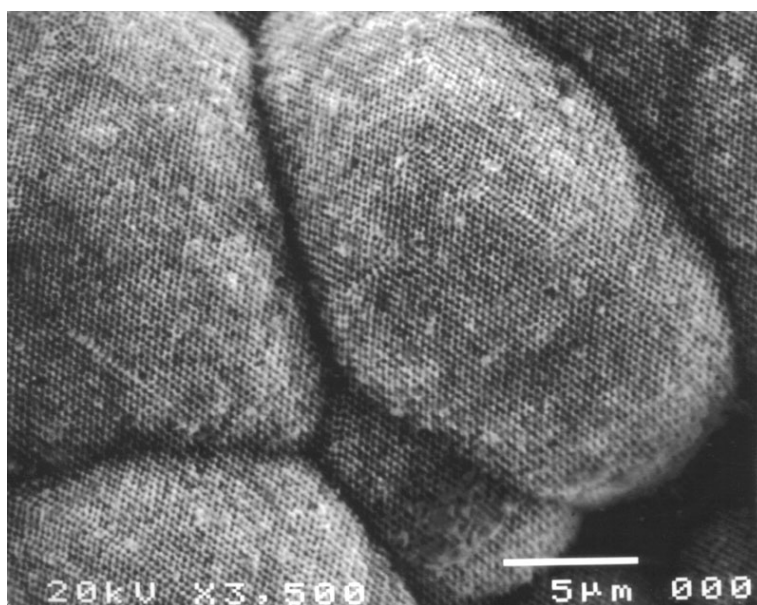
Figure 2.13. Top view SEM images 290 nm Au meshes. a) obtained at current density of 1.0 mA/cm^2 ($\times$ 7,500), b) obtained at current density of 0.20 mA/cm^2 ($\times$ 3,500).

diameter of the spherical "floret" is larger for Au mesh with 0.20 mA/cm^2 constant

current deposition, indicating the more uniform growth.

Though sometimes the electrodeposition for metal meshes (especially for Au

and Pd meshes) was uneven, the filling of the underlays is quite complete, as can be

seen from cross-sectional SEM images of Pd meshes (Figure 2.14 and Figure 2.15).

Cross-sections for SEM studies were prepared simply by physically separating

segments with a small blade, the step faults, holes and clumps in the images therefore

likely result from this process. The cross sections show long range periodicity, which

is quite different from the surface of Pd mesh, indicating the cauliflower-like surface

of metal meshes come from uneven electrochemical growth.

Highly pure metal meshes are obtained by the electrodeposition process, as

can be confirmed by the EDX (energy dispersive X-ray) spectra as shown in Figure

2.16. No silicon is detected, indicating the complete etching away of the opal

templates by dilute HF solution. Due to the surface oxidation in the air, a tiny amount

(< 3%) of oxygen is found on the EDX of Ni, Co and Cu meshes.

2.3.3.2 Transmission Electron Microscopy Characterization

TEM was also used to examine the Ni mesh. Figure 2.17a shows a TEM

image of opal (silica sphere arrays) filled with Ni. The lighter regions in the image

represent the opal framework, and the darker parts are the infiltrated Ni nanoparticles.

A (100) monolayer and multiple silica layers, as well as (111) stacking faults can be

seen. By loading a small piece of the inverse Ni mesh on a TEM copper grid, the two

dimensional projection of Ni network in predominately (110) orientation can be seen

as shown in figure 2.17b. The lighter regions now represent the void space previously

occupied by silica spheres. Figure 2.18a reveals a higher magnification of Ni mesh

with (100) orientation. Microtwins and stacking faults were found as shown in Figure

a)
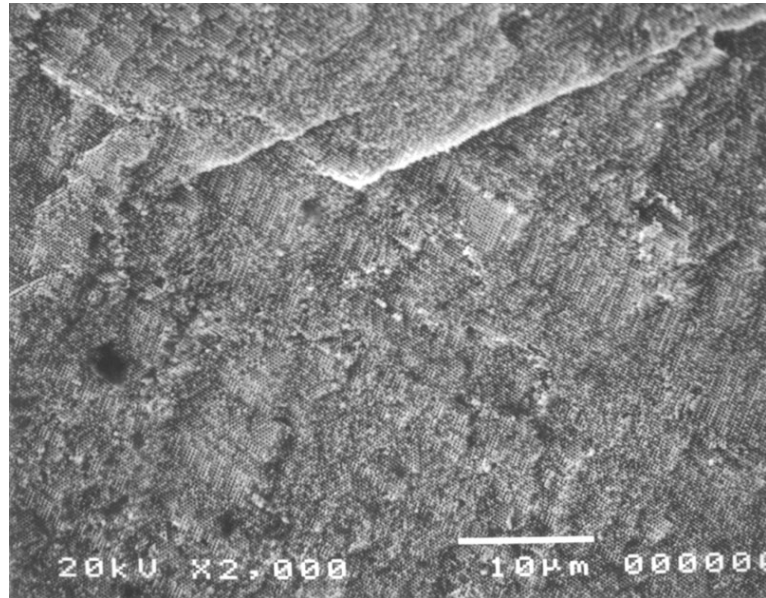
b)
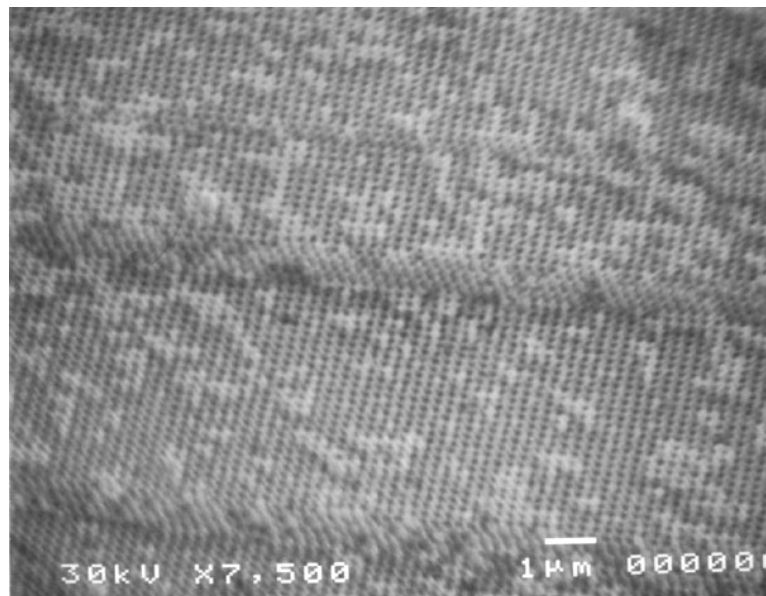
Figure 2.14. Cross-sectional view SEM images of 290 nm Pd mesh. a) × 2,000,
b) × 7,500.

a)

b)
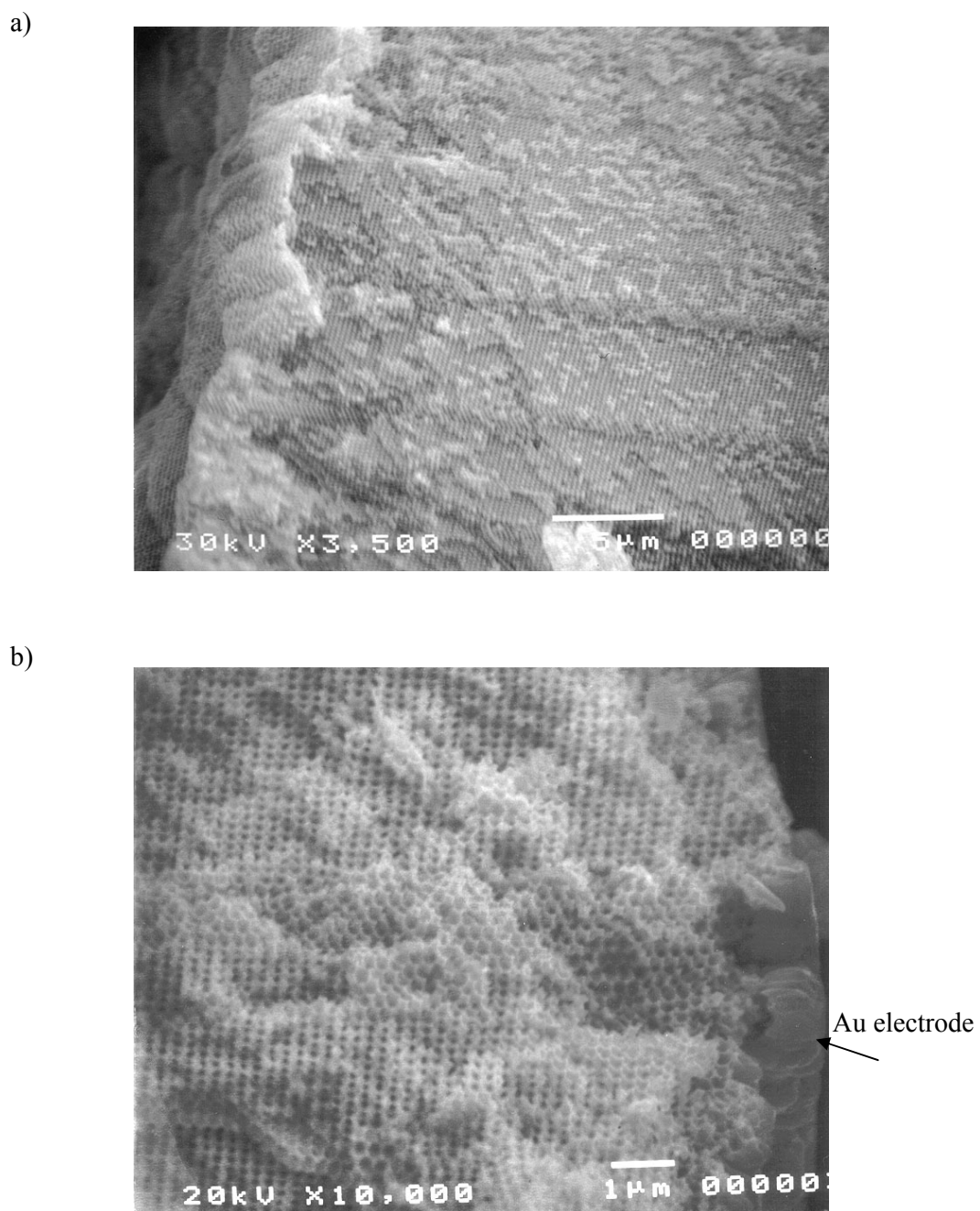
Au electrode

Figure 2.15. Cross-sectional view SEM images of 290 nm Pd mesh.
a) near surface, × 3,500, b) near Au electrode, × 10,000.

Figure 2.16. EDX spectra of a) nickel mesh, b) cobalt mesh, c) palladium mesh, d) gold mesh, e) silver mesh, f) copper mesh. The small amount of C on the EDX of metal meshes result from the C substrate.

a)
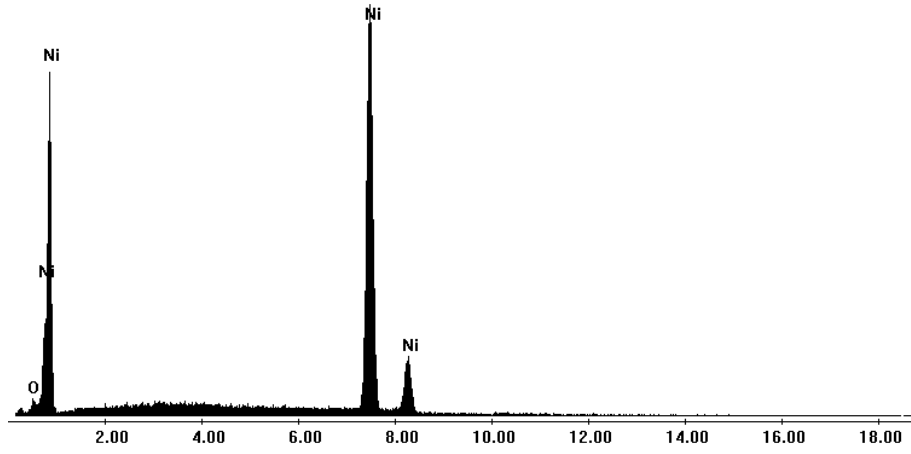
b)
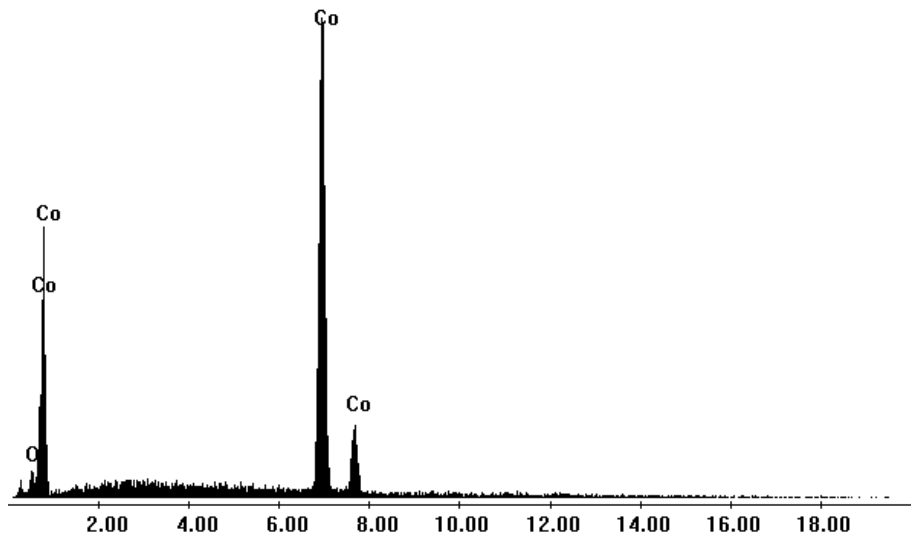
c)
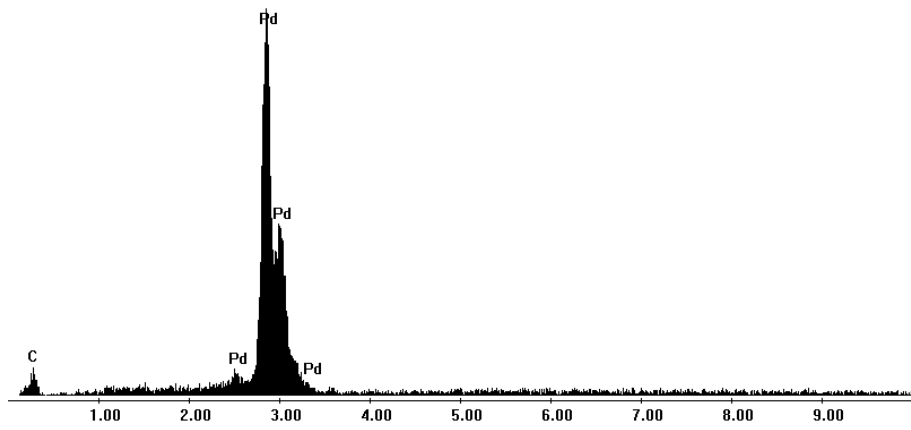
d)
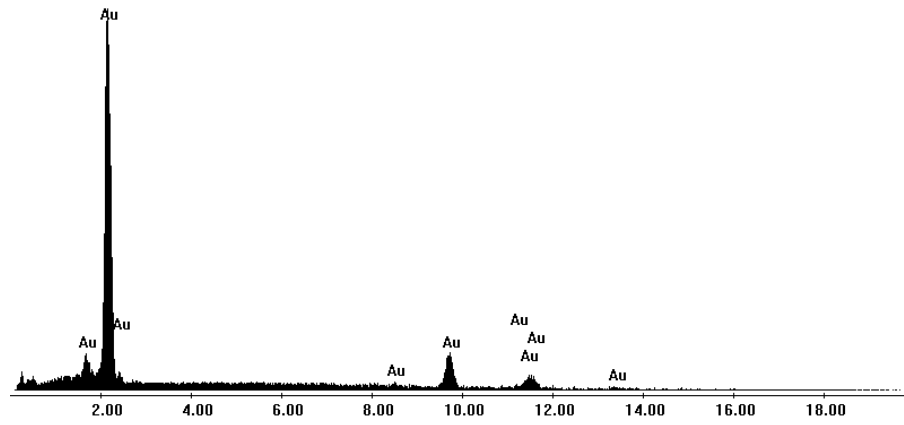
e)
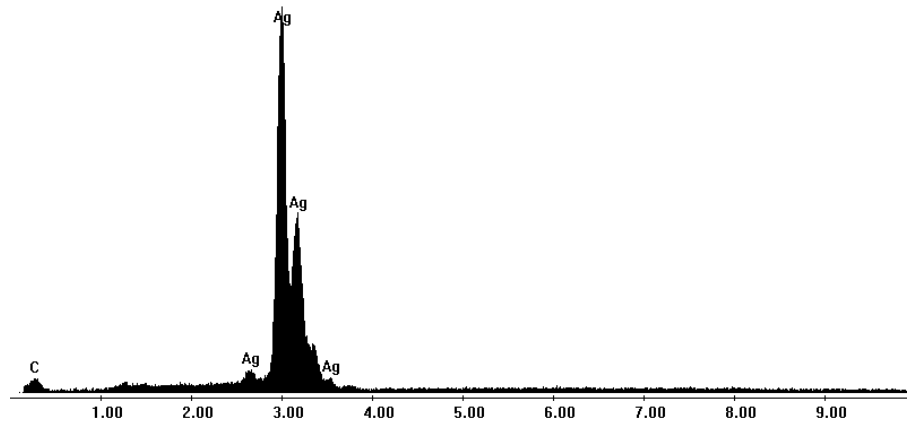
f)
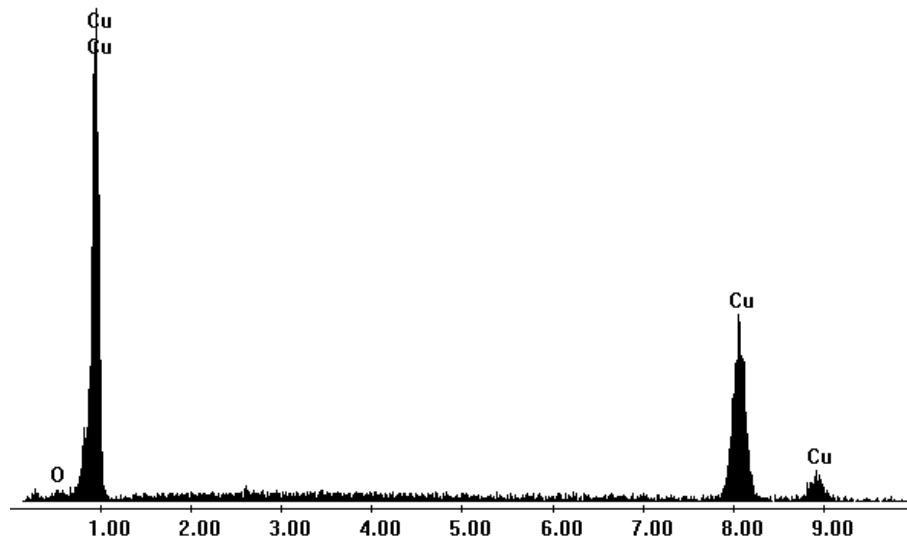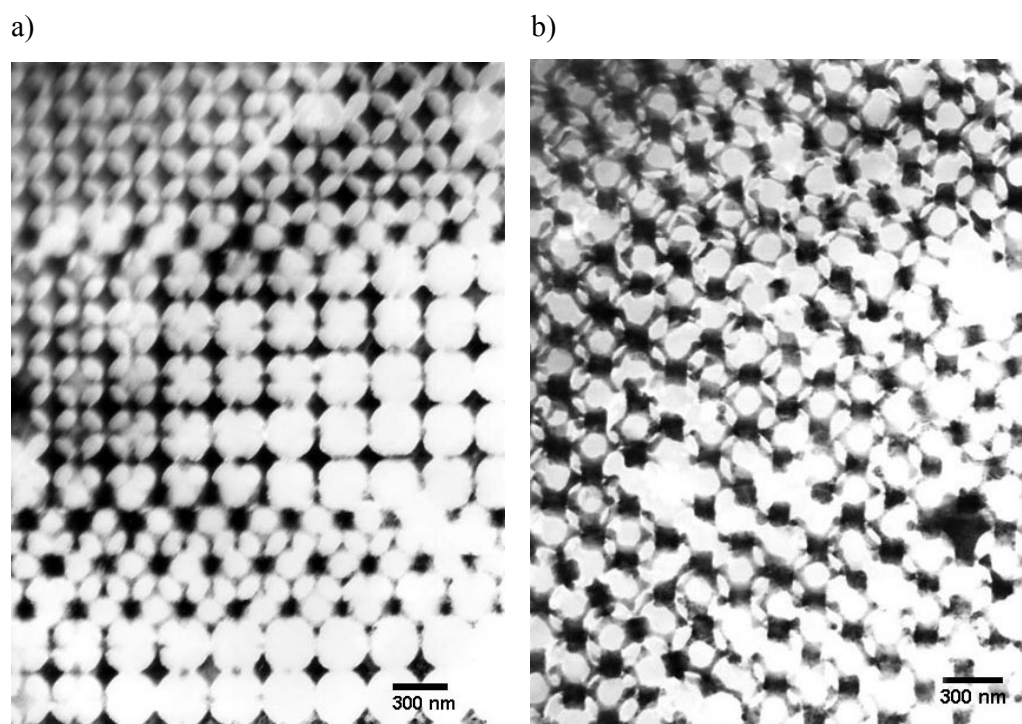
Figure 2.17. TEM images of (a) silica colloids with Ni infiltration, (b) macroporous Ni mesh in predominately (110) orientation.

a)
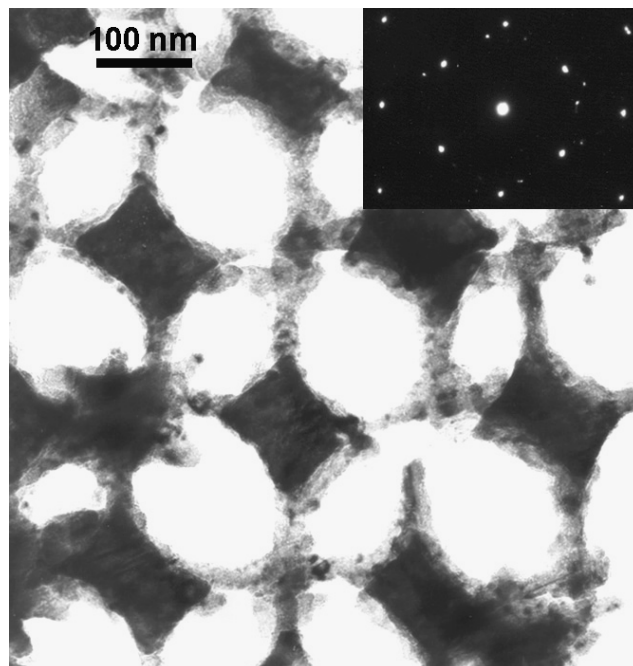
b)
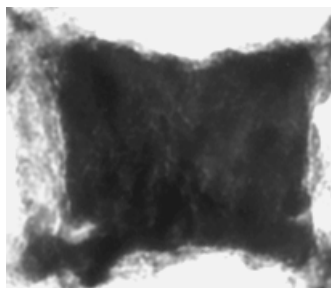
c)
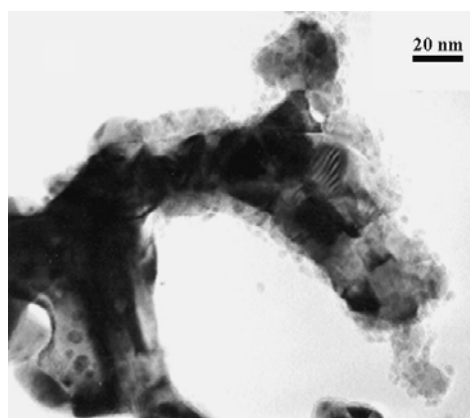
Figure 2.18. TEM images of a) Ni mesh in (100) orientation (inset is the <110> SADP of single Ni cube), b) a single Ni cube magnified from that in a), c) a single macropore with Ni/NiO pore wall.

2.18b by carefully investigating a single cube, which can be also determined from the

<110> SAED (selected area electron diffraction) pattern as shown in the inset of

Figure 2.18a. The streaks and twin diffraction spots can be clearly seen. By doing

SAED of many nickel octahedra, it was found that the most octahedral cubes formed

single crystals during the electrodeposition. The reason for forming such unique

structure is that the octahedral interstices have bigger space and gave enough time for

Ni cubes to crystallize and grow into homogeneous structure. The connections of the

macromesh consisted of nanograins. The narrow space of connections and large silica

surface provide a rapid quenching environment for forming Ni nanograins. Even

though the single crystal octahedral Ni cubes were formed, it was hard to find any

preferential growth of these nanocubes by doing SAED. The SAED showed

polycrystalline face-centered cubic (fcc) Ni feature with homogenous diffraction rings

(Figure 2.19a). The nanograins of the connections were composed of Ni

nanocrystallites with size range from 20-50 nm. The SAED in Figure 12a also reveals

the existence of fcc NiO. On close examination of a single macropore wall, it was

often found some small nanocrystals with size about 5 nm sticking on the surface of

the Ni membrane after etching away silica spheres as shown in figure 2.18c. By doing

EDX analysis, it was found that these nanoparticles contained Ni and oxygen, which

was also confirmed as NiO nanocrystals by doing SAED. Similar phenomena was

also observed by Blanford et al..[76] When they removed the template in an oxygen

containing atmosphere, any metal formed was immediately oxidized producing metal

oxide. In our case, when the silica spheres were etched away, the fresh Ni surface was

exposed to air and easily oxidized and formed a layer of NiO nanocrystals. In addition,

the feature of Ni and NiO meshes is quite different from that prepared by chemical

synthesis method reported by Yan et al..[113] In their samples Ni or NiO walls of

a)
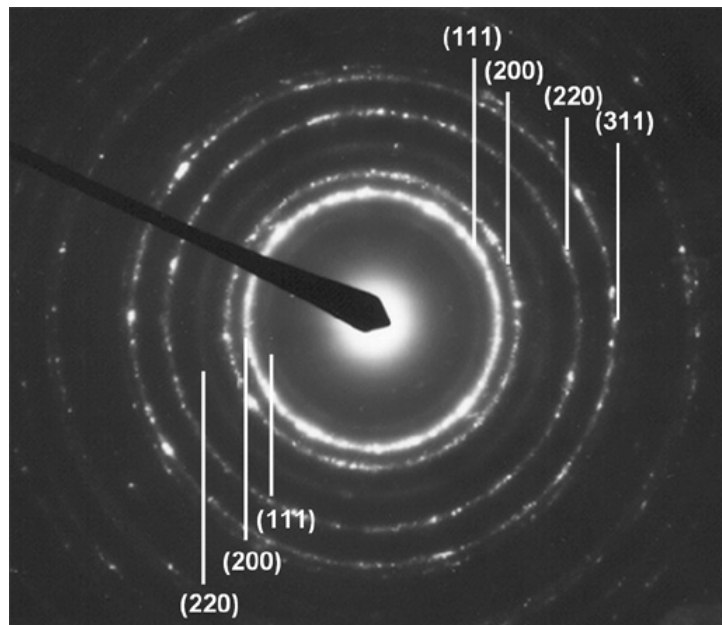
b)
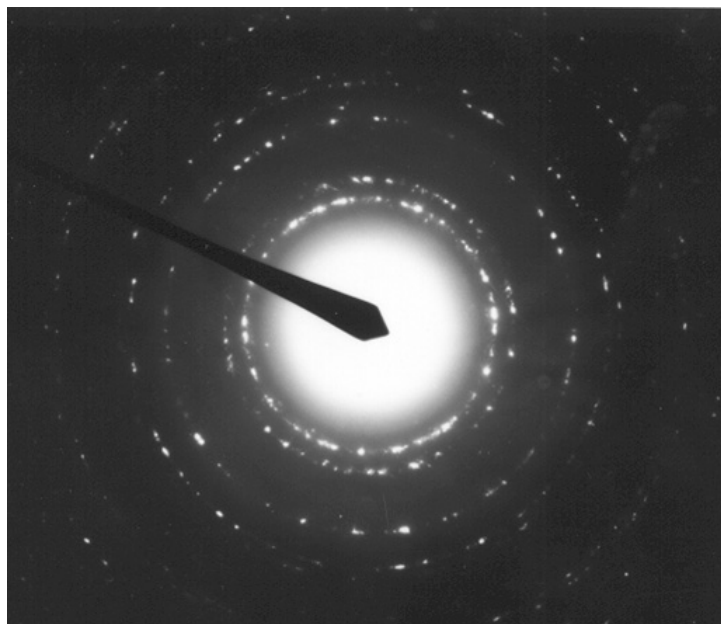
Figure 2.19. Selected area electron diffraction pattern for a) Ni mesh (the top right indices correspond to cubic Ni, while the left bottom indices correspond to cubic NiO), b) Ni/opal composite.

meshes were composed of fused nanograins with size about 50 nm and 6 nm, respectively. The NiO structure is hexagonal phase. In our case the nanocrystals of the NiO on the surface of the Ni membrane is face-centered cubic structure with size about 5 nm. On the contrary, no NiO diffraction ring was found from the SAED of Ni/opal composite (Figure 2.19b), indicating that the silica spheres can protect Ni nanoparticles from oxidation, similar to the situation in Ni infiltrated polyaniline nanotubules[167] and Co infiltrated ZrO_2 nanotubules.[168]

2.3.3 Optical Images of Opals and Metal Meshes

Since opals and metal meshes are structures with three-dimensional periodicity on a length scale comparable to that of light, they can strongly diffract white light, providing an iridescent coloration (Figure 2.20) that depends on the angle of the incidence on the crystals, the angle of observation, the spacing between the scattering planes, and the refractive index of materials, based on Bragg's Law (equation 2.2):[16]

$$m\lambda = 2n_a d_{hkl}\sin\theta \qquad (2.2)$$

where m is the order of the diffraction, λ is the wavelength of the diffracted light, n_a is the average refractive index of the 3D arrays, d_{hkl} is the interplanar spacing along the (hkl) direction, and θ is the angle between the incident light and the normal to the (hkl) plane. This equation indicates that the wavelength of the diffracted light is proportional to the interplanar spacing, then when the diameter of silica spheres in opals decreases, the wavelength of the diffracted light exhibits a blue shift if other conditions are the same. Due to the difference between the refractive indices of metal meshes and opal templates, they show different colors. The variation in color (Figure 2.20) arises from the fact that the films are not ordered in the whole surface areas, due to the defects like step faults in the crystals, as were observed in the SEM pictures.
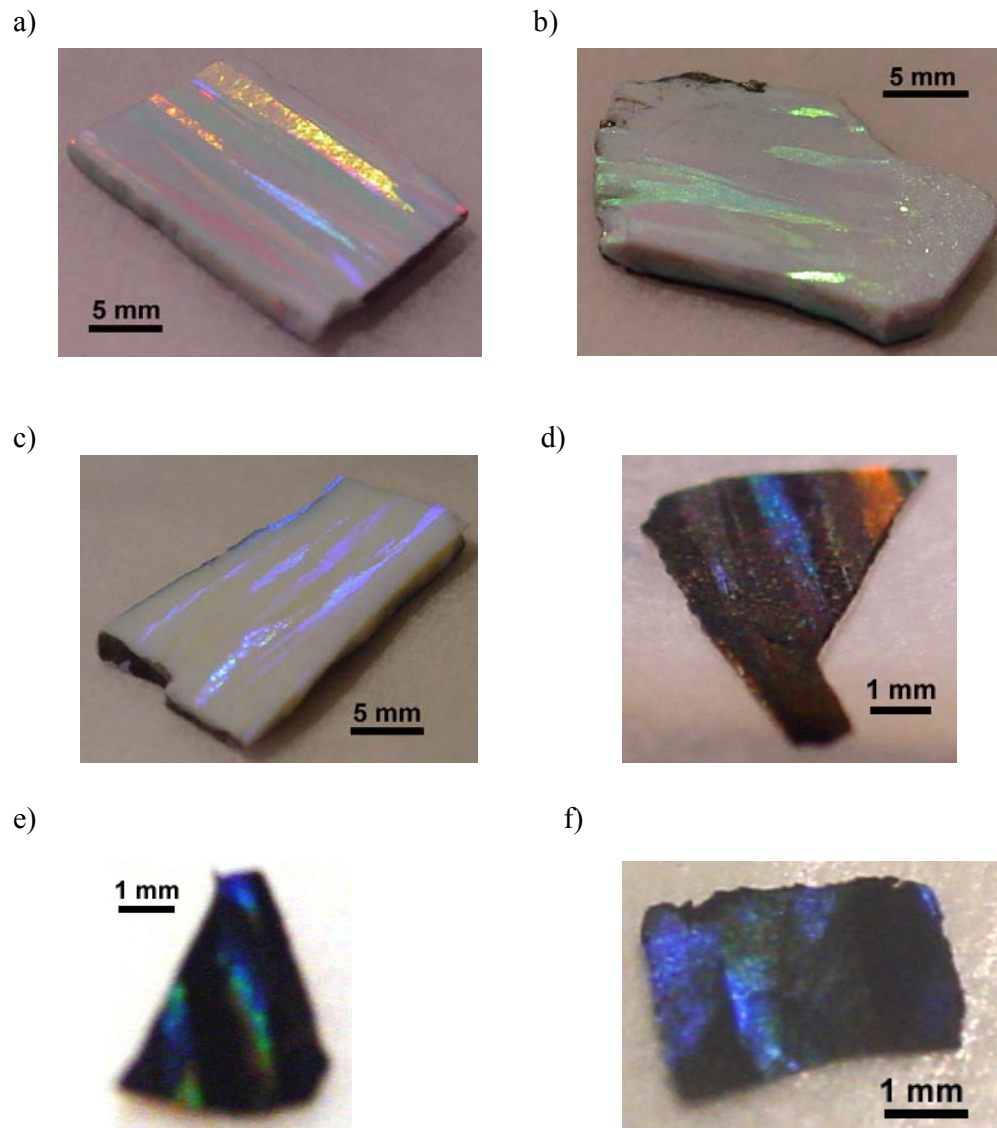
Figure 2.20. Opals and meshes (inverse opals) show opalescent colors.
a) 290 nm opal,   b) 220 nm opal,
c) 180 nm opal,   d) 290 nm Ni/opal composite,
e) 290 nm Ni mesh, f) 290 nm Pd mesh.

2.3.4 Magnetic Properties

Figure 2.21a shows the zero-field-cooled (ZFC) and field-cooled (FC) magnetization curves as a function of temperature taken in an applied field of 1000 Oe. The two curves separate at low temperature, and the ZFC curve exhibits a peak at 7 K and a broad peak with maximum at about 200 K, then the two curves merge at around 320 K. The maximum temperature (200 K) in the ZFC curve is called blocking temperature (T_B, at which the time to be thermally activated over the energy barrier becomes comparable to the measurement time). Because of their small size, anisotropy energy barrier for magnetic nanoparticles are smaller than for the bulk materials. Therefore, at high temperature, thermal energy can overcome the anisotropy barrier and allow a coherent rotation of the atomic moments of a nanoparticle. Then a nanomagnet may become superparamagnetic at a so-called blocking temperature, at which it would be magnetic in the bulk. When the temperature drops below the blocking temperature, the nanoparticle's moments are bound to the particle, and will not be very susceptible, so the induced magnetization will be small. This creates a peak at the blocking temperature for the ZFC magnetization under an applied field with increasing temperature.[169,170] When a size range of nanoparticles exists, there is a corresponding range in blocking temperature. Consequently, a size distribution broadens the ZFC maximum. The blocking temperature T_B at 200 K is related to the blocking of nanoparticles with average sizes, while the merging temperature (320 K) corresponds to the blocking of the largest particles. The broad maximum of ZFC curve indicates a distribution of particle sizes in Ni mesh, as is consistent with the SEM and TEM results. Interestingly, the ZFC curve also exhibits a sharp peak at 7 K, which may result from Ni nanoparticles with extremely small size[171] or from the surface NiO nanoparticles. Though bulk NiO

a)
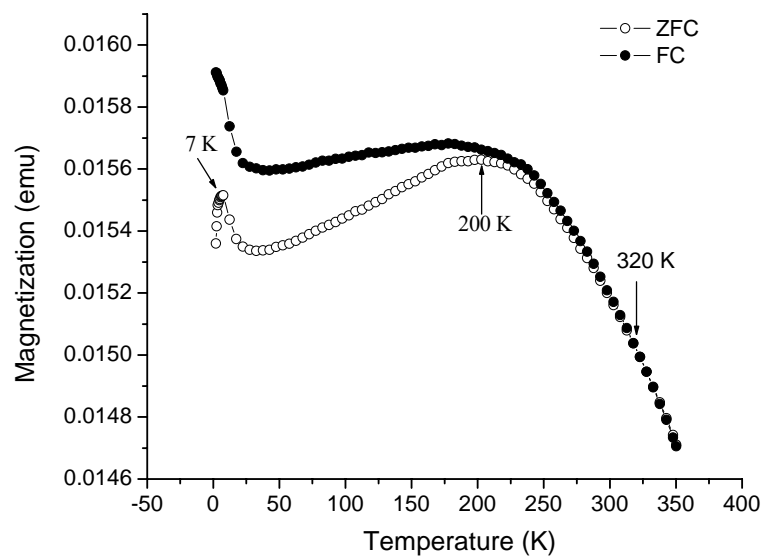
b)
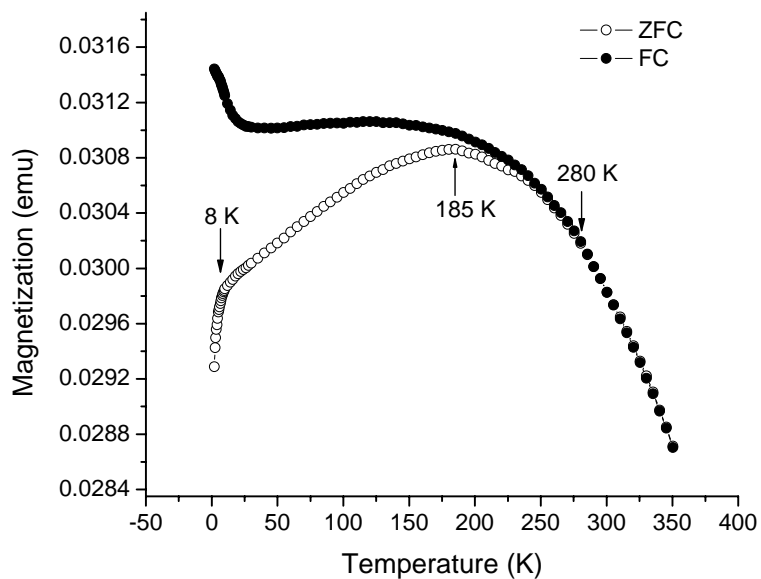
Figure 2.21. Temperature dependence of magnetization for a) 290 nm Ni mesh.
b) 180 nm Ni mesh. The zero-field cooled (ZFC), field-cooled (FC)
curves were recorded at 1000 Oe.

shows antiferromagnetism with Néel temperature (T_N) of 523 K, it is observed that NiO nanoparticles exhibit weak ferromagnetism and superparamagnetism due to uncompensated surface spins caused by the finite particle size.[172-176]

Figure 2.21b shows the ZFC-FC curves (applied field: 1000 Oe) of 180 nm Ni mesh. The shape of ZFC and FC curves is similar to that of 290 nm Ni mesh, but with average blocking temperature T_B of 185 K and merging temperature of 280 K, respectively, both smaller than the corresponding 290 nm Ni meshes, due to the reduced particle size in 180 nm Ni meshes.

In-plane hysteresis loops (magnetization versus applied field plots) at different temperature of 290 nm Ni mesh, 180 nm Ni mesh and bulk Ni film (fabricated by electrodeposition) were also obtained by SQUID magnetometer. Figure 2.22a shows the hysteresis loops of 180 nm Ni mesh measured at 5, 10, and 300 K and Figure 2.22b is the full range of the hysteresis loops (field range of between -50,000 to 50,000 Oe). The material exhibits a coercive field (H_c) of 506 Oe and squareness SQ (ratio of remanence to saturation magnetization, M_r/M_s) of 0.540 at 5 K. Both the coercivity and SQ decrease slowly with increasing temperature. The material reached a coercivity of 271 Oe and M_r/M_s of 0.491 at 300 K. Table 2.1a and 2.1b show respectively the coercivity and squareness data for bulk Ni film, 290 nm Ni mesh and 180 nm Ni mesh at different temperature (5, 10, 300 and 350 K). The values of coercivity and squareness of Ni meshes are much higher than found in bulk nickel film. Such an dramatic enhancement is well known for other size-constrained magnetic systems.[169] The presently observed coercive field for Ni meshes is similar to reported for 60 nm diameter Ni nanowires,[177] and thin-film (0.5μm thick) macroporous Ni.[52] The coercivity and squareness of 290 nm Ni mesh are slightly smaller than that for 180 nm Ni mesh, due to the size effect.[52,177] Since the

a)

b)
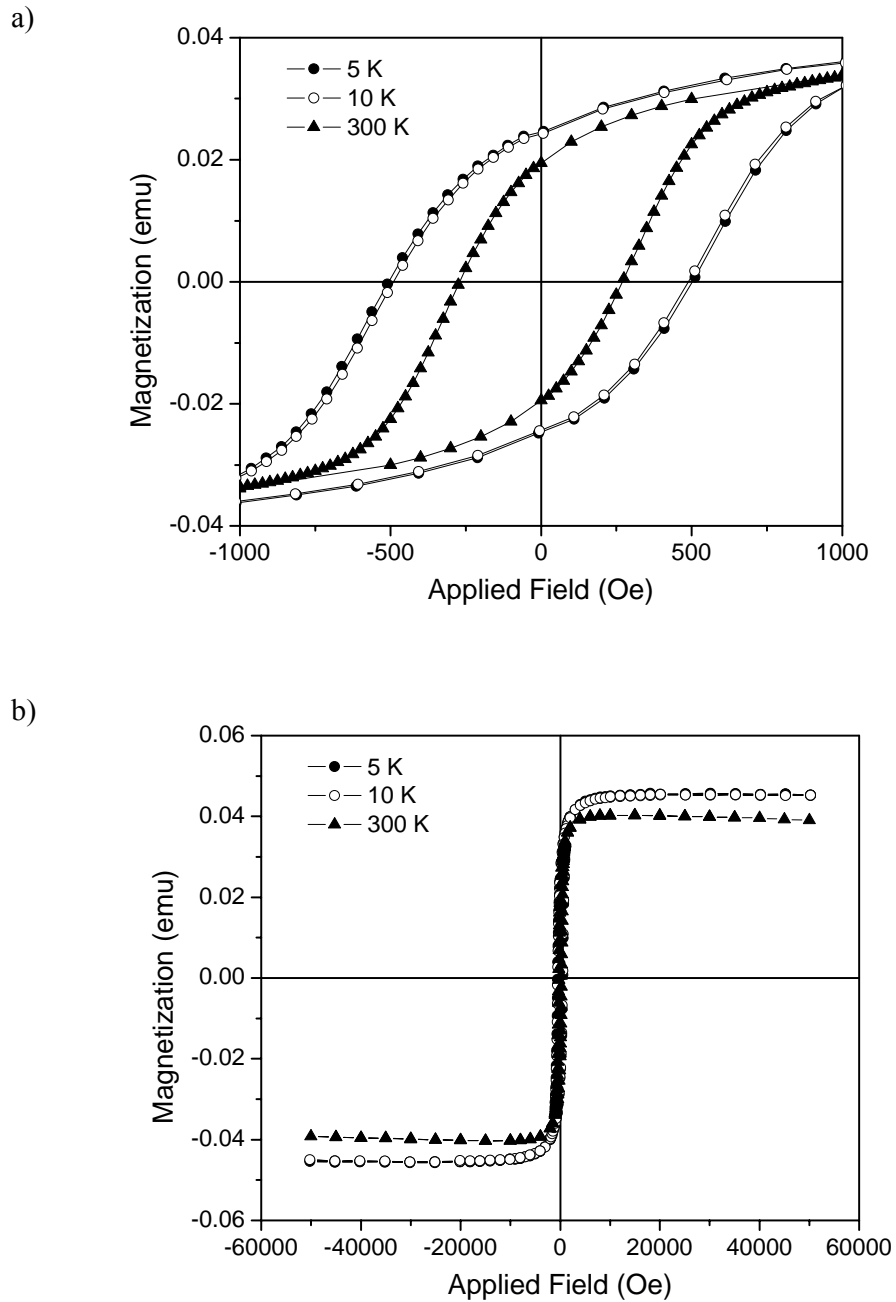
Figure 2.22. a) In-plane hysteresis loops for 180 nm Ni mesh at 5, 10, and 300 K.
b) Full range of the hysteresis loop (field range of between -50,000 to
50,000 Oe) for 180 nm Ni mesh at 5 K, 10, and 300 K.

Table 2.1. Comparison of a) coercivity, and b) squareness (M_r/M_s) for bulk Ni, 290 nm Ni mesh, and 180 nm Ni mesh at different temperature.

a)

Sample	H_c (Oe)			
	5 K	10 K	300 K	350 K
Bulk Ni	35	35	18	
290 nm Ni Mesh	426	404	211	190
180 nm Ni Mesh	506	491	271	

b)

Sample	M_r/M_s			
	5 K	10 K	300 K	350 K
Bulk Ni	0.114	0.113	0.052	
290 nm Ni Mesh	0.465	0.453	0.386	0.367
180 nm Ni Mesh	0.540	0.535	0.491	

nanoparticles in Ni meshes are connected to each other, strong dipole-dipole interactions exist. The Ni meshes show hysteresis loops even at 350 K, which is different from the pure superparamagnetic systems with very weak interparticle interactions,[178,179] but similar to the systems with very strong dipole-dipole interactions like ferromagnetic nanowires and nanoparticles assemblies.[180-183]

2.4 Conclusions

Electrodeposition in opal templates offers an effective route for the preparation of metal meshes. These metal meshes have uniformly porous structures with three-dimensional periodicity. Plating current density and pore size of templates can affect the growth of metal meshes, and better-quality metal meshes are obtained if a lower current density and an opal piece consisting of larger diameter silica spheres are applied. Due to their structures with interconnected pores, the metal meshes may be infiltrated with other materials (such as metals by melt infiltration[127]) to make specific alloys or composites. Also lower dimensional structures (such as one-dimensional corrugated metal nanowires or two-dimensional metal-mesh sheets) may be fabricated by mechanical processing like polishing.[184]

The magnetic properties of nickel mesh show size effects due to the nanometer dimensions of the components. The Ni mesh exhibits an enhanced coercivity by comparison with bulk nickel. The investigation of these new types of materials will be of significant fundamental and practical interest because of their unique structures consisting of three-dimensionally porous metal arrays.

CHAPTER 3

TEMPLATE SYNTHESIS OF METAL OXIDE MESHES

AND POLYMER MESHES

3.1 Introduction

Colloidal crystal template synthesis has been broadly applied in materials areas as it is expected to create 3D ordered macroporous (pore size > 50 nm) materials with unique physical and chemical properties. A number of macroporous materials, such as metal, metal oxide, silica, polymer, and carbon meshes have been fabricated by colloidal crystal templating method. Metal oxide and polymer meshes are two types of macroporous materials which are extensively investigated due to their facile fabrication and wide range of applications. Generally, alkoxide-based sol-gel hydrolysis,[69-87] metal salt (such as acetates and oxalates) precipitation and subsequent calcination[113-114] are used to fabricate metal oxide meshes, but it is hard to obtain dense filling of metal oxides in the opal templates by these two techniques. Direct oxidation has been reported to convert metal nanowires to metal oxide nanowires;[185] here we extend this method to fabricate NiO meshes by the oxidation of Ni meshes obtained by electrodeposition.[127,128] One advantage of synthesis of NiO meshes by direct oxidation is that higher filling fraction of NiO (~ 0.44) can be achieved comparing to NiO meshes obtained by nickel oxalate precipitation and thermal decomposition (filling fraction: ~ 0.09),[114] then the mechanical stability of as-synthesized NiO meshes increases a great deal, and thus they are more stable for

further applications, such as in catalysis,[76] and as templates for metal nanosphere fabrication (see Chapter 4).[127,128]

Polymer meshes have broad applications in a variety of areas, including photonics,[91-94, 100] biosensing,[98,186,187] catalysis,[188] and separations.[189] Chemical[91-100] and electrochemical[59-61] polymerization approaches are generally used to prepared polymer meshes through colloidal crystal templating. Other methods include electroless polymerization,[190] and infiltration of polymer solutions.[191] Due to the plastic nature of polymers, the polymer meshes usually have highly uniform porous structures and are also stable enough for further applications, such as used as templates for nanosphere fabrication.[85,97,192]

In this chapter, we demonstrate the fabrications of NiO meshes by direct oxidation of Ni meshes, conductive polyaniline meshes by electrochemical polymerization, and nonconductive PMMA mesh by chemical polymerization. Also, the formation of pressed PMMA meshes containing oblate pores by the compression of PMMA meshes is reported.

3.2 Experimental Section

3.2.1 Materials

All solvents and chemicals were of reagent quality and were used as received. Na_2SO_4 (99.99%, Aldrich), H_2SO_4 (99.999%, Aldrich), HF solution (48%, Aldrich), methyl methacrylate (99%, Aldrich), aniline (99.5%, Aldrich), benzoyl peroxide (97%, Aldrich), dichloromethane (99.5%, EM Science), acetone (99.7%, Mallinckrodt).

3.2.2 Synthesis of NiO Meshes

We first sputtered a Au film (ca. 1 μm thick) onto one side of an opal piece (typically 7×10×1.5 mm), then Ag paste (Ted Pella, Inc.) was used to attach a length

of Cu wire to the Au film, and finally the Au/wire side of the electrode, as well as the edges, were covered with an insulating glue (Scotch Super Strength, 3M).

Using the opal membrane as the working electrode, versus a Pt wire counter electrode, Ni was deposited galvanostatically into the opal template at a current density of 0.12 mA/cm^2. The Ni electroplating solution (Nickel Sulfamate RTU, Ni(H$_2$NSO$_3$)$_2$ solution) was obtained commercially (Technic, Inc.). The deposition time was 144 hours (*ca*. 80 µm thick nickel deposited).

After the deposition, the Ni/opal sample was attached to a polishing wand, and polished with a piece of silicon carbide paper (600) to remove silica layers that had not been infiltrated with nickel. When the nickel mesh layer was nearly reached, the polishing was then carefully continued with a piece of silicon carbide paper (1200/4000) until reaching the surface of nickel mesh layer. The sample appearance changed from opalescent white (opal) to opalescent black (nickel/opal composite). Freestanding porous Ni mesh could be obtained by etching away the opal template with a 2% HF solution for 2 hours.

Then the Ni mesh was put in a crucible and annealed in a tube furnace (TF 55035A-1, Lindberg/Blue M). NiO mesh was obtained by slowly oxidizing the Ni mesh in open air to 550ºC at 1ºC /min., followed by an 8-hour isotherm. Then the NiO mesh was cooled slowly to room temperature in the furnace. Under similar procedure, NiO mesh with annealing temperature of 650ºC was also fabricated.

3.2.3 Electrodeposition of Conductive Polyaniline Mesh

3.2.3.1 Electroplating Solution

The prepared plating solution contained 40 g/liter aniline, 70 g/liter Na$_2$SO$_4$, and 62 g/liter H$_2$SO$_4$, and had a pH ~ 1.0.

3.2.3.2 Synthesis of Polyaniline Mesh

Using the opal membrane as the working electrode, versus a Pt wire counter electrode, electropolymerisation was carried out galvanostatically inside the opal template at a current density of 0.50 mA/cm^2, over a 48-hour period. After the electrochemical deposition was complete, the opal template was removed by soaking the polyaniline/opal film in 2% HF solution for 12 hours, resulting in freestanding polyaniline mesh with black opalescent color.

3.2.4 Chemical Polymerization of Nonconductive PMMA Mesh

A piece of opal was immersed in methyl methacrylate (MMA) monomer with 1 wt.% benzoyl peroxide (BPO) as an initiator. Polymerization was initially carried out at 40°C for 10 hrs and then 60°C for 12 hrs. Excess poly(methyl methacrylate) (PMMA) on the opal surfaces, was removed by wiping the exposed opal surface clean with dichloromethane (CH_2Cl_2). Then, the PMMA/opal composite was immersed in 10% HF solution for 12 hrs to remove silica spheres, resulting in freestanding PMMA mesh structure. The PMMA mesh was washed thoroughly with distilled water, then was either kept in distilled water for later preparation of compressed PMMA mesh or dried in air for SEM observation.

3.2.5 Preparation of Compressed PMMA Mesh with Oblate Pores

A piece of PMMA mesh was placed between two metal plates and filled with distilled water. By the use of a laboratory press (Fred S. Carver, Inc.), a pressure (~ 5 tons) was then applied to the top metal plate to deform the PMMA mesh, resulting in the formation of compressed PMMA mesh with oblate pores, instead of the spherical pores of original PMMA mesh. Then the compressed PMMA mesh was dried in air for the SEM observation.

3.2.6 Characterization

3.2.6.1 Scanning Electron Microscopy Characterization

Scanning electron microscopy (SEM) and energy dispersive X-ray spectroscopy (EDX) analysis were performed on a JEOL JSM 5410 SEM. The samples were affixed to conductive carbon tape and loaded on specimen mounts for SEM. For PMMA mesh and compressed PMMA mesh, a thin-layer (~ 4 nm) of Au was puttered onto the surface of samples before the SEM observation.

3.2.6.2 Transmission Electron Microscopy Characterization

Transmission electron micrographs (TEM) and electron diffraction patterns were obtained by using a JEOL 2010 TEM operating at 200 kV. The samples were prepared by mounting small pieces of mesh on TEM copper grid and directly loaded in TEM for observation.

3.3 Results and Discussion

3.3.1 Synthesis and Characterization of NiO Meshes

In the preparation of Ni mesh (inverse Ni opal), a low plating current density (0.12 mA/cm^2) was used for the even growth of nickel within the opal membrane. The thickness of the Ni mesh film can be controlled by simply adjusting the deposition time. After the deposition, the silica part with no Ni deposited of the Ni-mesh/opal sample was removed by polishing to show the Ni/silica composite surface. Such a step is necessary for the preparation of uniform Ni and NiO mesh. Since the thickness of opal piece (~ 1.0 mm) is far more than that of Ni mesh (~ 80 µm), in order to reduce the dissolution of Ni when etching away of opal by dilute HF acid, we used a grinding paper to polish the Ni filled opal until Ni appears on the surface. Then opal template could be removed in a relatively short time to get freestanding Ni mesh. It

takes about 2 hours to completely etch away the opal in the polished Ni/opal sample (around 80 µm thick) by 2% HF solution, while 12 hour is needed for the complete removal of opal in the pre-polishing sample, thus higher-quality Ni mesh can be obtained by the polishing.

NiO mesh can be readily obtained by annealing the Ni mesh in open air. In the annealing, we raised the temperature to 550ºC at a low rate of 1 ºC/min to ensure the even oxidation of Ni mesh, then the sample was kept at 550ºC for 8 hours to completely convert the Ni to NiO. Semiquantitative analysis with EDX shows a stoichiometry of approximately 1:1 (Ni:O) for the NiO mesh (Figure 3.1). After annealing, the mesh could not be attracted by a strong magnet, which indicated that the Ni was well oxidized. Figure 3.2a shows a representative SEM image of 290 nm NiO mesh surface (5,000 ×). Figure 3.2b and 3.2c reveal 290 nm NiO mesh with predominately (111) orientation (10,000 ×), and (100) orientation (20,000 ×), respectively. Figure 3.2d shows SEM image of a piece of 220 nm NiO mesh (20,000 ×). These meshes are quite uniform and good for further applications, such as used as templates for the fabrication of metal sphere arrays.[127,128]

The size of the pores in the NiO mesh became smaller due to the oxidation of Ni mesh. If one assumes that the overall dimensions of the mesh piece do not vary with oxidation and that the volume changes that do occur only go to reduce the internal void volume of the mesh, then one can estimate the expected change in the internal void space by considering the formula weights (FW) and densities (D) of Ni (FW: 58.69, D: 8.902 g/cm^3) and NiO (FW: 74.71, D: 6.67 g/cm^3). Based on these values, the fraction of space occupied by the Ni mesh (~0.26) would be expected to increase to *ca.* 0.44 for the NiO mesh. The higher filling fraction of NiO mesh makes it more mechanically stable than the NiO meshes fabricated by other methods like

```
Label:NiO Mesh

kV:20.0      Tilt:0.0     Take-off:23.1    Det Type:SUTW+    Res:137      Tc:40

FS : 393     Lsec : 50                                      30-Aug- 1     10:25:25
```

| | | | 2.00 | 4.00 | 6.00 | 8.00 | 10.00 | 12.00 | 14.00 | 16.00 | 18.00 |

```
EDAX ZAF Quantification (Standardless)
Element Normalized

Element    Wt %     At %    K-Ratio    Z        A        F
   O K    20.18    48.13   0.0764    1.1080   0.3409   1.0025
   NiK    79.82    51.87   0.7734    0.9638   1.0053   1.0000
 Total   100.00   100.00
```
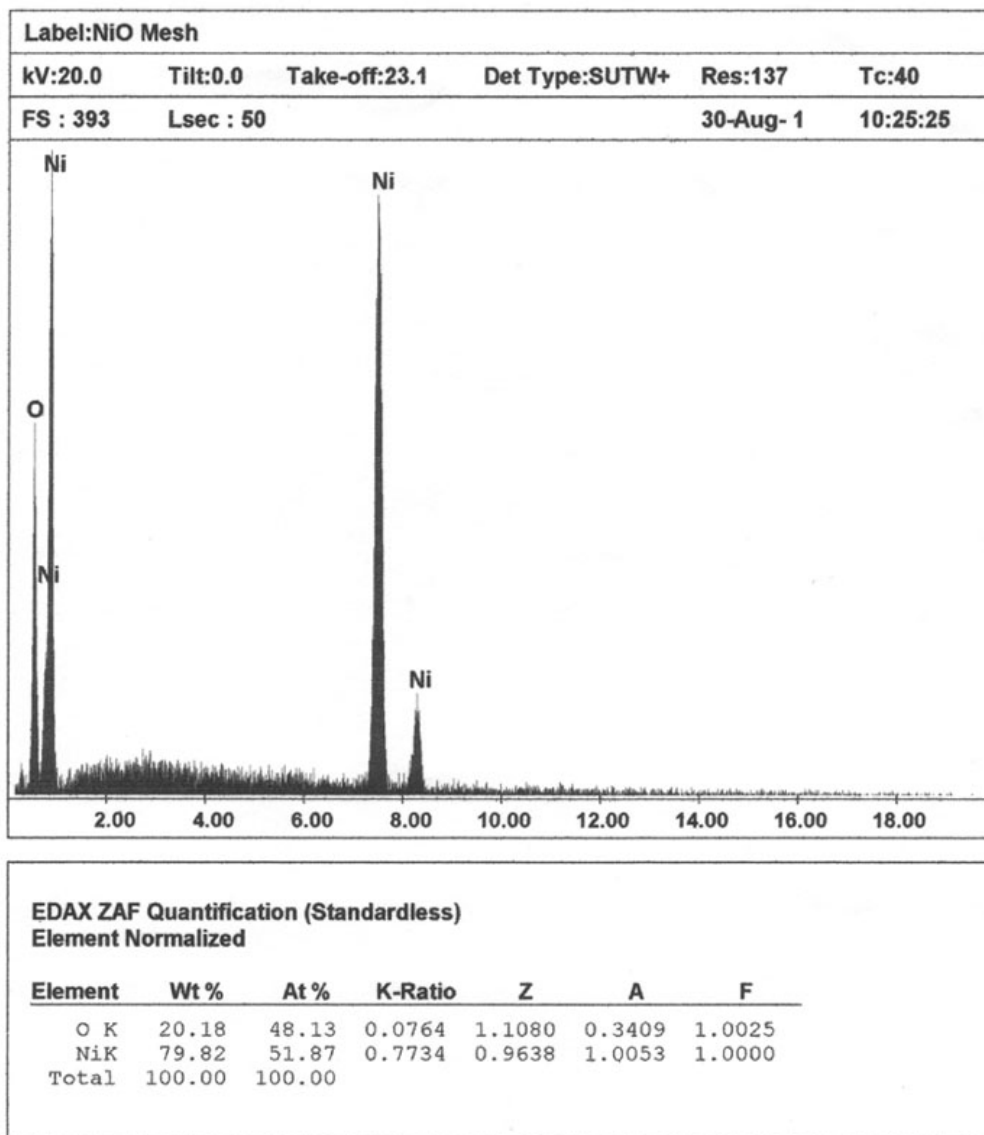
Figure 3.1. EDX spectra of NiO mesh.

Figure 3.2. SEM photographs of a) 290 nm NiO mesh at magnification of 5,000,
b) 290 nm NiO mesh predominately along the 111 direction ($\times$ 10,000),
c) 290 nm NiO mesh along 100 direction ($\times$ 20,000),
d) 220 nm NiO mesh ($\times$ 20,000).

a)
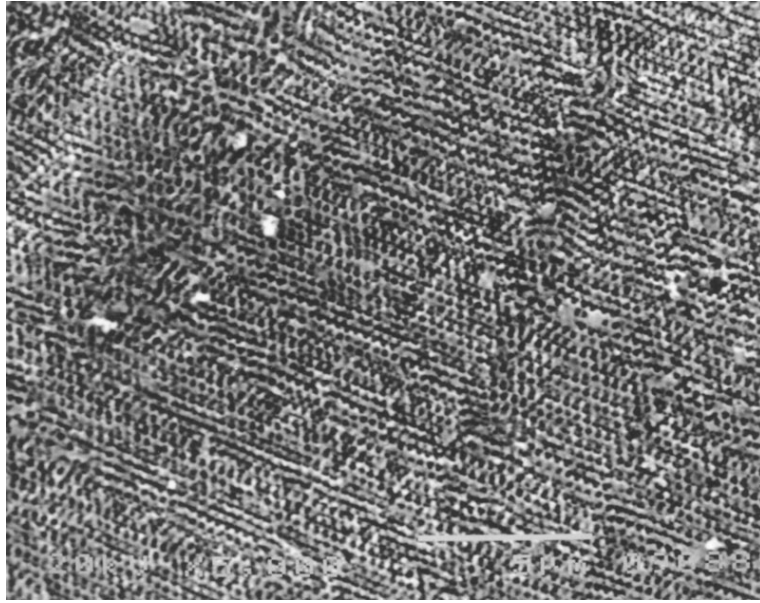
b)
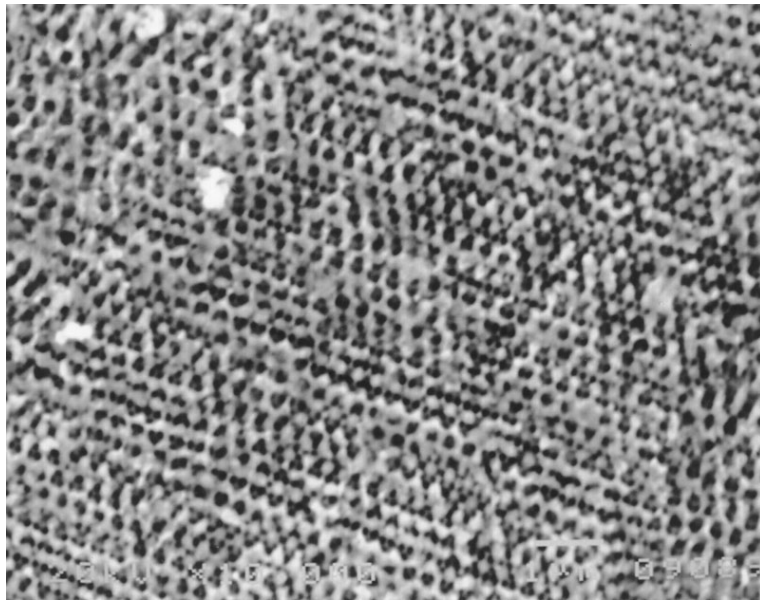
c)
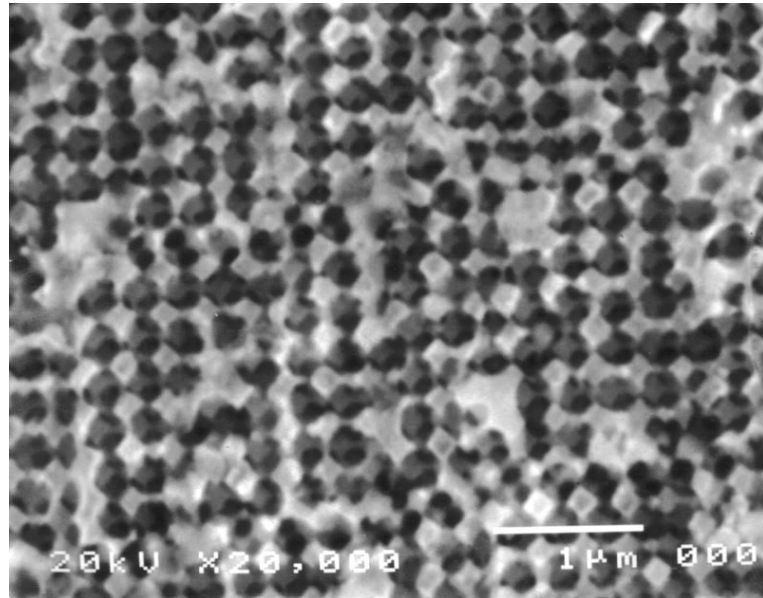
d)
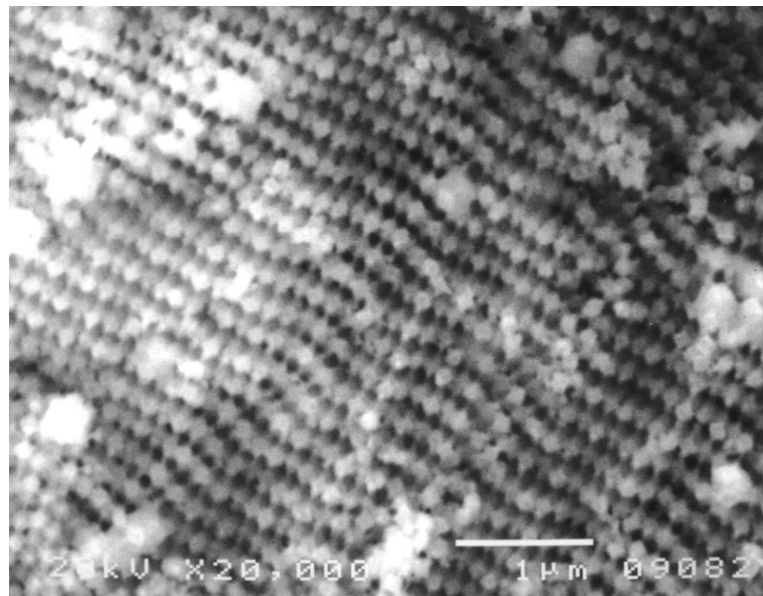
nickel oxalate precipitation and thermal decomposition which produces NiO meshes with a very low filling fraction (~ 0.09).[113,114]

The annealing process turned the Ni membrane completely into a mesh consisted of NiO nanograins. Figure 3.3a is the (111) TEM image of the mesh. All of the mesh now was composed of fused NiO nanograins with an average diameter of 20 nm. Figure 3.3b is the selected area electron diffraction (SAED) pattern of the NiO membrane with face-centered cubic (fcc) structure. The structure is quite different from that reported by Yan *et al.*, who obtained crystalline hexagonal NiO mesh by salt-precipitation and chemical conversion method.[113] Further annealing of the NiO membrane at 650ºC induced the NiO nanograins to grow bigger. TEM picture as shown in Figure 3.3c shows that NiO nanograins grew into a size of 50-80 nm. The higher temperature treatment made NiO membrane more stable for further applications.

3.3.2 Synthesis of Conductive Polymeric Meshes

Conductive polymeric meshes can be synthesized by either chemical or electrochemical polymerization. The latter is generally preferred because it provides better control of film thickness and morphology. Polyaniline is one of the most extensively investigated conductive polymers. In our experiments, we successfully fabricated conductive polyaniline mesh using opal template by electrochemical polymerization. The polyaniline was infiltrated into opal under acidic condition (shown in equation 3.1) through anodic oxidation. Then the opal was removed by

$$ (3.1) $$

a)

b)

c)
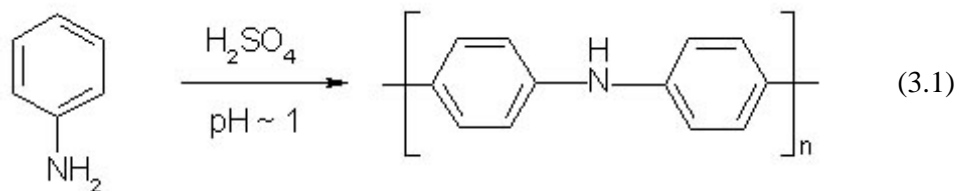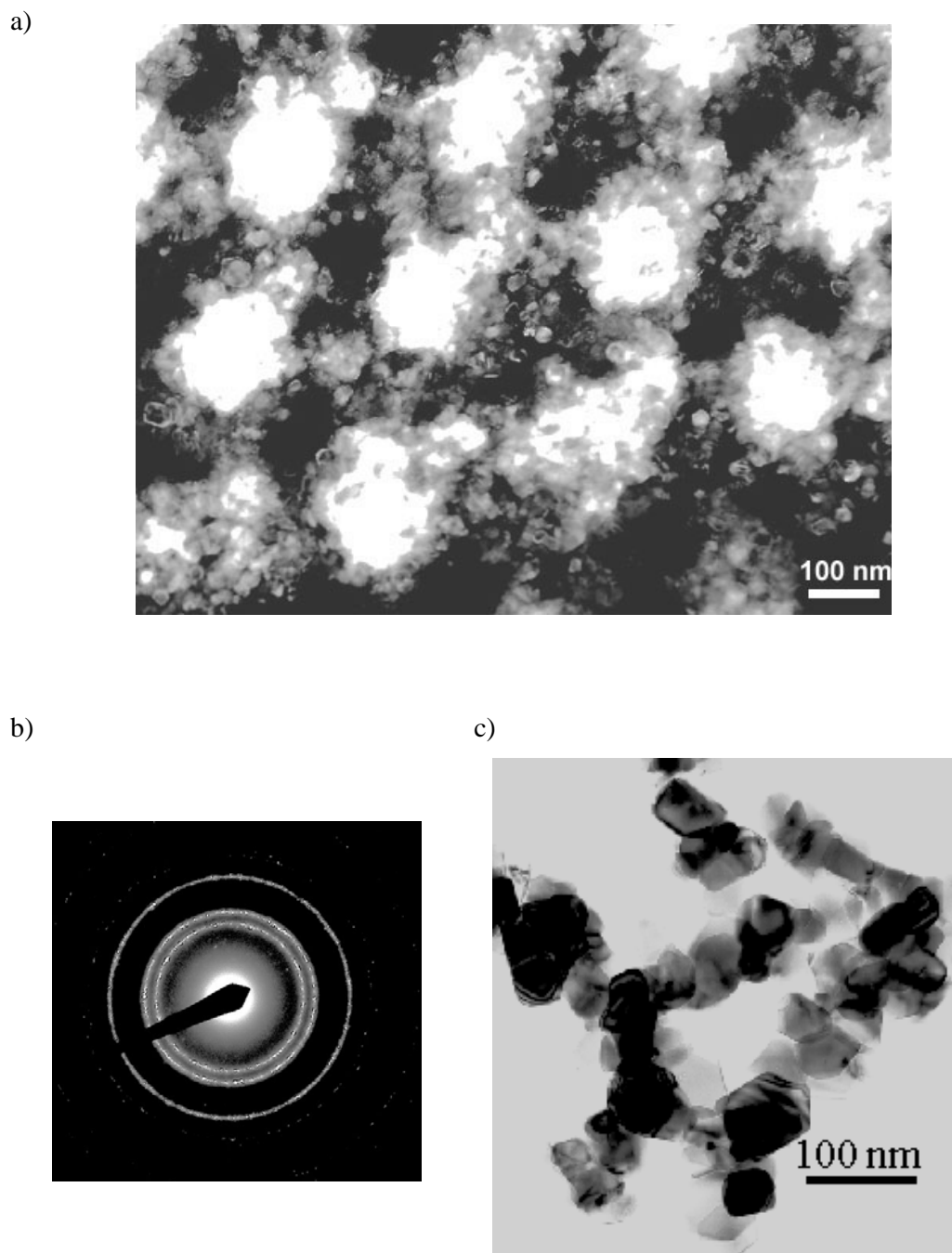
Figure 3.3. a) TEM image of 290 nm NiO mesh obtained by annealing Ni mesh at 550
ºC. b) Electron diffraction pattern of NiO mesh. c) TEM image of a single
macropore with NiO pore wall obtained by annealing Ni mesh at 650 ºC.
(In TEM images, darker regions represent NiO nanoparticles).

dilute HF solution to produce freestanding polyaniline mesh. The black polyaniline

mesh shows opalescent color under the illumination of white light.

Figure 3.4 shows SEM image of a piece of polyaniline mesh made from a 290

nm diameter silica opal template. It is obvious that the polyaniline mesh has three-

dimensionally ordered porous structure. The three-dimensional periodicity extends

over long range.

3.3.3 Synthesis of Nonconductive PMMA Meshes

Nonconductive PMMA poly(methyl methacrylate) meshes can be fabricated

by chemical polymerization of MMA (methyl methacrylate) monomer inside the void

space of opal, followed by the removal of opal template by dilute HF solution. In the

polymerization process (shown in equation 3.2), BPO (benzoyl peroxide) was used as

the initiator for the free radical synthesis of PMMA. The polymerization can be

carried out by either heating or UV (ultra-violet) irradiation. Thermopolymerization

was used to synthesis PMMA mesh in our experiments. The reaction temperature was

easily controlled by a furnace, and PMMA was readily obtained by heating at 60°C

for a few hours.

(3.2)
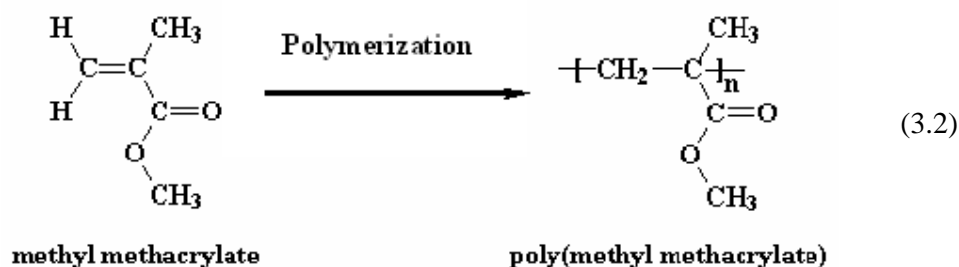
The filling of PMMA inside the void space opal was quite complete, and

nearly all the interstices in the whole opal piece were occupied by PMMA, which is

different from the infiltration process of electrodeposition. By electrochemical

deposition, the thickness of materials being deposited can be controlled by varying the
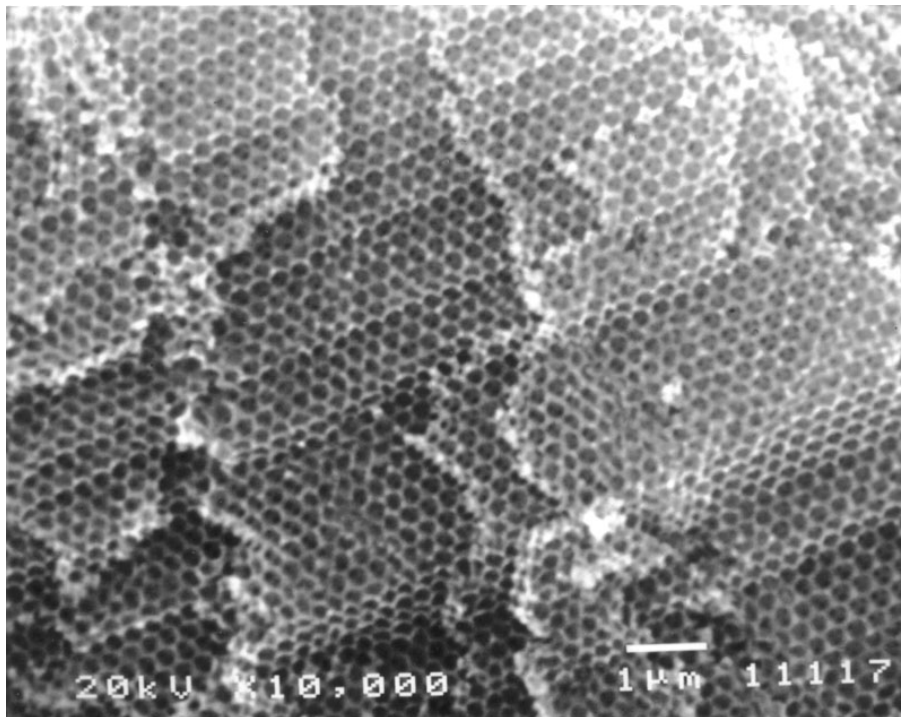
Figure 3.4. SEM picture of 290 nm polyaniline mesh ($\times$ 10,000).
.

time and current, while by chemical polymerization, nearly all the voids in the whole

volume of the template are filled by polymer. Figure 3.5a shows the cross-sectional

SEM image ($\times$ 10,000) of PMMA mesh made from opal consisting of 290 nm

diameter silica spheres, and Figure 3.5b is a higher magnification of the PMMA mesh

in (111) orientation. The PMMA mesh contains highly uniform macropores and a

triangular pattern below each pore of the surface layer of (111) orientation region can

be seen clearly, indicating that PMMA mesh consists of 3D ordered porous structures.

Since PMMA is glassy, the pore wall of PMMA mesh is smooth compared with that

of metal and metal oxide meshes consisting of crystalline metal or metal oxide. Dilute

HF solution can completely remove the silica spheres in opal template, based on the

SEM image and EDX analysis, which detected no Si signal in the PMMA mesh. Since

opal templates can be made with variable silica sphere sizes, as well as thicknesses,

the resulting polymeric meshes have easily controlled void volume and thickness.

Also the PMMA meshes, which are white themselves, can strongly diffract white light

and exhibit opalescent colors.

3.3.4 Synthesis of Compressed PMMA meshes

Silica opal is brittle and thus further processing is impossible. In contrast,

polymer mesh is soft and can be deformed by stretching or pressing to produce

polymer mesh with oblate pores. Jiang *et al.* fabricated ellipsoidal polystyrene mesh

by heating the polystyrene mesh filled with mineral oil above the glass transition

temperature of polystyrene (94°C) and stretching.[192] Sumioka *et al.* stretched PMMA

mesh fill with hot water (87°C) to obtain deformed PMMA mesh.[193] In our

experiments, we applied a pressure on the surface of PMMA mesh film by simply

using a laboratory press at room temperature. The pressure can be controlled by the

press, and thus the deformation of PMMA mesh can be also controlled.

a)

b)
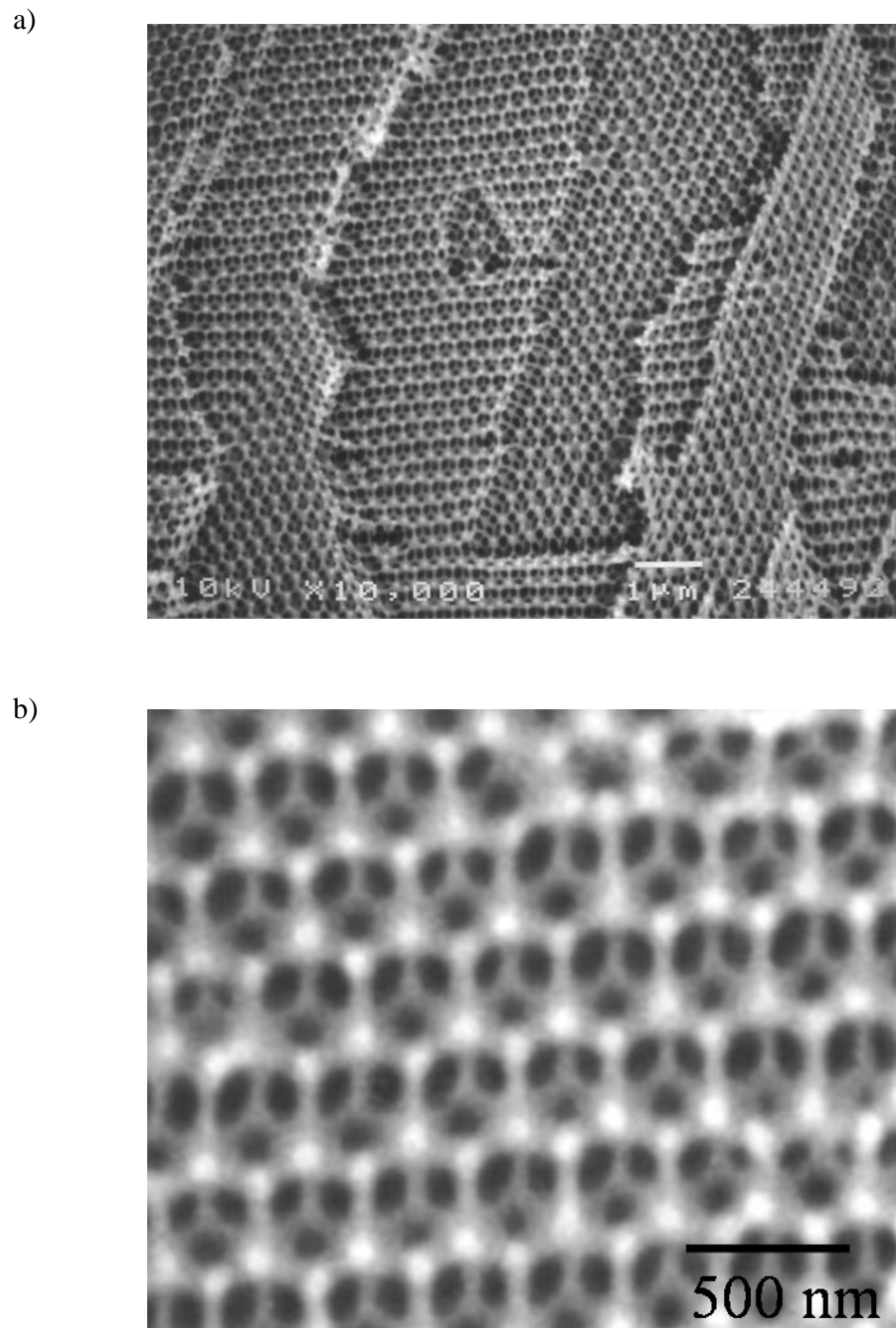
Figure 3.5. a) SEM image of PMMA mesh ($\times$ 10,000). b) A higher magnification of PMMA mesh with (111) orientation showing uniform porous structure.

Figure 3.6 shows the SEM pictures of compressed PMMA mesh obtained by pressing water-filled PMMA mesh containing 290 nm diameter pores. Oblate textures that represent deformed air spheres in the PMMA mesh can be observed. Three-dimensional periodicity of original PMMA mesh is still retained. In contrary to the original PMMA mesh which reflects green light, the compressed PMMA mesh reflects blue light, indicating a decrease in the lattice spacing of selective reflection.[193] Thus the optical properties of PMMA meshes are tunable by if the deformation is well controlled.

3.3 Conclusions

Three-dimensionally periodic NiO meshes were successfully fabricated by directed oxidation of Ni meshes in the air. The nanocrystalline sizes of NiO particles can be adjusted by temperature. Lower-temperature treatment of Ni meshes leads to NiO meshes with smaller nanograins, but having higher total surface areas. More mechanically stable NiO meshes are obtained by annealing NiO meshes at higher temperature. Using opal templates, ordered conductive polyaniline meshes were synthesized by electrochemical polymerization of aniline monomer in acidic solution. Well-defined nonconductive PMMA meshes were produced from chemical polymerization of MMA monomer inside opal templates. These polymer meshes show highly uniform porous structures with 3D periodicity. Also, compressed PMMA meshes with oblate pores could be formed by the deformation of PMMA meshes with pressure. One important application of these meshes is that they can be used as further templates to fabricate new types of 3D ordered sphere arrays (colloidal crystals) with technologically important properties (refer to Chapter 4).[97,127,128,192]

a)
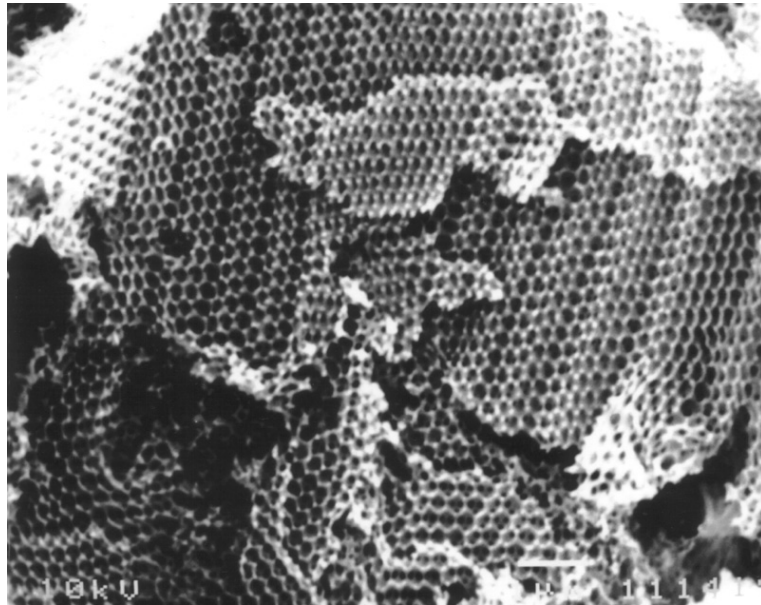
b)
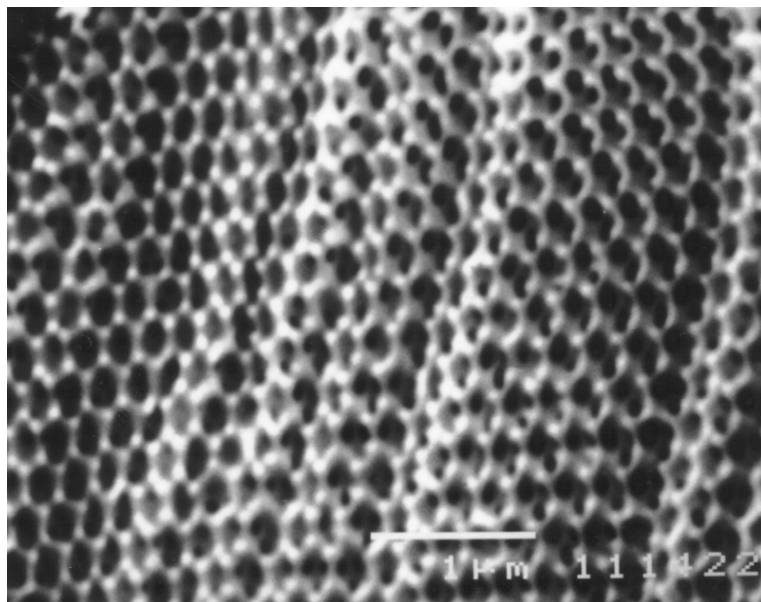
Figure 3.6 SEM images of compressed PMMA mesh with magnification of a) $\times$
10,000, b) $\times$ 20,000.

CHAPTER 4

TWO-STEP TEMPLATE SYNTHESIS OF

METAL SPHERE ARRAYS

4.1 Introduction

Two-step template synthesis has been previously applied to prepare one-dimensionally ordered nanohole arrays.[194-197] Recently, this approach was extended to fabricate three-dimensional (3D) nanoscale structures.[85,95,97,127,128,192,198-205] By the use of opal (colloidal crystal with ordered silica or latex spheres) as a template, inverse opal can be fabricated by established methods described in Chapter 1. Then the inverse opal can be further used as a mold to synthesize diverse nanosphere arrays (colloidal crystals) and nanocomposites, such as silica,[95,198] metal oxide,[85,192,198-201] and metal sphere arrays[97,127,128,205] and carbon/metal,[127] carbon/semiconductor,[127] carbon/polyaniline,[202] and ferromagnetic/ ferroelectric composites.[203] These new types of materials, which are hard to produce by other techniques, have potential applications in a variety of areas, including photonics,[23] gas sensing,[85,200] and magnetics.[97,206]

A number of methods like sol-gel hydrolysis,[85,192,198-201,203] electrochemical deposition[97,127,128,202,205] and melt infiltration[127] have been employed to fabricate nanosphere arrays and nanocomposites. In our group, we mainly use electrochemical deposition technique to synthesize metal nanosphere arrays.[97,127,128,205] Electrodeposition offers an effective method for producing metal sphere arrays, due to

the nearly complete filling of the channels of porous templates and easy control of the

extent of metal growth. In this chapter, we describe the two-step template synthesis

of metal sphere arrays.[97,127,128,205] First, NiO mesh or poly(methyl methacrylate)

(PMMA) mesh was prepared from an opal template. Then, using the poorly

conductive NiO mesh or PMMA mesh as a mold, highly ordered metal nanospheres

were readily obtained by electrochemical deposition. Also, angle-dependent magnetic

properties of Ni and Co sphere arrays were investigated.

4.2 Experimental Section

4.2.1 Materials

All solvents and chemicals were of reagent quality and were used as received.

$CoSO_4 \cdot 7H_2O$ (99.998%, Aldrich), NaCl (100.2%, J. T. Baker), HF solution (48%,

Aldrich), H_3BO_3 (99.8%, EM Science), H_2SO_4 (95.0-98.0%, EM Science), methyl

methacrylate (99%, Aldrich), benzoyl peroxide (97%, Aldrich), dichloromethane

(99.5%, EM Science), acetone (99.7%, Mallinckrodt), ethyl alcohol (99.5%, Aldrich).

4.2.2 Electrodeposition of Metal Sphere and Oblate Sphere Arrays

4.2.2.1 Electroplating Solutions

The commercial *Ni* (Nickel Sulfamate RTU, $Ni(H_2NSO_3)_2$ solution, pH ~ 4.0),

Pd (Pallaspeed VHS, 3.97% $(NH_2CH_2CH_2NH_2)_2PdSO_4$ solution, containing 5.3 g/liter

palladium, pH ~ 6.0), and *Au* (Orotemp 24 RTU, $KAu(CN)_2$ solution, containing 8.2

g/liter gold, pH ~ 8.0) electroplating solutions were obtained from Technic Inc.

Co plating solution: 200 g/liter $CoSO_4 \cdot 7H_2O$, 6 g/liter NaCl, 40 g/liter H_3BO_3,

pH ~ 3.5

4.2.2.2 Synthesis of Metal Sphere Arrays Using NiO Mesh Template

Synthesis of NiO Mesh. Three-dimensionally ordered Ni mesh was fabricated

by first electrodepositing Ni into the opal template at a current density of 0.12

mA/cm^2 over a 144-hr period (*ca*. 80 μm thick nickel deposited), then polishing to

remove silica layers that had not been infiltrated with nickel until reaching the Ni

mesh layer, and finally removing the opal template with dilute HF solution. Poorly-

conductive NiO mesh was obtained by slowly oxidizing the Ni mesh in open air to

550 ºC at 1 ºC /min., followed by an 8-hour isotherm. More details are described in

Chapter 3.

     Synthesis of Metal Sphere Arrays. The poorly conductive NiO mesh was then

used as an electrode (the sputtering gold backing still in place) after the copper wire

and insulating glue (Scotch Super Strength, 3M) were reapplied. The NiO mesh was

filled with metals by galvanostatic electrodeposition using a Pt wire counter electrode

and a Potentiostat/Galvanostat (EG&G Model 263A). Figure 4.1 shows the set-up for

electrodeposition of metals in NiO mesh membrane. The current density is usually

smaller than 0.6 mA/cm^2, and the deposition time is larger than 12 hours. After the

deposition, the NiO mesh was removed in a boiling dilute sulfuric acid solution (20%

v/v, 15 min.), resulting in ordered metal sphere arrays.

4.2.2.3 Synthesis of Metal Sphere Arrays Using PMMA Mesh Template

     Preparation of PMMA Infiltrated Opal. The PMMA infiltrated opal was

prepared by chemical polymerization of methyl methacrylate (MMA) monomer inside

the opal piece. Excess poly(methyl methacrylate) (PMMA) on the opal was removed

by wiping the exposed opal surface clean with dichloromethane (CH$_2$Cl$_2$). More

details are described in Chapter 3.

     Fabrication of PMMA Mesh Electrode. A Au film (*ca*. 1 μm thick) was

sputtered onto one side of a piece of PMMA/opal, then Ag paste (Ted Pella, Inc.) was

used to attach a length of Cu wire to the Au film, and finally the Au/wire side of the
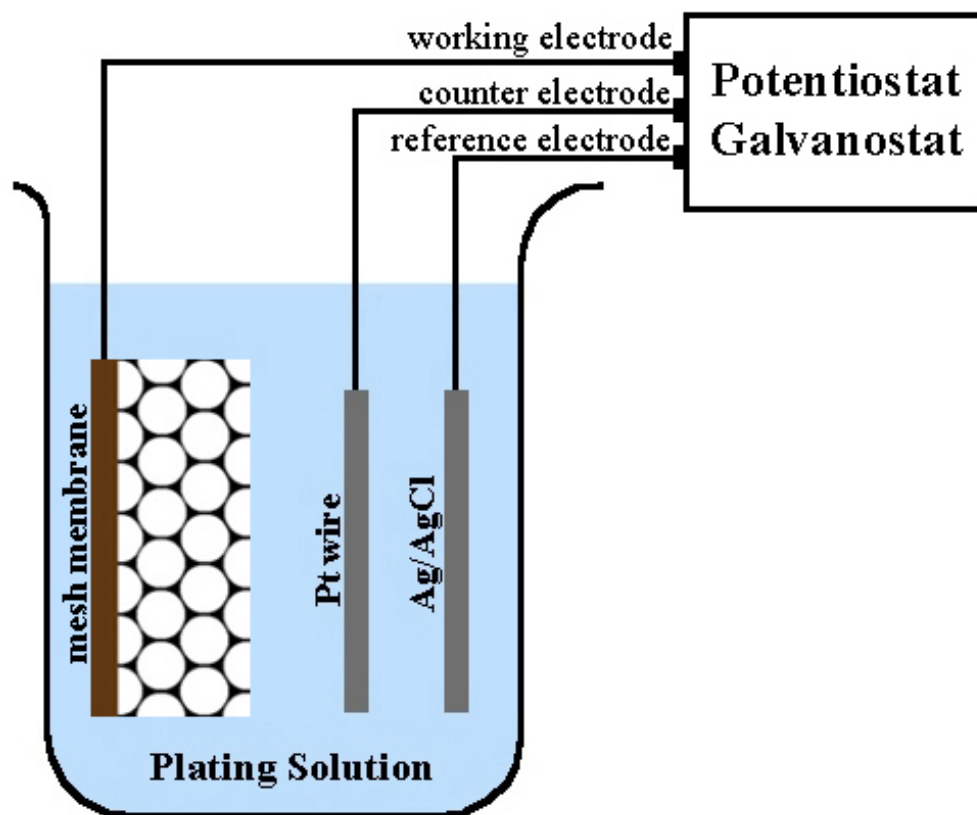
Figure 4.1.   Set-up for electrodeposition of metals in mesh membrane.

electrode, as well as the edges, were covered with an insulating glue (3M). The silica

opal spheres were removed using a 10 wt.% HF solution (12 h) to obtain a

freestanding PMMA mesh (inverse opal). This PMMA mesh was kept in water for

later use as working electrode in electrodeposition.

Synthesis of Metal Sphere Arrays. The PMMA mesh was filled with metals by

galvanostatic electrodeposition using a Pt wire counter electrode and an EG&G

Model 263A Potentiostat/Galvanostat (Figure 4.1). The current density is 0.8

mA/cm^2 for Ni or Co deposition and 0.6 mA/cm^2 for Pd deposition; the plating times

were all 48 hrs. After the electroplating process, freestanding metal sphere arrays

were obtained by etching away the PMMA template with warm CH_2Cl_2. The

thickness of a typical metal colloidal crystal was about 60 μm.

4.2.2.4 Synthesis of Oblate Metal Sphere Arrays Using Compressed Mesh Template

Preparation of Compressed PMMA Mesh. Compressed PMMA mesh was

prepared by applying a pressure on the surface of PMMA mesh, which was filled with

water. The resulted compressed PMMA mesh was dried in air. More details are

described in Chapter 3.

Fabrication of Compressed PMMA Mesh Electrode. A Au film (*ca*. 0.5 μm

thick) was sputtered onto one side of a piece of compressed PMMA, then Ag paste

(Ted Pella, Inc.) was used to attach a length of Cu wire to the Au film, and finally the

Au/wire side of the electrode, as well as the edges, were covered with an insulating

glue (3M). The electrode was immersed in 50% (v/v) EtOH solution for 24 hours to

make the PMMA pore wall hydrophilic, and then the electrode was kept in distilled

water for later use as working electrode in electrodeposition.

Synthesis of Oblate Metal Sphere Arrays. The compressed PMMA mesh was

filled with metals by galvanostatic electrodeposition using a Pt wire counter electrode

and an EG&G Model 263A Potentiostat/Galvanostat (Figure 4.1). For Ni deposition,

the current density is 0.4 mA/cm^2 and the plating time was 96 hrs. After the

electroplating process, freestanding oblate metal sphere arrays were obtained by

etching away the compressed PMMA template with warm CH_2Cl_2.

4.2.3 Fragmentation of Metal Sphere Arrays

The metal sphere array samples were put in distilled water. Then sonication

was carried out in a 75 W ultrasonic bath (Branson 1510) to disintegrate the large

piece of metal sphere array into smaller pieces, sphere arrays, or isolated spheres.

Pieces of the colloidal crystals were deposited on conducting ITO (Indium Tin Oxide)

glass substrate for SEM observation.

4.2.4 Characterization

4.2.4.1 Scanning Electron Microscopy Characterization

Scanning electron microscopy (SEM) and energy dispersive X-ray

spectroscopy (EDX) analysis were performed on a JEOL JSM 5410 SEM. The

samples were affixed to conductive carbon tape and loaded on specimen mounts for

SEM.

4.2.4.2 Optical Image

Optical picture was taken by a Sony DSC-S75 digital camera with 3.3-

megapixel CCD, 3× optical zoom lens and 2× digital zoom under a white light

illumination.

4.2.4.3 X-Ray Diffraction Characterization

Powder X-ray diffraction (XRD) data were collected between 5º and 118º 2θ

(step = 0.02º with a 1 s count time) on an automated Philips X'Pert-MPD

diffractometer equipped with copper radiation (λ = 1.5418 Å) and a graphite attached

monochromator. X-ray diffraction measurements were made on sample membranes to

the sample holder using a double-face tape.

4.2.4.4 Magnetic Properties

The angular dependence of hysteresis loops for Ni and Co sphere arrays

obtained from PMMA mesh template was measured at room temperature on thin

sample plates (3 mm x 3 mm x 60 μm) using a Lakeshore 735 vibrating sample

magnetometer (VSM). For out-of-plane angular variation measurements, the magnetic

field was applied at an angle between the field direction and the normal to the plate

plane; for in-plane angular variation measurements, the magnetic field was applied in

the plate plane but at an angle between the field direction and one axis of the plate

plane. The maximum applied field was ± 10,000 Oe.

The temperature dependence of hysteresis loops for ordered Ni sphere arrays

was studied at various temperatures (5 K, 50 K, 300 K) in external fields up to ±

50,000 Oe using an MPMS-5S superconducting quantum interference device (SQUID)

magnetometer. The procedure is similar to that described in Chapter 2.

4.3 Results and Discussion

4.3.1 Schematic Procedure for Two-Step Templating Method

Figure 4.2 shows schematic views of the procedure for the fabrication of

ordered metal sphere arrays (metallic colloidal crystals). There are two replication

steps in the fabrication process. In the first templating process, opal consisting of

three-dimensionally ordered silica spheres was used as a template to fabricate Ni

mesh (Figure 4.2a) by electrodeposition or PMMA mesh (Figure 4.2b) by chemical

polymerization of MMA monomer. Freestanding inverse opals (Ni mesh and PMMA

a)

| opal | Ni infiltrated opal | Ni mesh | NiO mesh | metal infiltrated NiO mesh | metal sphere arrays |

b)

| opal | PMMA infiltrated opal | PMMA mesh | metal infiltrated PMMA mesh | metal sphere arrays |
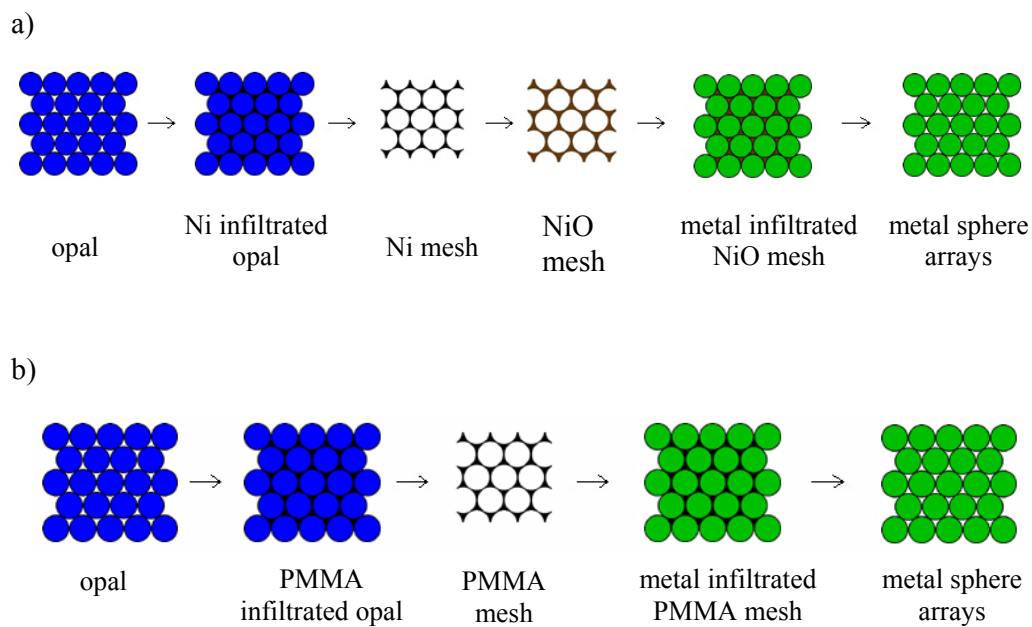
Figure 4.2. Schematic of two-step replication process for the fabrication of metal sphere arrays. a) NiO mesh used as the second-step template, b) PMMA mesh used as the second-step template.

mesh) were obtained by etching away the opal template in dilute HF solution. Then
conductive Ni mesh was oxidized in the air to form poorly conductive NiO mesh.

In the second templating process, the poorly conductive NiO mesh or PMMA
mesh was further used as a nanomold for the electrochemical growth of 3D periodic
metal spheres in the macropores of NiO mesh (Figure 4.2a) or PMMA mesh (Figure
4.2b). The templates were then removed by acidic solutions (for NiO mesh) or
organic solvents (for PMMA mesh) to produce freestanding metal sphere arrays; or
the templates were kept intact to form specific metal/metal oxide and metal/polymer
composites, which are hard to otherwise fabricate.

Since in our experiments the metal sphere arrays were synthesized by
electrodeposition, the second-step template needs to be poorly conductive, otherwise
the electrochemical growth of metal preferentially occurs on the surface of mesh.
Also due to the interconnection of macropores in a mesh, the electroplating solution
can effectively diffuse through the poorly conductive mesh to reach the
microelectrode, and then the electrodeposition starts from the electrode and grows out
towards the exposed surface of mesh.

4.3.2 Metal Sphere Arrays from NiO Mesh Templates

Well-defined NiO mesh was fabricated by slowly oxidizing Ni mesh in open
air. In order to obtain high quality NiO mesh, we used very low electroplating current
density (~ 0.12 mA/cm^2) for the even growth of Ni mesh and polished away the opal
layers with no Ni deposited to reach the surface of Ni mesh layers in order to reduce
the time of etching of Ni mesh by dilute HF acid. Also it is important to remove the
opal completely, otherwise some parts of the macropores in Ni mesh was occupied by
silica spheres, and then blocked the diffusion of electroplating solution. Figure 4.3a
and 4.3b show typical SEM images of a piece of opal (first template) consisting of

a)
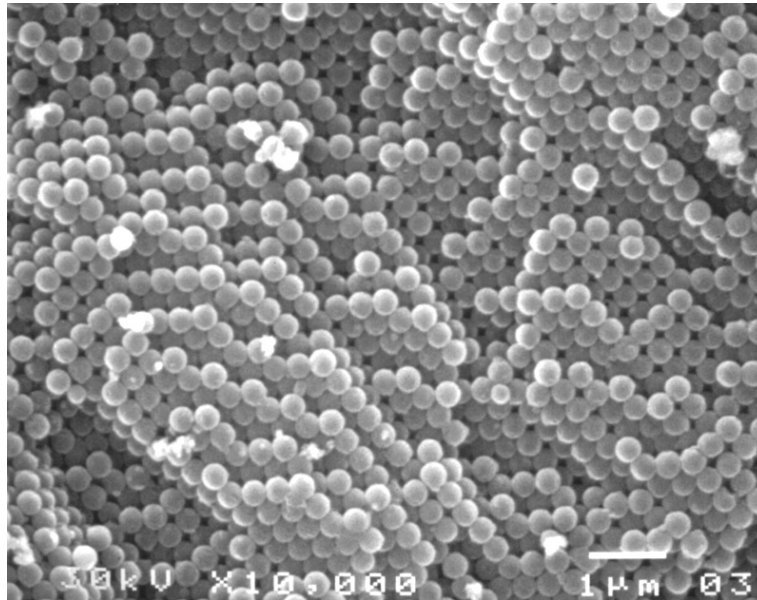
b)
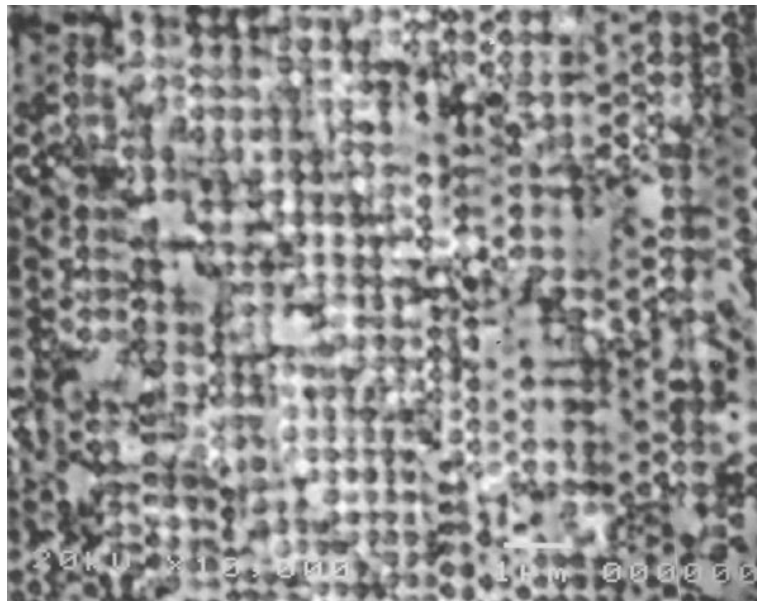
Figure 4.3. SEM pictures of a) a piece of opal consisting of 290 nm diameter silica
spheres ($\times$ 10,000), b) a piece of three-dimensionally periodic NiO mesh
oxidized from Ni mesh containing 290 nm diameter pores ($\times$ 10,000).

290 nm diameter ordered silica spheres and NiO mesh (second-step template)

oxidized from Ni mesh containing 290 nm diameter pores, respectively (both at

magnification of 10,000). Some grey parts on the surface of NiO mesh (Fugure 4.3b)

came from polishing.

Using the NiO mesh as a template, ordered metal sphere arrays were readily

obtained by electrodeposition. Figure 4.4a shows a low magnification ($\times$ 5,000) SEM

image of the of the gold sphere arrays that were electrochemically deposited within

the NiO mesh. EDX analysis reveals the presence of only Au in the sphere arrays after

complete dissolution of the NiO template by hot dilute sulfuric acid. 3D ordered

structure of Au sphere arrays can be seen clearly from Figure 4.4b. Figure 4.5 shows

cross-sectional SEM images of Au sphere arrays. The extended three-dimensional

sphere network can be seen in Figure 4.5a ($\times$ 10,000). The spheres can be seen linked

to each other by narrow interconnects. Cross-sections for SEM studies were prepared

simply by physically separating segments with a small blade, the clumps and large

hollows seen in Figure 4.5a therefore likely result from this process. Figure 4.5b

shows a higher-magnification image of Au sphere arrays in the (111) orientation.

Figure 4.6a shows the SEM image of a small piece of Pd sphere arrays (5,000$\times$). The

flat part on the right lower corner came from the overdeposition of Pd. Well ordered

Pd sphere arrays were exposed after detaching the overdeposited Pd layer. Figure 4.6b

reveals a cross-sectional SEM image of Pd sphere arrays (15,000$\times$). The narrow

interconnects between adjacent Pd spheres can be clearly observed. Interestingly, the

metal spheres are slightly smaller in diameter (ca. 270 nm) relative to those of the

starting opal membrane (290 nm). This likely relates to volume changes that occur on

oxidation of the Ni mesh to NiO. Since the filling fraction of NiO mesh is about 0.44

(refer to Chapter 3), which is larger than that of Ni mesh (0.26), this would

a)
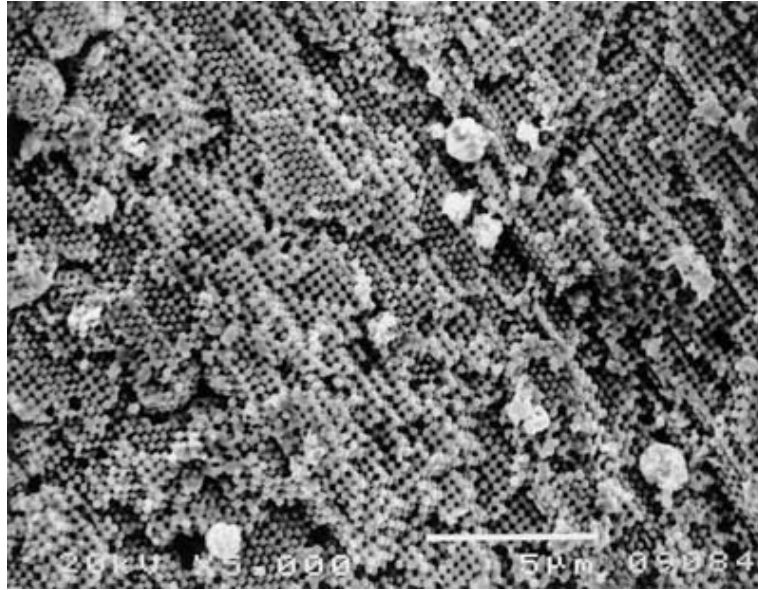
b)
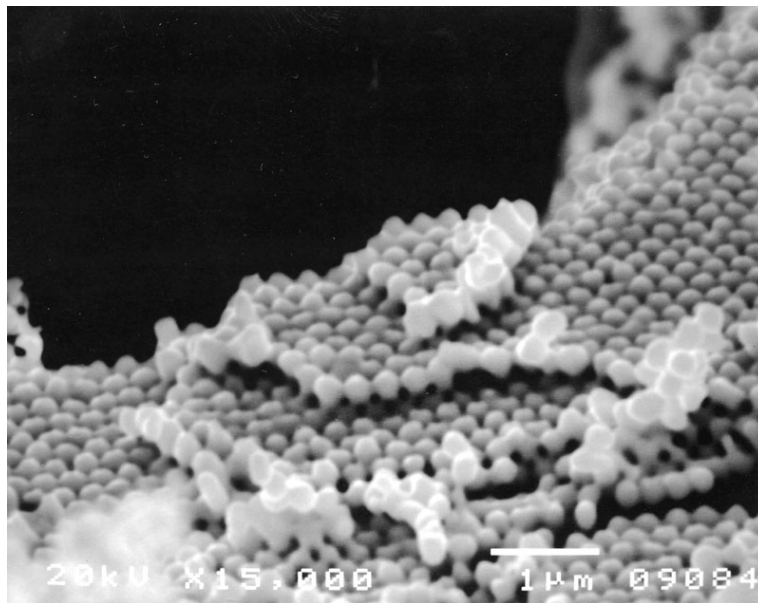
Figure 4.4.   SEM pictures of a) Au sphere arrays at low magnification ($\times$ 5,000),
b) Au sphere arrays show three-dimensional structure ($\times$ 15,000).

a)
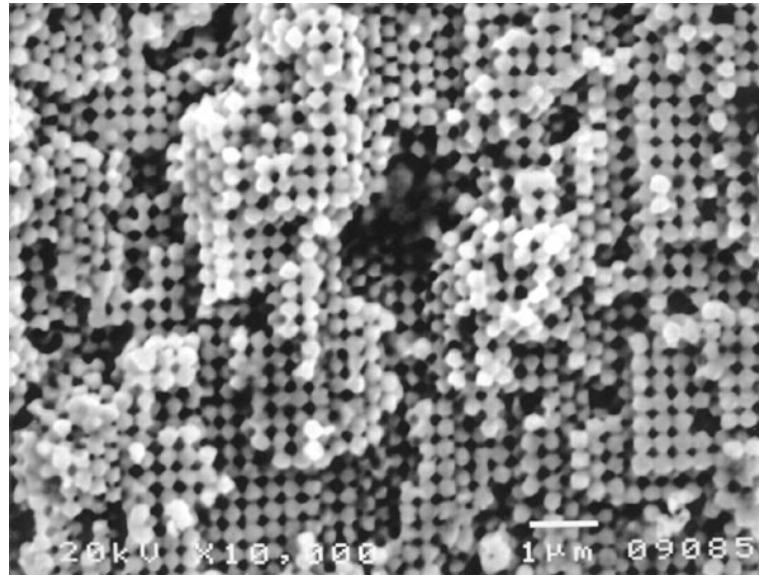
b)
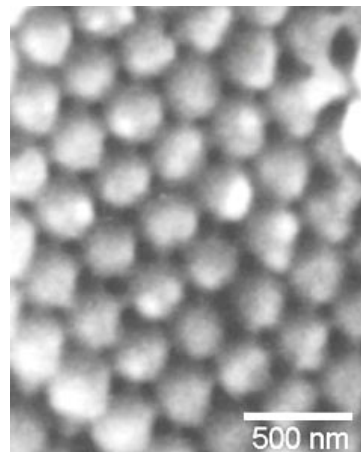
Figure 4.5. Cross-sectional SEM pictures of a) Au sphere arrays at × 10,000 magnification, b) Au sphere arrays along (111) direction.

a)
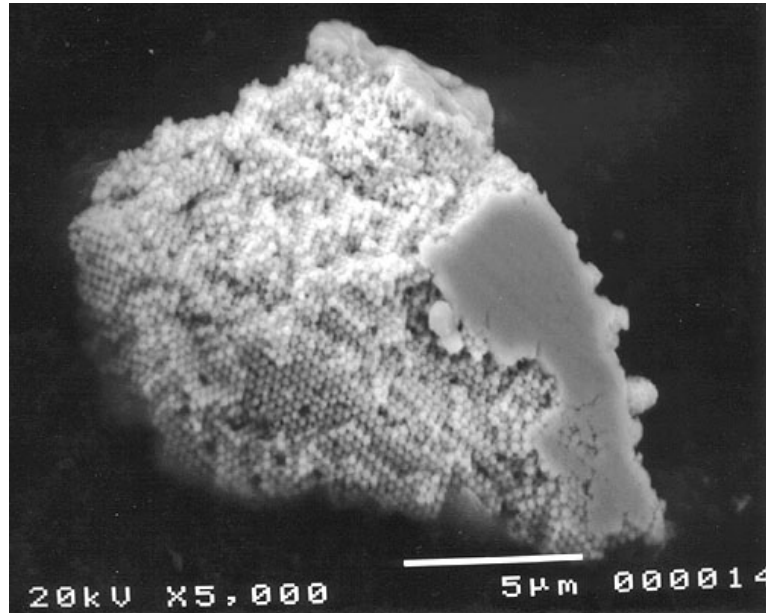
b)
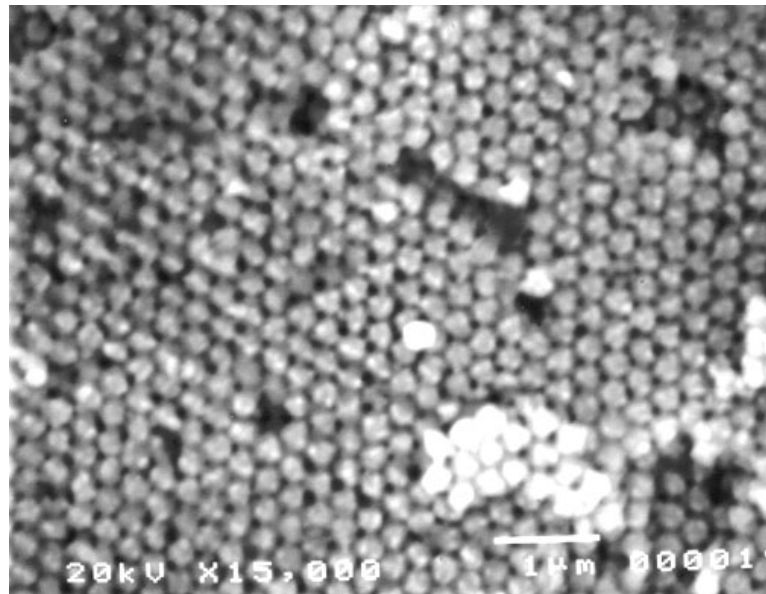
Figure 4.6.   SEM images of (a) nanoscale Pd sphere arrays with overdeposited part
(× 5,000), (b) cross-sectional Pd sphere arrays (×15,000).

correspond to a reduction in the metal sphere diameter from that of the opal spheres to approximately 260 nm, similar to what is observed.

It is important to completely oxidize Ni mesh into NiO mesh. A partial oxidized Ni mesh (NiO shell/Ni core mesh) was attempted to fabricate metal sphere arrays, the resulting sample surface was covered by metal. Though the surface of Ni core was covered by the nanocrystalline NiO shell, the NiO nanoparticles could not completely block the diffusion of plating solution to reach the Ni core, then electrodeposition could also take place on the surface of NiO shell/Ni core mesh, and the inner pores could not completely be filled with metal by electrodeposition. If conductive metal mesh was used as the template for electrodeposition, the electrochemical growth of metal preferentially occurred on the surface of metal mesh, rather than from the bottom electrode. Though metal meshes are not good templates for electrodeposition of metal sphere arrays, they can be used as a mold for the preparation of specific alloys by melt filtration[127] or fabrication of other types of sphere arrays like ceramic sphere arrays by sol-gel methods.

Some other metals like Ni and Co can also be deposited into the NiO mesh, and metal/NiO nanocomposites can thus be produced, but it is hard to separate the metal spheres from NiO mesh since these metals also dissolve in acid. Though freestanding Ni and Co cannot be obtained from NiO mesh template, the Ni/NiO and Co/NiO nanocomposites may have important properties like interesting exchanging bias property since these materials contain antiferromagnetic (NiO)/ferromagnetic (Ni or Co) nanolayers.[145,146,207] Other metal oxide meshes (such as CoO and CuO meshes) can also be prepared and used as the templates to fabricate a diversity of functional metal sphere arrays and metal/metal oxide nanocomposites by electrodeposition.

4.3.3 Metal Sphere Arrays from PMMA Mesh Templates

4.3.3.1 Scanning Electron Microscopy Characterization

Though electrodeposition is a highly effective approach for the preparation of

metal sphere arrays by template filling, the application of the NiO mesh is limited,

since it readily dissolves in solutions containing acid and can be affected by strongly

coordinating ligands. Polymer meshes have an advantage that they can be unaffected

by acidic or basic solutions, so that a wider range of metals may be electrodeposited.

Further, the ease at which organic reagents can remove the polymer meshes readily

leads to high-quality, freestanding metal sphere arrays.

Figure 4.7 reveals the uniform porous structure of the PMMA mesh, which

contains 290 nm diameter pores ($\times$ 20,000). Since the macropores in PMMA mesh are

interconnected, the PMMA mesh allows the electroplating solutions to diffuse

through the mesh and reach the Au electrode, so that electrochemical growth of the

metal spheres can take place, starting from the Au electrode. Because of the

hydrophobicity of the PMMA surface, the PMMA mesh had to be kept wet after

removal of the silica opal spheres by HF solution, otherwise the aqueous plating

solutions could not effectively diffuse into the mesh. Also, the wet PMMA mesh

maintains its porous structure, with pore diameter similar to that of the original silica

spheres. If dried in air, the PMMA mesh shrinks and the pore diameter somewhat

decreases.

Figure 4.8 shows a cross-sectional view of Pd spheres between the Au

electrode and the sample surface ($\times$ 1,500). The filling is quite complete, and the

periodicity extends over the entire area, except when interrupted by defects present

largely as stacking faults in the original opal. Figure 4.9 shows SEM pictures of

metal sphere arrays at different magnification. High-quality metal sphere arrays with
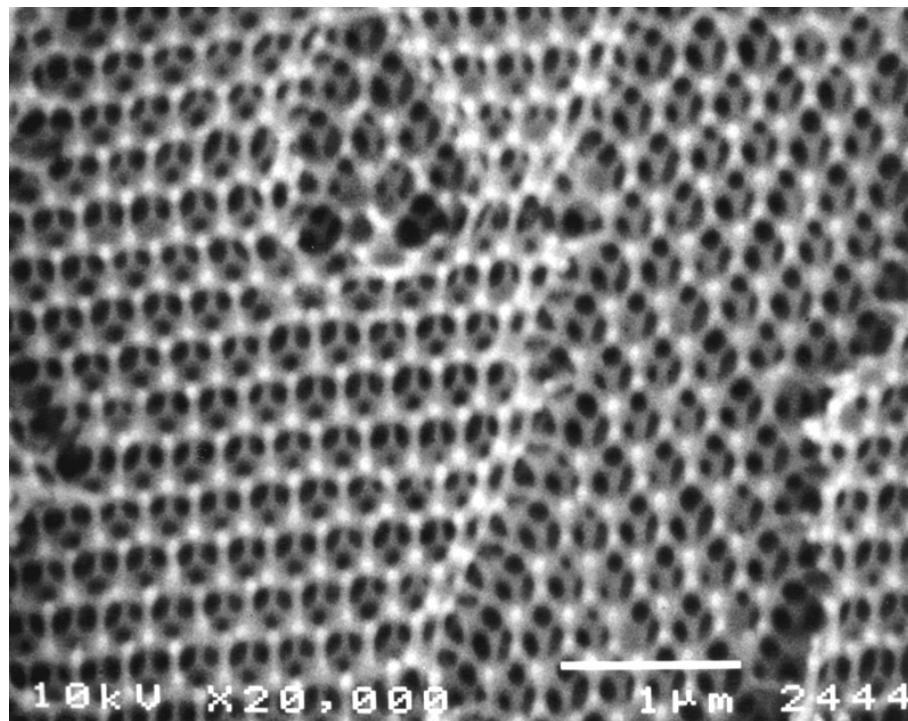
Figure 4.7.   SEM image of a piece of PMMA mesh containing 290 nm diameter
pores (× 20,000).
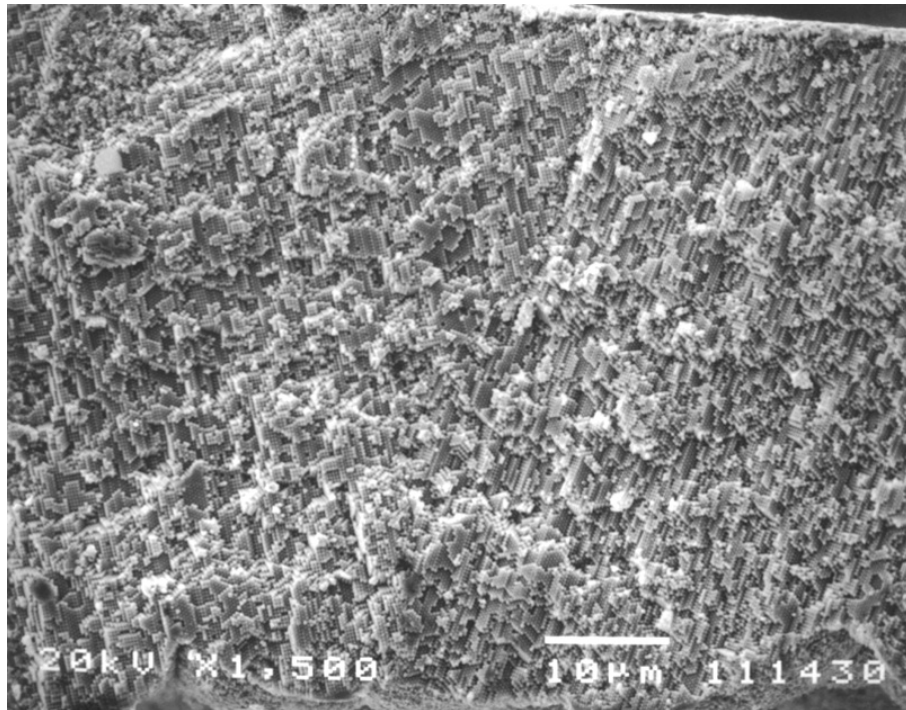
Figure 4.8.   Cross-sectional SEM image of 290 nm diameter Pd spheres between the Au electrode and the sample surface ($\times$ 1,500).

Figure 4.9. SEM images of 290 nm diameter metal sphere arrays at different magnifications. a) Ni sphere arrays ($\times$ 10,000), b) Pd sphere arrays ($\times$ 20,000), c) Ni sphere arrays with (111) orientation ($\times$ 35,000), d) Ni sphere arrays with predominately (100) orientation ($\times$ 50,000), e) Pd sphere arrays at high magnification ($\times$ 100,000).

a)

b)

c)

d)

e)

20kV X100,000 0.1μm 1114
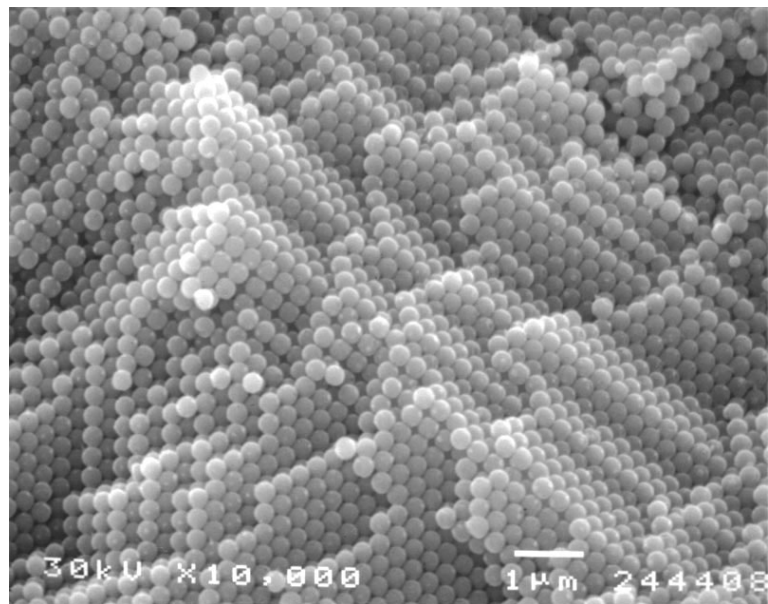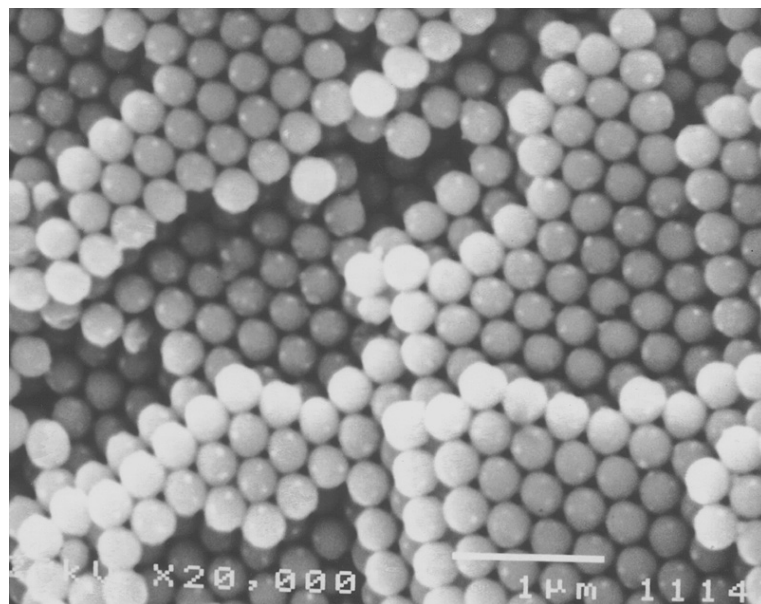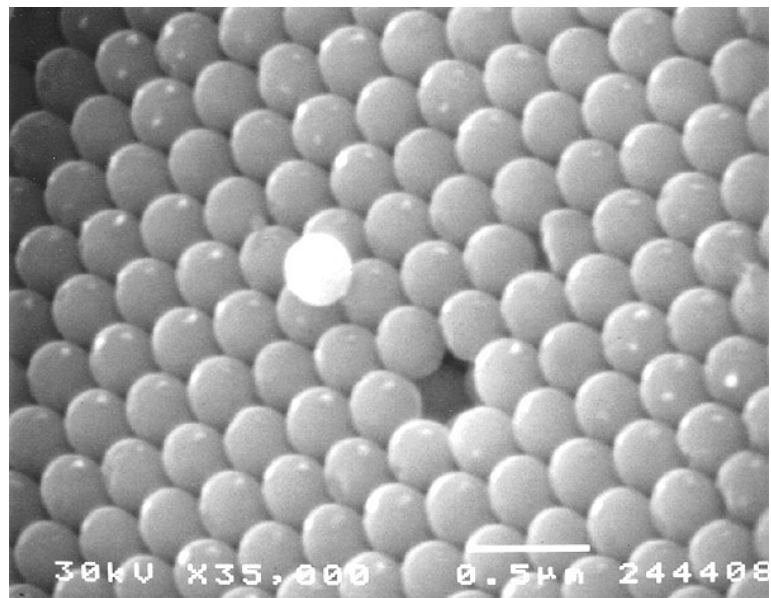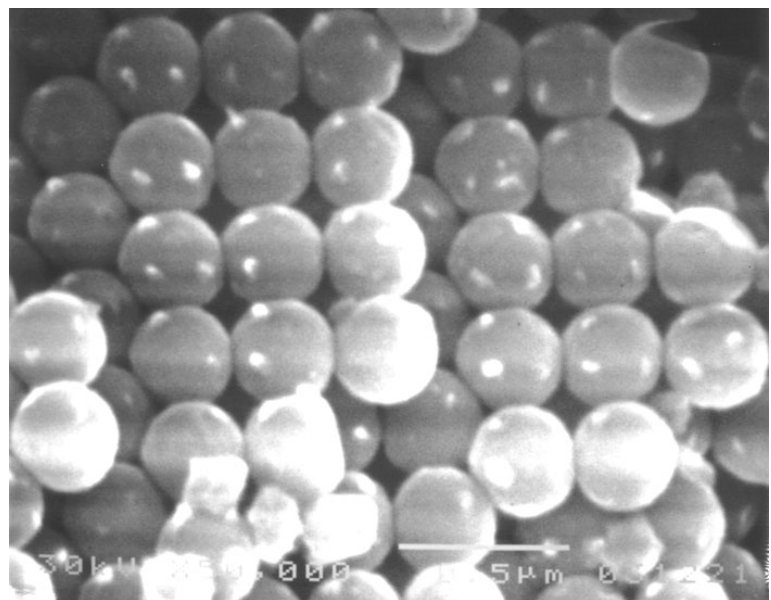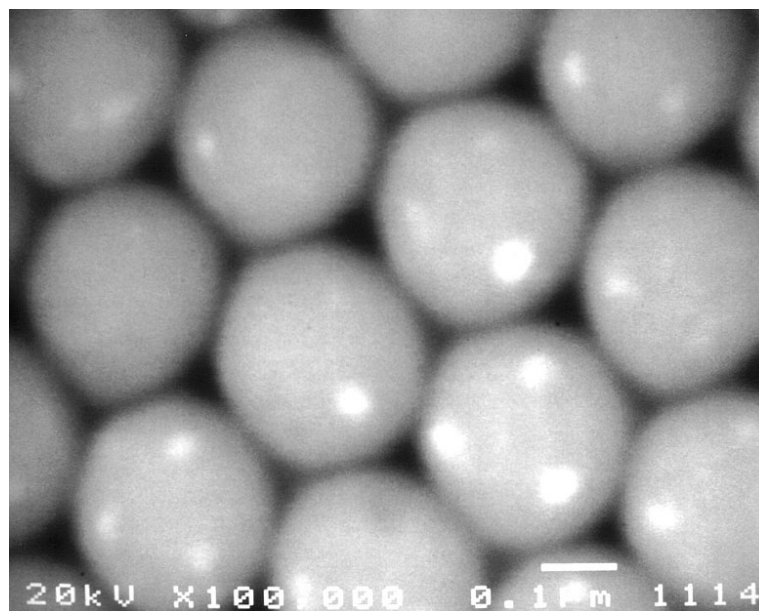
three-dimensional periodicity can be seen from Figure 4.9a (Ni sphere arrays, at magnification of × 10,000). Figure 4.9b shows the Pd sphere arrays at magnification of × 20,000. Figure 4.9c and 4.9d show predominately (111) and (100) orientation of Ni sphere arrays, with magnification of (× 35,000) and (× 50,000), respectively. Interestingly, one single Ni sphere was found on the surface of the (111) plane (Figure 4.9c), and also a void space was left on the lattice, which suggests that metal sphere arrays may be broken into isolated spheres by methods such as ultrasonication.[192,208] Figure 4.9e is a higher magnification (× 100,000) of Pd sphere arrays. The location of broken nanoscale interconnects (to spheres removed from the sample) can be clearly seen in the Figure 4.9b to 4.9e, as white spots on the sphere surfaces. Based on Figure 4.9d and 4.9e, the diameter of as-prepared metal spheres is estimated to be 290 ± 10 nm, very close to that of original silica spheres, indicating that electrodeposition produces high-density infiltration through volume templating. On the contrary, a sol-gel process either forms hollow colloidal crystals through surface templating or experiences significant reduction of sphere diameter.[85,192] Opal with 180 nm diameter silica spheres was also used to fabricate metallic colloidal crystals, and similar results were obtained (Figure 4.10, × 15,000).

4.3.3.2 Optical Image of Metal Sphere Arrays

Since these metal sphere arrays have structures with three-dimensional periodicity on a length scale comparable to that of light, they are metallic photonic crystals. These materials strongly diffract white light and exhibit iridescent colors. Figure 4.11 shows the optical photo of 290 nm diameter Ni sphere arrays. Different colors on the surface relate to different regions of metal sphere arrays, each of which is differently oriented. Also, based on Bragg's Law, the color for same orientation region depends on the angle of the incidence on the sample.
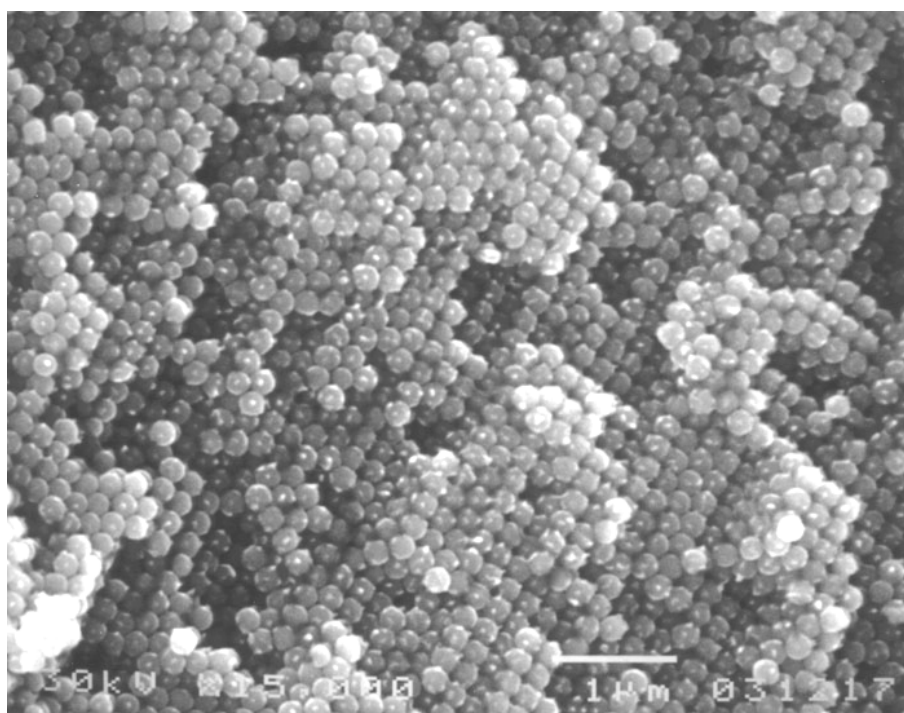
Figure 4.10. SEM image of 180 nm diameter Ni sphere arrays (× 15,000).
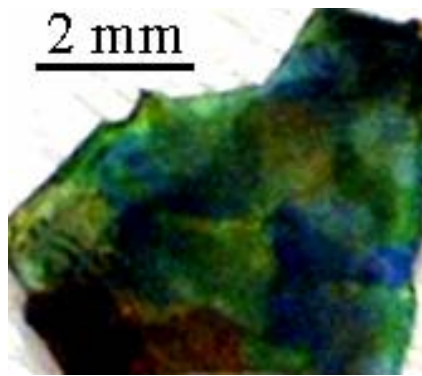
Figure 4.11. Optical image of 290 nm diameter Ni sphere arrays.

4.3.3.3 X-Ray Diffraction of Metal Sphere Arrays

The electrodeposition produced polycrystalline metal sphere arrays, like that observed in electrodeposited metal nanowires and metal meshes. Figure 4.12 shows the powder X-ray diffraction pattern of a piece of Ni sphere arrays. The position and relative intensity of peaks agree well with that reported for polycrystalline FCC (face-centered cubic) nickel (PDF-2 database, International Center for Diffraction Data, Newtown Square, Pennsylvania, 1993; Ni reference pattern, 4-850), indicating an absence of preferred orientation in the electrodeposited nickel sphere arrays.

4.3.3.4 Magnetic Properties of Metal Sphere Arrays

Magnetic hysteresis loops with different angles up to a field of $\pm$ 10,000 Oe for 290 nm Ni sphere arrays prepared from a PMMA mesh template were performed on a vibrating sample magnetometer (VSM) at room temperature. Figure 4.13 shows both the hysteresis loops with the field perpendicular (out-of-plane) and parallel (in-plane) to the plate plane for the nickel sphere opal. Typical values of coercivity H_c and squareness SQ (ratio of remanence to saturation magnetization, M_r/M_s) are H_c = 100 Oe and SQ = 0.028 for out-of-plane magnetization and H_c = 90 Oe and SQ = 0.225 for in-plane magnetization. These values of coercivity are similar to that of an array of 300 nm diameter Ni nanowires[209] and higher than for bulk Ni, which has coercivity of a few tens of oersteds.[177] The large difference in the remanence shows that the easy direction of magnetization is in the plate plane, and perpendicular to the sample membrane is the magnetic hard axis. In addition, the very low remanent magnetization, M_r, is always less than 30% of the saturation magnetization, which indicates very strong interaction among the Ni sphere arrays because the spheres are very close to each other.
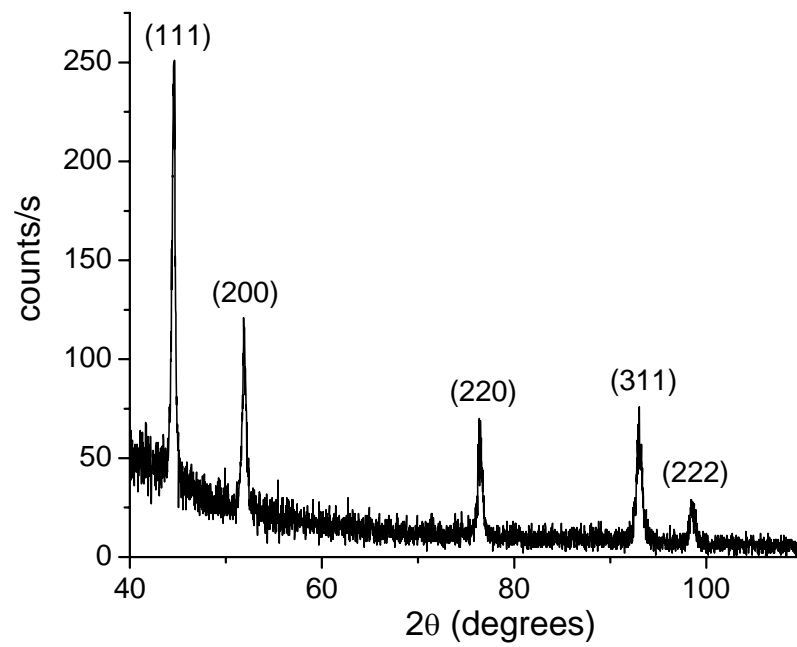
Figure 4.12. X-ray diffraction pattern of 290 nm diameter Ni sphere arrays.

a)

b)
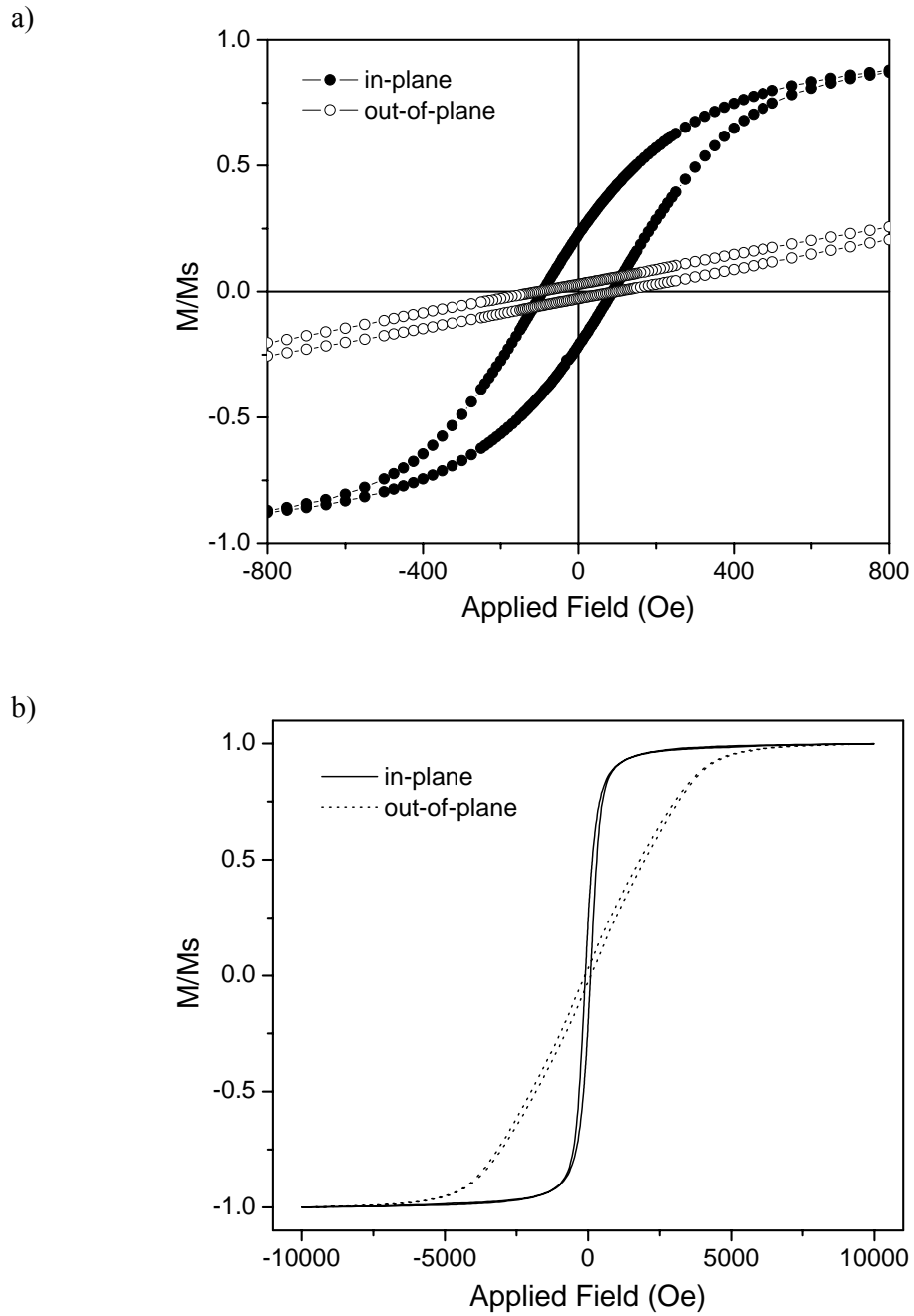
Figure 4.13. a) Hysteresis loops of ordered Ni sphere arrays with the applied field
perpendicular (out-of-plane) and parallel (in-plane) to the plate plane.
b) Full range of the out-of-plane and in-plane hysteresis loops (measured
over a field range of between -10000 to 10000 Oe) for Ni sphere arrays.

Figure 4.14a and 4.14b present the angular dependence of coercivity and squareness, respectively. The indicated parameter θ is the angle between the applied magnetic field and the normal to the plate. The "M" shape angular variation of coercivity has also been found in other anisotropic magnetic systems, such as in CoNi thin films[210-213] and Ni nanowires.[214,215] Domain wall motion[216] and coherent rotation[217] may account for the mechanism of magnetization reversal.[213] For the angle range of 0° to 90°, the coercivity increases rapidly with angle to reach a maximum (154 Oe) at $\theta = 20°$. After that the coercivity decreases with increasing θ and the minimum (91 Oe) occurs when the applied field is parallel to the plate plane ($\theta = 90°$). According to coherent rotation mode,[217] the coercivity increases with θ, which is consistent with the angular variation of coercivity at $\theta < 20°$. After a critical angle ($\theta = 20°$), domain wall motion will dominate the reversal process. Based on domain wall motion mode, the angular variation of coercivity normalized at $\phi = 0°$ will be $1/|\cos\phi|$ (ϕ is the angle between the easy axis and applied field; in this system, the easy axis lies in the plate plane, thus $\phi = 90°- \theta$ and $\cos\phi = \sin\theta$).[216] As can be seen from Figure 4.15, the experimental data of normalized coercivity at higher angles agree well with the $1/\sin\theta$ values predicted by domain wall motion mechanism. The angular dependence of as-prepared Ni sphere arrays ($\sim 60 \mu m$ thick) is different from that of thin-film macroporous permalloy (1 μm pore size and 0.5 μm thickness), in which domain wall motion predominates and the product of coercivity and the angle between applied magnetic field and the normal to the film plane is nearly constant.[144] The squareness behavior of Ni sphere arrays shows a $|\cos\phi|$ dependence, i.e. SQ = $SQ_0|\cos\phi|$, where SQ_0 is the squareness when the applied field is along the easy axis. The $|\cos\phi|$ dependence is caused by the uniaxial anisotropy along the in-plane easy

a)

b)
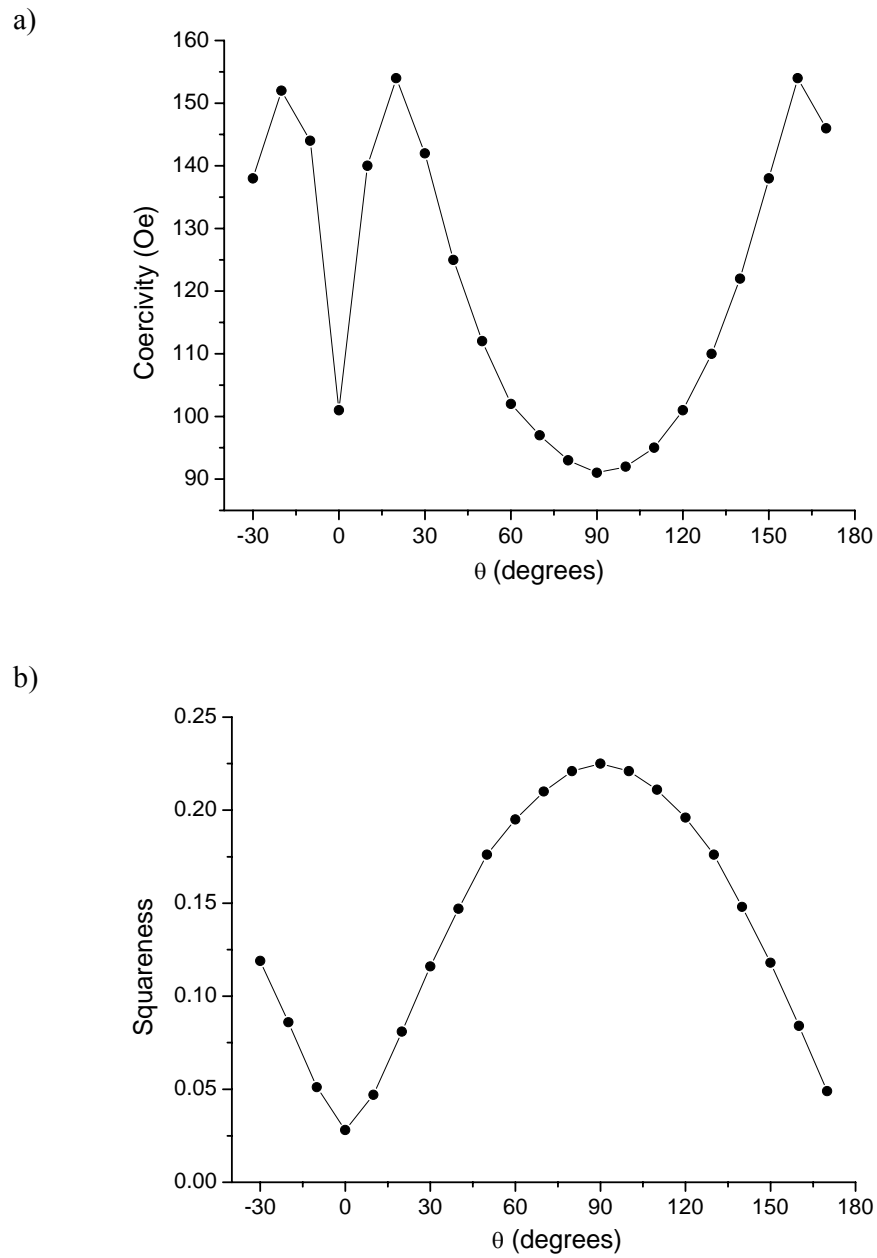
Figure 4.14. Angular dependence of a) coercivity and b) squareness for Ni sphere arrays. θ is the angle between the applied magnetic field and the normal to the plate plane of the Ni sphere arrays.
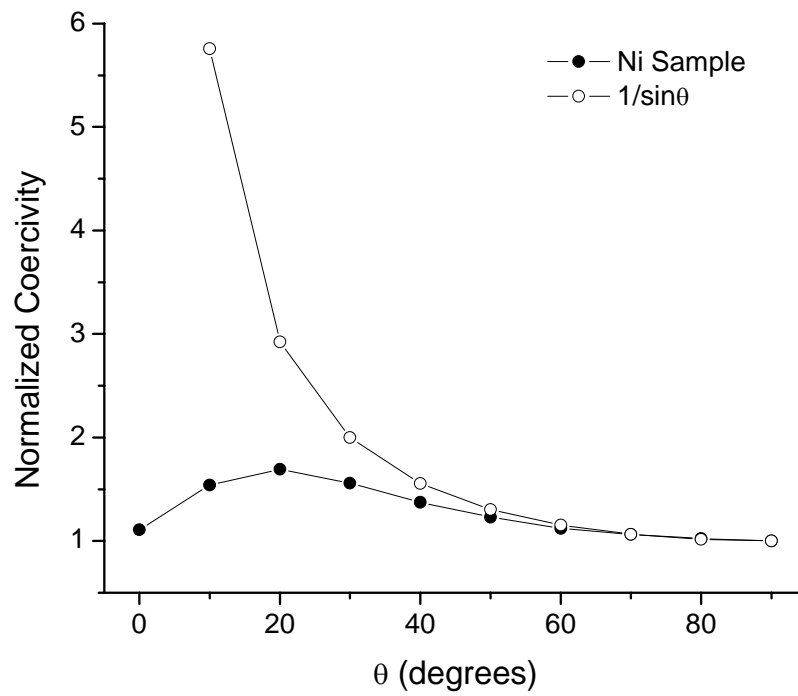
Figure 4.15. Normalized coercivity as a function of angle for Ni sphere arrays.

axis of magnetization.[214] Similar feature of angular dependence of squareness was also reported for Ni and Co nanowires.[214,215,218] The maximum of squareness (0.225) is obtained when the magnetic field is applied parallel to the plate plane ($\theta = 90°$) and minimum squareness (0.028) occurs when the field is perpendicular to the plate plane ($\theta = 0°$). When rotating the magnetic field in the plate plane, similar hysteresis loops were obtained from different orientations. Figure 4.16 shows the in-plane hysteresis loops with different orientations (0° to 200°, at 10° interval). The coercivity and squareness are in the range of 92 to 94 Oe, and 0.232 to 0.255, respectively. The very similar hysteresis loops indicate random in-plane magnetization anisotropy in this system, as is similar to the thin-film CoNiCr/Cr media.[219] Due to the polycrystalline structure of Ni sphere arrays and the relatively small crystalline anisotropy, the crystalline anisotropy of Ni can be neglected. Therefore, the angle dependent magnetic behavior is overall predominated by shape anisotropy of the bulk nickel piece.

The angular dependence of hysteresis loops for cobalt sphere arrays prepared from a PMMA mesh template was also investigated. Figure 4.17 shows both the hysteresis loops with the field perpendicular (out-of-plane) and parallel (in-plane) to the plate plane for the Co sphere arrays. The material exhibits a coercivity of 88 Oe and squareness of 0.099 for in-plane hysteresis loop, and a coercivity of 108 Oe and squareness of 0.033 for out-of-plane hysteresis loop. The easy axis of magnetization lies in the plate plane. Interestingly, the out-of-plane hysteresis loop shows an anomalous 'hourglass shape', i.e. the loop looks as if it is pinched closed at near zero fields, the region where an ordinary hysteresis graph is the widest. Such an hourglass-shaped hysteresis loop was also observed in the macroporous Co (due to the exposition in the air, an antiferromagnetic CoO layer was present on the surface of the
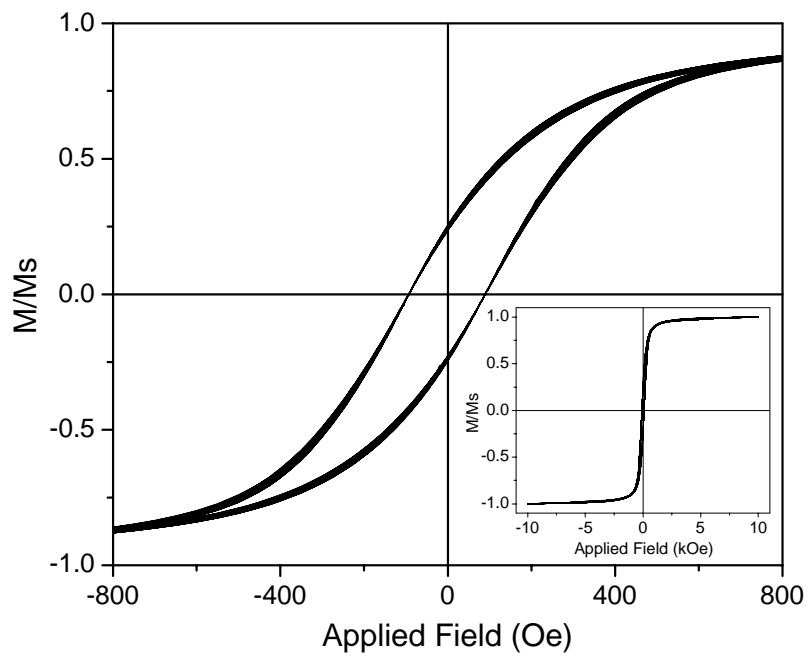
Figure 4.16. In-plane hysteresis loops from different orientations for ordered Ni
sphere arrays. The inset is the full range of the hysteresis, measured over
a field range of between -10,000 to 10,000 Oe.

a)

b)
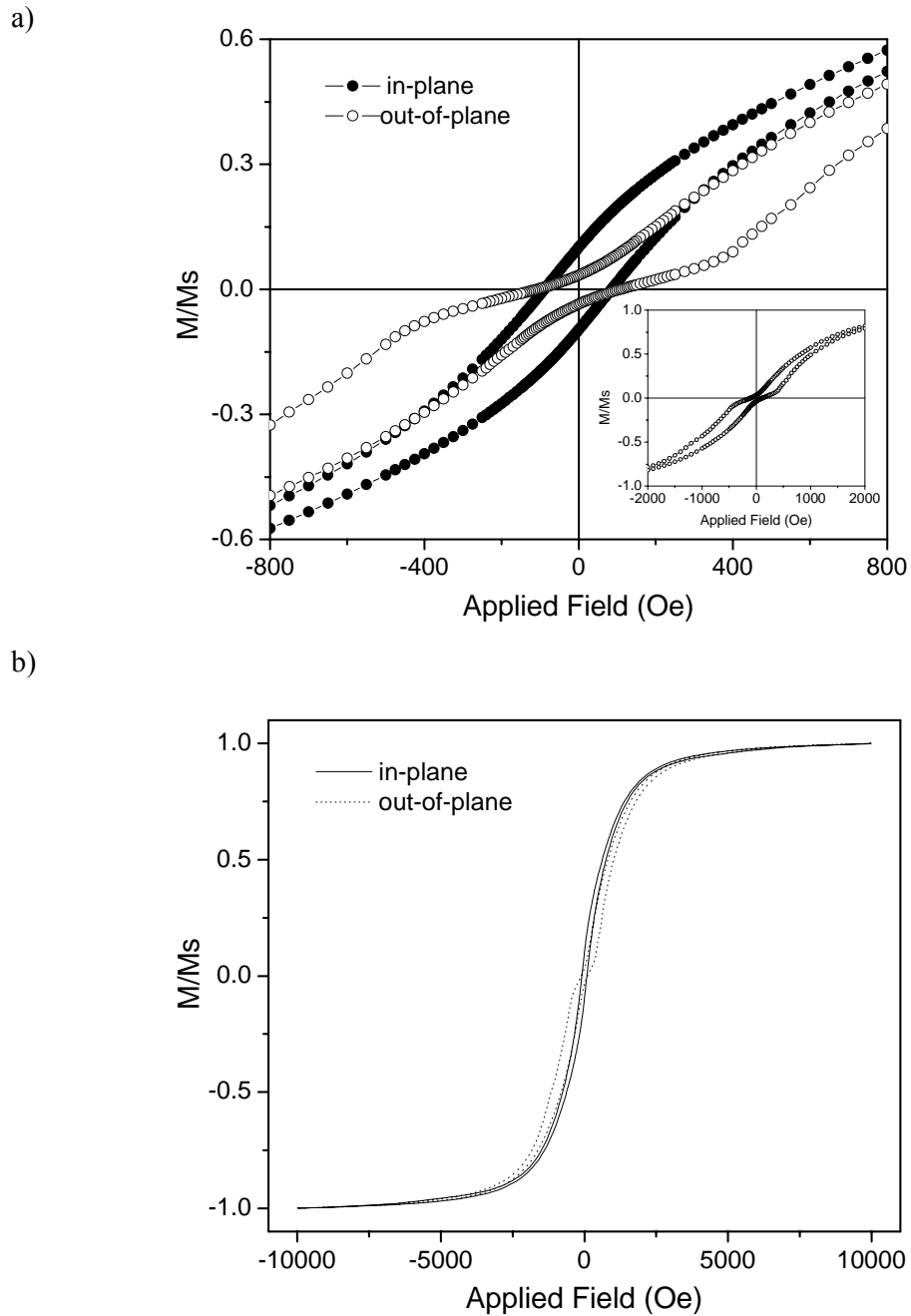
Figure 4.17. a) Hysteresis loops of ordered Co sphere arrays with the applied field
perpendicular (out-of-plane) and parallel (in-plane) to the plate plane.
The inset is out-of-plane hysteresis loop showing hourglass shape,
between field range of -2,000 to 2,000 Oe.   b) Full range of the out-of-
plane and in-plane hysteresis loops (measured over a field range of
between -10000 to 10000 Oe) for Co sphere arrays.

Co nanoparticles in macroporous Co), where the anomaly in the hysteresis loops was attributed to the formation of spin-glass-like state in the coupled single-domain Co nanoparticles.[146] The angular dependence of coercivity and squareness of Co sphere arrays is present in Figure 4.18. The shape of graphs is similar to but not so regular as that in Ni sphere arrays, especially when the field is nearly perpendicular to the plate plane. The coercivity data are in the range of 87-118 Oe with the maximum (118 Oe) at $\theta = 20°$ and minimum at $\theta = 90°$ (87 Oe); and the squareness shows $|\sin\theta|$ i.e. $|\cos\phi|$ dependence with squareness range of 0.031 to 0.099. Like that observed in Ni sphere arrays, very similar in-plane hysteresis loops from different orientations (Figure 4.19) also occur in the ordered Co sphere arrays, indicating that there is no obvious in-plane magnetization anisotropy in this system. The coercivity and squareness are in the range of 87 to 90 Oe, and 0.088 to 0.112, respectively.

The temperature dependence of hysteresis loops for 290 nm Ni sphere arrays was investigated using a SQUID magnetometer. Figure 4.20 shows the out-of-plane hysteresis loops of 290 nm Ni sphere arrays measured at 5, 50, and 300 K. The material exhibits a coercive field (H_c) of 220 Oe and squareness of 0.066 at 5 K. Both the coercivity and SQ decrease slowly with increasing temperature. The material reached a coercivity of 122 Oe and M_r/M_s of 0.038 at 300 K (by the comparison with the coercivity and squareness data obtained from VSM, the sample in SQUID was not strictly perpendicular to the field, but with an inclination of about 5°, see Figure 4.14). It seems that the coercivity and squareness of Ni sphere arrays vary linearly with temperature (Figure 4.21). Linear temperature dependence of the coercivity was also observed in Ni nanowires,[180] acicular Fe_2O_3,[220] and percolating granular Fe–SiO_2 composites.[221]

a)

b)
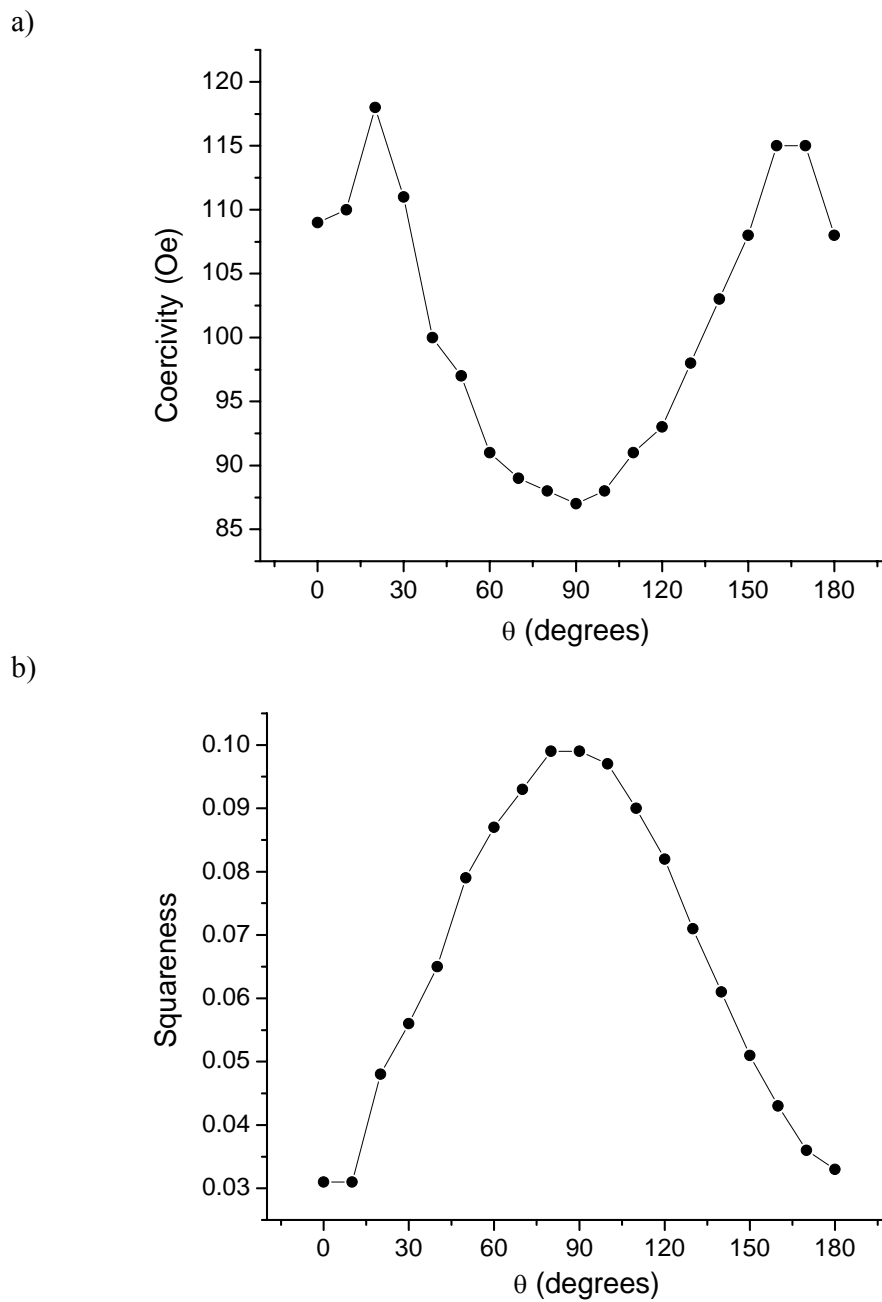
Figure 4.18. Angular dependence of a) coercivity and b) squareness for Co sphere
arrays. θ is the angle between the applied magnetic field and the normal
to the plate plane of the Ni sphere arrays.
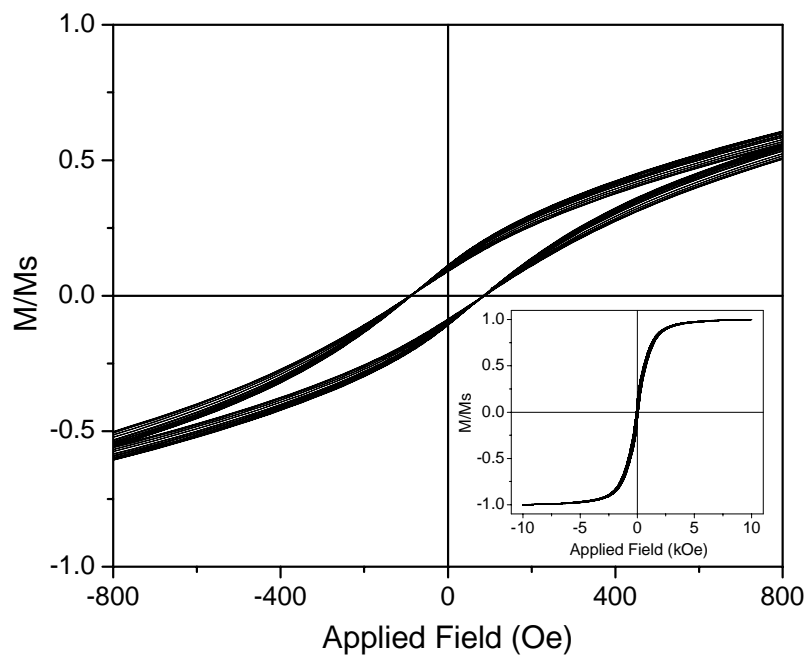
Figure 4.19. In-plane hysteresis loops from different orientations for ordered Co
          sphere arrays. The inset is the full range of the hysteresis, measured over
          a field range of between -10,000 to 10,000 Oe.

a)

b)
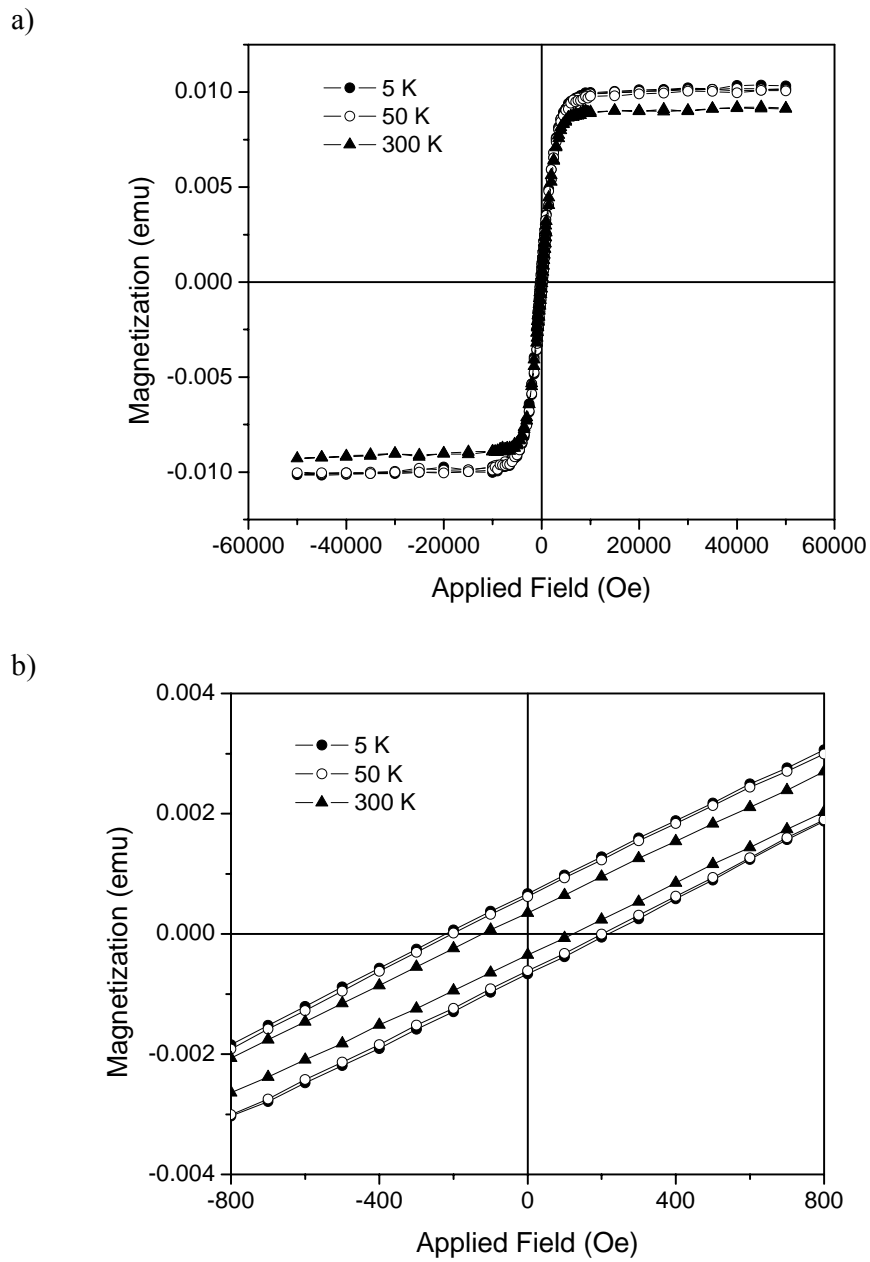
Figure 4.20. a) Out-of-plane hysteresis loops for 290 nm Ni sphere arrays at 5, 50, and 300 K. b) Magnification of the hysteresis loops in field range of between -800 to 800 Oe.

a)

b)
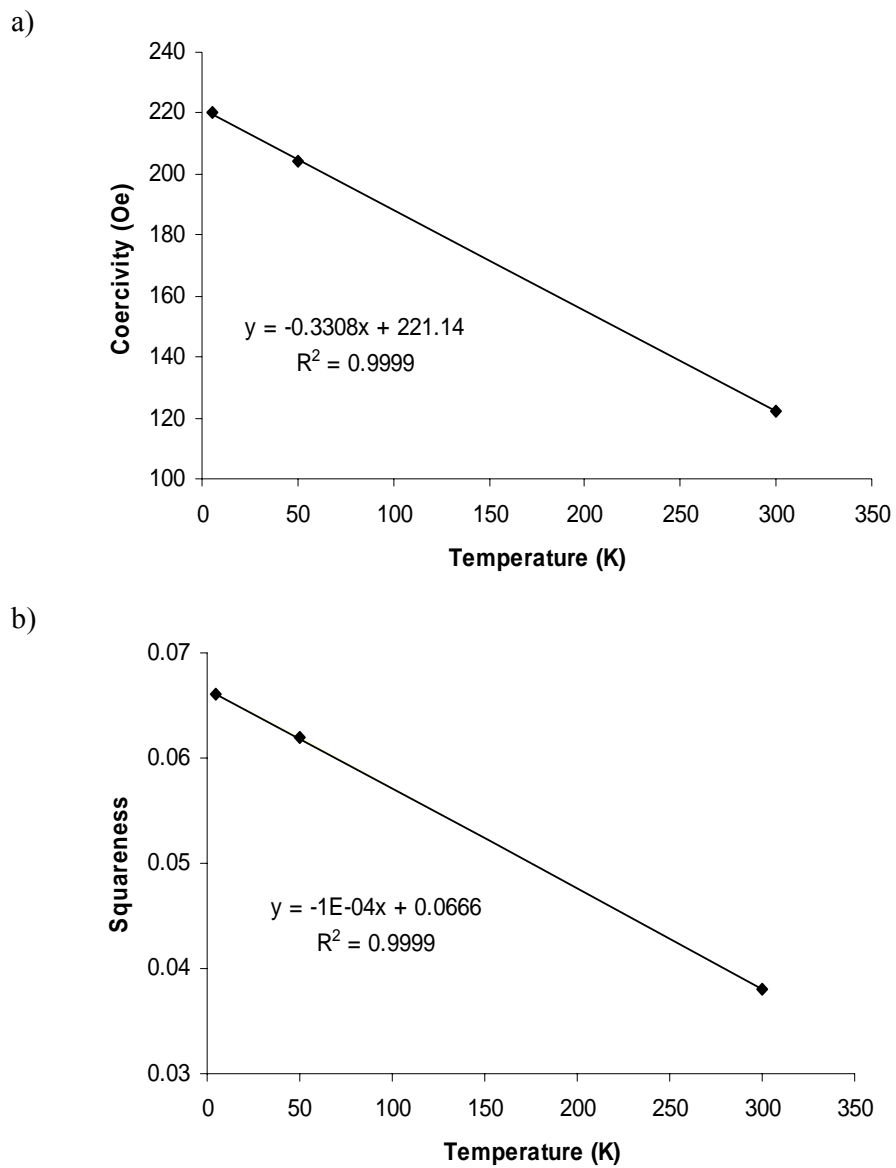
Figure 4.21. Temperature dependence of a) coercivity and b) squareness for Ni sphere arrays.

4.3.3.5 Fragmentation of Metal Sphere Arrays by Ultrasonication

Ultrasonication has been used to disintegrate the colloidal crystals into small arrays of spheres, and even single spheres.[192,208] Due to the strong interconnection between adjacent metal spheres, it is more difficult to fragment the metallic colloidal crystals (metal sphere arrays) than to fragment ceramic colloidal crystals. After 2-hour sonication in a 75 W ultrasonic bath, the metallic colloidal crystal was broken into about 1 mm size pieces of colloidal crystals. Some smaller pieces, several microns in size, (showed in Figure 4.22a) were detached from the larger pieces and dispersed in water. Continued ultrasonication of the smaller pieces resulted in even smaller sphere arrays, and isolated spheres. Figure 4.22b shows several isolated spheres and the inset is a segment consisting of six spheres. The six spheres are still connected to each other through the small interconnects, which can be clearly seen in the inset of Figure 4.22b.

4.3.4 Oblate Metal Sphere Arrays from Compressed PMMA Mesh Templates

PMMA mesh is a soft material, which can change shape to form a PMMA mesh with oblate pores by stretching or pressing. PMMA mesh with oblate pores can be further used as a template for the fabrication of oblate sphere arrays. Jiang *et al.* used stretched PMMA mesh to fabricate hollow oblate TiO_2 spheres by sol-gel technique.[192] In our experiments, we used a laboratory press to make compressed PMMA mesh (more details are described in Chapter 3) and then fabricated oblate metal sphere arrays by electrodeposition.

Figure 4.23 shows a typical oblate Ni sphere arrays ($\times$ 10,000), and the inset is a higher magnification of oblate Ni sphere arrays in (111) orientation. Three-dimensionally ordered oblate Ni spheres can be seen clearly on the picture. Due to the pressing, the volume of the oblate pores is smaller than that of the spherical pores in

a)

b)
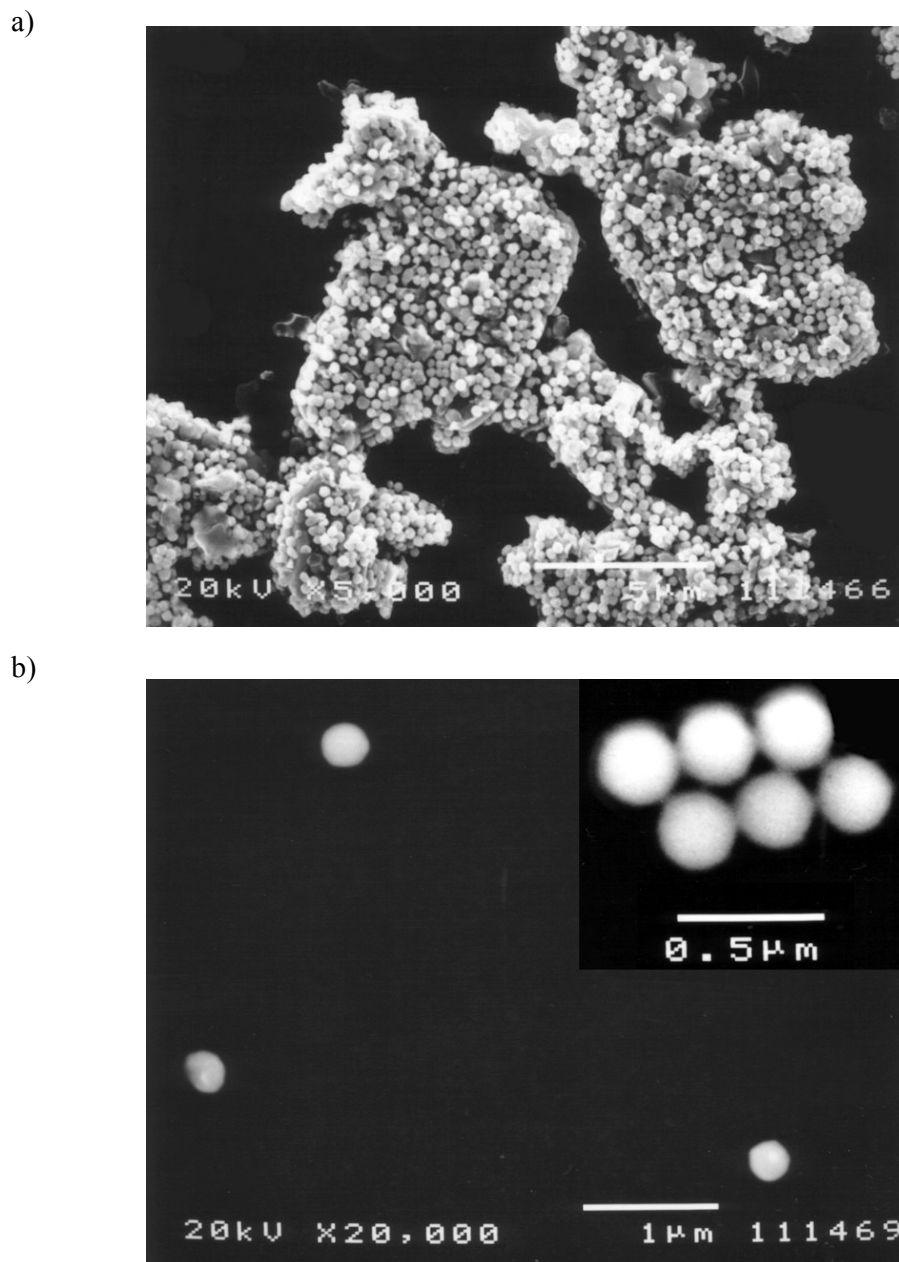
Figure 4.22. SEM images of (a) small pieces of ordered Pd spheres after 2-hour ultrasonication ($\times$ 5,000), (b) isolated Pd spheres after longer ultrasonication ($\times$ 20,000), inset shows an array of six spheres at higher magnification ($\times$ 35,000).
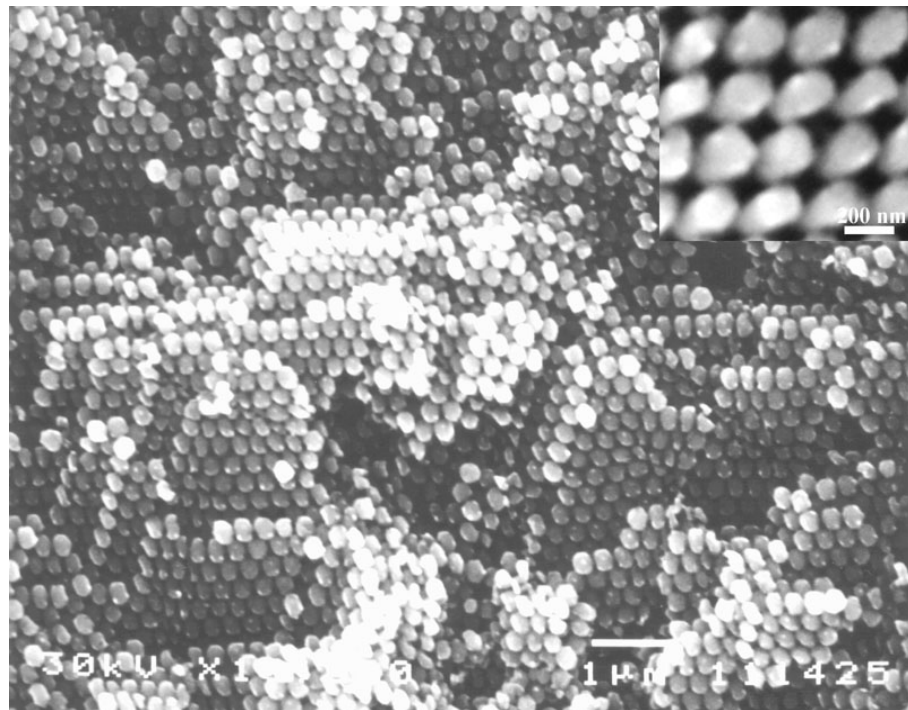
Figure 4.23. SEM oblate Ni sphere arrays fabricated from compressed PMMA mesh, inset shows higher magnification image of oblate Ni sphere arrays.

original PMMA mesh, and then the volume of the oblate metal spheres is smaller than that of relating metal spheres. Also, ultrasonication can be used to break the oblate metal sphere arrays into smaller pieces and even monodisperse oblate metal spheres.[192]

4.2 Conclusions

The two-step templating method, combining chemical and electrochemical processes, provides an effective route for the preparation of metal sphere arrays. These metal sphere arrays are composed of highly ordered metal spheres having a diameter close to that of the SiO_2 spheres in the starting opal templates. Angle-dependent magnetic properties of Ni and Co sphere array membranes exhibit out-of-plane anisotropy. Investigations of these metal sphere arrays are of significant fundamental and technological interest due to their novel structures having three-dimensional periodicity. For example, theoretical calculations show that the metal sphere arrays are promising for the construction of complete photonic band gap materials in the visible part of the optical spectrum.[222-225] In addition, oblate sphere arrays can be fabricated using compressed PMMA template by electrodeposition, and small pieces of metal sphere arrays and isolated metal spheres, which are hard to otherwise fabricate, can be obtained by ultrasonication technique. Furthermore, the method described here can be conveniently extended to fabricate semiconductor (such as CdS, CdSe, and ZnO) nanosphere arrays and conductive polymer/nonconductive polymer nanocomposites.

CHAPTER 5

SUMMARY

Three-dimensionally (3D) ordered meshes were fabricated by a colloidal crystal templating method. In this process, opals composed of 3D close-packed SiO_2 spheres served as templates, with the voids between the SiO_2 spheres infiltrated by materials (such as metals and polymers) that solidified in place without disrupting the order of opals. Subsequent dissolution of the opals by HF solution opened 3D mesh structures.

Using opals as templates, well-defined metal (such as Ni, Pd, and Au) meshes were readily obtained by electrochemical deposition using constant current method. Electrodeposition ensures a high-density filling of the void spaces in opals, resulting in very low shrinkage of metal meshes when the opal templates are removed. Also, the extent of metal growth can be controlled by adjusting the charge passed in the deposition. The plating current density plays an important role in the electrodeposition of metal meshes. In general, lower current density led to more uniform deposition. Also, higher-quality metal meshes were obtained if opals consisting of larger diameter SiO_2 spheres were used, because of the faster diffusion of metal ions inside larger diameter opals.

Some metal oxide meshes like NiO mesh could be prepared by direct oxidation of corresponding metal meshes in the air. Due to the lower density and higher formula weight of metal oxides comparing with related metals, the metal oxide

meshes exhibit higher volume occupation fraction than corresponding metal meshes. For example, the filling factor of NiO meshes is about 0.44 while it is only 0.26 for Ni meshes. Also the nanocrystalline sizes of metal oxide particles could be adjusted by temperature. More mechanically stable metal oxide meshes comprising of larger metal oxide nanocrystals could be obtained by annealing metal meshes at higher temperature. This direct conversion of metal meshes may be extended to fabricate other types of meshes, such as metal halide meshes and metal sulfide meshes.

3D periodic conducive polyaniline meshes were prepared by electrochemical polymerization of aniline monomer inside opal templates in acidic solution. Nonconductive poly(methyl methacrylate) (PMMA) meshes were synthesized by chemical polymerization of methyl methacrylate (MMA) monomer using opal templates. These polymer meshes exhibit highly uniform porous structures consisting of glassy polymer walls. Due to the mechanical flexibility of polymer meshes, the PMMA meshes could be pressed to produce deformed PMMA meshes having oblate pores.

One of the important applications of the meshes is that they can be used as further templates to fabricate new types of colloidal crystals (nanosphere arrays) and specific nanocomposites. Metal sphere arrays were prepared by electrodepositing metals into the voids of poorly conductive NiO mesh or PMMA mesh templates and then removed the templates by acids (for NiO) or organic solvents (for PMMA). Metal/NiO or Metal/PMMA composites could also be obtained if the templates were left intact.

Magnetic measurements showed that both the metal (such as Ni and Co) meshes and sphere arrays had enhanced coercivities compared with bulk metals, due to the size effect of the nanometer dimensions of the components in meshes and

sphere arrays. Both the coercivity and squareness decreased with increasing temperature. Angular variation of Ni and Co sphere array membranes exhibited out-of-plane magnetic anisotropy, similar to that observed in magnetic recording media (such as CoNi and CoNiCr/Cr films) membranes.

Due to their unique structures having 3D periodicity, these meshes and sphere arrays have potential applications in a variety of areas, including photonics, magnetics, thermoelectrics, catalysis, separations, and sensing. Future work may include fabricating new types of functional meshes, sphere arrays and composites by the combination of electrodeposition with other techniques (such as melt infiltration, and sol-gel hydrolysis), and investigating their novel properties.

REFERENCES

1. Possin, G. E. *Rev. Sci. Instrum.* **1970**, *41*, 772.

2. Williams, W. D.; Giordano, N. *Rev. Sci. Instrum.* **1984**, *55*, 410.

3. Penner, R. M.; Martin, C. R. *Anal. Chem.* **1987**, *59*, 2625.

4. Brumlik, C. J.; Martin, C. R. *J. Am. Chem. Soc.* **1991**, *113*, 3174.

5. Martin, C. R. *Science* **1994**, *266*, 1961.

6. Martin, C. R.; *Chem. Mater.* **1996**, *8*, 1739.

7. Klein, J. D.; Herrick, R. D.; Palmer, D.; Sailor, M. J.; Brumlik, C. J.; Martin, C. R. *Chem. Mater.* **1993**, *5*, 902.

8. Roxlo, B.; Deckman, H. W.; Gland, J.; Cameron, S. D.; Cianelli, R. *Science* **1987**, *235*, 1629.

9. Wu, C. G.; Bein, T. *Science* **1994**, *264*, 1757.

10. Schmid, G.; Bäumle, M.; Heim, I.; Kröll, M.; Müller, F.; and Sawitowski, T. *J. Cluster Sci.* **1999**, *10*, 223.

11. Tonucci, R. J.; Justus, B. L.; Campillo, A. J.; Ford, C. E. *Science* **1992**, *258*, 783.

12. Wu, C. G.; Bein, T. *Science* **1994**, *266*, 1013.

13. Yang, H.; Shi, Q.; Tian, B.; Lu, Q.; Gao, F.; Xie, S.; Fan, J.; Yu, C.; Tu, B.; Zhao, D. *J. Am. Chem. Soc.* **2003**, *125*, 4724.

14. Favier, F.; Walter, E. C.; Zach, M. P.; Benter, T.; Penner, R. M. *Science* **2001**, *293*, 2227.

15. Velev, O. D.; Kaler, E. W. *Adv. Mater.* **2000**, *12*, 531.

16. Xia, Y.; Gates, B.; Ying, Y.; Lu, Y. *Adv. Mater.* **2000**, *12*, 693.

17. Kulinowski, K. M.; Jiang, P.; Vaswani, H.; Colvin, V. L. *Adv. Mater.* **2000**, *12*, 833.

18. Velev, O. D.; Lenhoff, A. M. *Curr. Opin. Colloid In.* **2000**, *5*, 56.

19. Stein, A. *Micropor. Mesopor. Mat.* **2001**, *44*, 227.

20. Stein, A.; Schroden, R. C. *Curr. Opin. Solid. St. M.* **2001**, *5*, 553.

21. Colvin, V. L. *MRS Bull.* **2001**, *26*, 637.

22. Braun, P.V.; Wiltzius, P. *Curr. Opin. Colloid In.* **2002**, *7*, 116.

23. Lopez, C. *Adv. Mater.* **2003**, *15*, 1679.

24. Reynolds, A. L. *http://www.elec.gla.ac.uk/groups/opto/photoniccrystal/*.

25. Zakhidov, A. A.; Baughman, R. H.; Iqbal, Z.; Cui, C.; Khayrullin, I.; Dantas, S.O.; Marti, J.; Ralchenko, V. G. *Science* **1998**, *282*, 897.

26. Hall, N.; Ozin, G. *Chem. Comm.* **2003**, 2639.

27. *Microscopy & Histology Catalog*, Polysciences, Warrington, PA **1993**-**1994**.

28. Stöber, W.; Fink, A.; Bohn, E. *J. Colloid Interface Sci.* **1968**, *26*, 62.

29. Candau, F.; Ottewill, R. H. *An Introduction to Polymer Colloids*, Kluwer, Dordrecht, the Netherlands, **1990**.

30. Holland, B. T.; Blanford, C. F.; Do, T.; Stein, A. *Chem. Mater.* **1999**, *11*, 795.

31. Reese, C. E.; Guerrero, C. D.; Weissman, J. M.; Lee, K.; Asher, S. A. *J. Colloid Interface Sci.* **2000**, *232*, 76.

32. Dinsmore, A. D.; Crocker, J. C.; Yodh, A. G. *Curr. Opin. Colloid In.* **1998**, *3*, 5.

33. Ruhl, T; Spahn, P; Hellmann, G. P. *Polymer* **2003**, *44*, 7625.

34. Mayoral, R.; Requena, J.; Moya, J. S.; Lopez, C.; Cintas, A.; Miguez, H.; Meseguer, F.; Vazquez, L.; Holgado, M.; Blanco, A. *Adv. Mater.* **1997**, *9*, 257.

35. Miguez, H.; Meseguer, F.; Lopez, C.; Blanco, A.; Moya, J. S.; Requena, J.; Mifsud, A.; Fornes, V. *Adv. Mater.* **1998**, *10*, 480.

36. Miguez, H.; Meseguer, F.; Lopez, C.; Mifsud, A.; Moya, J. S., Vazquez, L. *Langmuir* **1997**, *13*, 6009.

37. Davis, K. E.; Russel, W. B.; Glantschnig, W. J. *J. Chem. Soc. Faraday Trans.* **1991**, *87*, 411.

38. Jiang, P.; Bertone, J. F.; Hwang, K. S.; Colvin, V. L. *Chem. Mater.* **1999**, *11*, 2132.

39. Balakirev, V. G.; Bogomolov, V. N.; Zhuravlev, V. V.; Kumzerov, Y. A.; Petranovskii, V. P.; Romanov, S. G.; Samoilovich, L. A. *Kristallografiya* **1993**, *38*, 111.

40. Yan, H. W.; Blanford, C. F.; Holland, B. T.; Smyrl, W. H.; Stein, A. *Chem. Mater.* **2000**, *12*, 1134.

41. Woodcock, L. V. *Nature* **1997**, *385*, 141.

42. Woodcock, L. V. *Nature* **1997**, *388*, 236.

43. Hammond, C. *The Basics of Crystallography and Diffraction*, 2nd edition, Oxford Publishing, **2001**, Chapter 1.

44. Verma, A. R.; Krishna, P. *Polymorphism and Polytypism in Crystals*, John Wiley & Sons Publishing, **1966**, Chapter 4.

45. West, A. R. *Basic Solid State Chemistry*, John Wiley & Sons Publishing, **1988**, Chapter 1.

46. Baughman, R. H.; Zakhidov, A. A. *Proc. AMRI/Industry Symp.* **1999**, 232.

47. Xu, L.; Zhou, W. L.; Frommen, C.; Baughman, R. H.; Zakhidov, A. A.; Malkinski, L.; Wang, J.-Q.; Wiley, J. B. *Chem. Commun.* **2000**, 997.

48. Wijnhoven, J. E. G. J.; Zevenhuizen, S. J. M.; Hendriks, M. A.; Vanmaekelbergh, D.; Kelly, J. J.; Vos, W. L. *Adv. Mater.* **2000**, *12*, 888.

49. Bartlett, P. N.; Birkin, P. R.; Ghanem, M. A. *Chem. Commun.* **2000**, 1671.

50. Bartlett, P. N.; Baumberg, J. J.; Birkin, P. R.; Ghanem, M. A.; Netti, M. C. *Chem. Mater.* **2002**, *14*, 2199.

51. Sumida, T.; Wada, Y.; Kitamura, T.; Yanagida, S. *Langmuir* **2002**, *18*, 3886.

52. Bartlett, P. N.; Ghanem, M. A.; El Hallag, I. S.; de Groot, P.; Zhukov, A. *J. Mater. Chem.* **2003**, *13*, 2596.

53. Braun, P. V.; Wiltzius, P. *Nature* **1999**, *402*, 603.

54. Braun, P. V.; Wiltzius, P. *Adv. Mater.* **2001**, *13*, 482.

55. Sumida, T.; Wada, Y.; Kitamura, T.; Yanagida, S. *Chem. Lett.* **2001**, 38.

56. van Vugt, L. K.; van Driel, A. F.; Tjerkstra, R. W.; Bechger, L.; Vos, W. L.; Vanmaekelbergh, D.; Kelly, J. J. *Chem. Commun.* **2002**, 2054.

57. Lee, Y. C.; Kuo, T. J.; Hsu, C. J.; Su, Y. W.; Chen, C. C. *Langmuir* **2002**, *18*, 9942.

58. Bartlett, P. N.; Dunford, T.; Ghanem, M. A. *J. Mater. Chem.* **2002**, *12*, 3130.

59. Sumida, T.; Wada, Y.; Kitamura, T.; Yanagida, S. *Chem. Commun.* **2000**, 1613.

60. Bartlett, P. N.; Birkin, P. R.; Ghanem, M. A.; Toh, C. S. *J. Mater. Chem.* **2001**, *11*, 849.

61. Cassagneau, T.; Caruso, F. *Adv. Mater.* **2002**, *14*, 34.

62. Velev, O. D.; Jede, T. A.; Lobo, R. F.; Lenhoff, A. M. *Nature* **1997**, *389*, 447.

63. Velev, O. D., Jede, T. A.; Lobo, R. F.; Lenhoff, A. M. *Chem. Mater.* **1998**, *10*, 3597.

64. Holland, B. T.; Abrams, L.; Stein, A. *J. Am. Chem. Soc.* **1999**, *121*, 4308.

65. Blanford, C. F.; Schroden, R. C.; Al-Daous, M.; Stein, A. *Adv. Mater.* **2001**, *13*, 26.

66. Schroden, R. C.; Blanford, C. F.; Melde, B. J.; Johnson, B. J. S.; Stein, A. Chem. Mater. **2001**, *13*, 1074.

67. Zeng, F.; Sun, Z.; Wang, C.; Ren, B.; Liu, X.; Tong, Z. *Langmuir* **2002**, *18*, 9116.

68. Miguez, H.; Meseguer, F.; Lopez, C.; Holgado, M.; Andreasen, G.; Mifsud, A.; Fornes, V. *Langmuir* **2000**, *16*, 4405.

69. Imhof, A.; Pine, D. J. *Nature* **1997**, *389*, 948.

70. Holland, B. T.; Blanford, C. F.; Stein, A. *Science* **1998**, *281*, 538.

71. Wijnhoven, J. E.; Vos, W. L. *Science* **1998**, *281*, 802.

72. Yang, P.; Deng, T.; Zhao, D.; Feng, P.; Pine, D.; Chmelka, B. F.; Whitesides, G. M.; Stucky, G. D. *Science* **1998**, *282*, 2244.

73. Richel, A.; Johnson, N. P.; McComb, D. W. *Appl. Phys. Lett.* **2000**, *76*, 1816.

74. Turner, M. E.; Trentler, T. J.; Colvin, V. L. *Adv. Mater.* **2001**, *13*, 180.

75. Yi, G. R.; Moon, J. H.; Yang, S. M. *Chem. Mater.* **2001**, *13*, 2613.

76. Blanford, C. F.; Yan, H.; Schroden, R. C.; Al-Daous, M.; Stein, A. *Adv. Mater.* **2001**, *13*, 401.

77. Wijnhoven, J. E. G. J.; Bechger, L.; Vos, W. L. *Chem. Mater.* **2001**, *13*, 4486.

78. McComb, D. W.; Treble, B. M.; Smith, C. J.; De La Rue, R. M.; Johnson, N. P. *J. Mater. Chem.* **2001**, *11*, 142.

79. Meng, Q. B.; Fu, C. H.; Einaga, Y.; Gu, Z. Z.; Fujishima, A.; Sato, O. *Chem. Mater.* **2002**, *14*, 83.

80. Kuai, S.; Badilescu, S.; Bader, G.; Bruning, R.; Hu, X.; Truong, V. V. *Adv. Mater.* **2003**, *15*, 73.

81. Dong, W.; Bongard, H. J.; Marlow, F. *Chem. Mater.* **2003**, *15*, 568.

82. Wang, D.; Rogach, A. L.; Caruso, F. *Chem. Mater.* **2003**, *15*, 2724.

83. Al-Daous, M. A.; Stein, A. *Chem. Mater.* **2003**, *15*, 2638.

84. Carbajo, M. C.; Lopez, C.; Gomez, A.; Enciso, E.; Torralvo, M. J. *J. Mater. Chem.* **2003**, *13*, 2311.

85. Scott, R. W. J.; Yang, S. M.; Chabanis, G.; Coombs, N.; Williams, D. E.; Ozin, G. A. *Adv. Mater.* **2001**, *13*, 1468.

86. Scott, R. W. J.; Yang, S. M.; Williams, D. E.; Ozin, G. A. *Chem. Comm.* **2003**, 688.

87. Zhang, Y. G.; Lei, Z. B.; Li, J. M.; Lu, S. M. *New J. Chem.* **2001**, *25*, 1118.

88. Lei, Z. B.; Li, J. M.; Zhang, Y. G.; Lu, S. M. *J. Mater. Chem.* **2000**, *10*, 2629.

89. Gundiah, G.; Rao, C. N. R. *Solid State Sci.* **2000**, *2*, 877.

90. Li, B.; Zhou, J.; Hao, L. F.; Hu, W.; Zong, R. L.; Cai, M. M.; Fu, M.; Gui, Z. L.; Li, L. T.; Li, Q. *Appl. Phys. Lett.* **2003**, *82*, 3617.

91. Park, S. H.; Xia, Y. *Chem. Mater.* **1998**, *10*, 1745.

92. Park, S. H.; Xia, Y. *Adv. Mater.* **1998**, *10*, 1045.

93. Gates, B.; Yin, Y.; Xia, Y. *Chem. Mater.* **1999**, *11*, 2827.

94. Jiang, P.; Hawang, K. S.; Mittleman, D. M.; Bertone, J. F.; Colvin, V. L. *J. Am. Chem. Soc.* **1999**, *121*, 11630.

95. Johnson, S. A.; Ollivier, P. J.; Mallouk, T. E. *Science* **1999**, *283*, 963.

96. Yi, D. K.; Kim, D. Y. *Nano Lett.* **2003**, *3*, 207.

97. Xu, L. B.; Tung, L. D.; Spinu, L.; Zakhidov, A. A.; Baughman, R. H.; Wiley, J. B. *Adv. Mater.* **2003**, *15*, 1562.

98. Qian, W.; Gu, Z. Z.; Fujishima, A.; Sato, O. *Langmuir* **2002**, *18*, 4526.

99. Deutsch, M.; Vlasov, Y. A.; Norris, D. J. *Adv. Mater.* **2000**, *12*, 1176.

100. Miguez, H.; Meseguer, F.; Lopez, C.; Lopez-Tejeira, F. ; Sanchez-Dehesa, J. *Adv. Mater.* **2001**, *13*, 393.

101. Muller, M.; Zentel, R.; Maka, T.; Romanov, S. G.; Torres, C. M. S. *Adv. Mater.* **2000**, *12*, 1499.

102. Romanov, S. G.; Maka, T.; Torres, C. M. S.; Muller, M.; Zentel, R. *Synth. Metals* **2001**, *116*, 475.

103. Feng, M.; Puddephatt, R. J. *Chem. Mater.* **2003**, *15*, 2696.

104. Blanco, A.; Chomski, E.; Grabtchak, S.; Ibisate, M.; John, S.; Leonard, S. W.; Lopez, C.; Meseguer, F.; Miguez, H.; Mondia, J. P.; Ozin, G. A.; Toader, O.; van Driel, H. M. *Nature* **2000**, *405*, 437.

105. Vlasov, Y. A.; Bo, X. Z.; Sturm, J. C.; Norris, D. J. *Nature* **2001**, *414*, 289.

106. Miguez, H.; Tetreault, N.; Yang, S. M.; Kitaev, V.; Ozin, G. A. *Adv. Mater.* **2003**, *15*, 597.

107. Miguez, H.; Chomski, E.; Garcia-Santamaria, F.; Ibisate, M.; John, S.; Lopez, C.; Meseguer, F.; Mondia, J. P.; Ozin, G. A.; Toader, O.; van Driel, H. M. *Adv. Mater.* **2001**, *13*, 1634.

108. Velev, O. D.; Tessier, P. M.; Lenhoff, A. M.; Kaner, E. W. *Nature* **1999**, *401*, 548.

109. Tessier, P. M.; Velev, O. D.; Kalambur, A. T.; Lenhoff, A. M.; Rabolt, J. F.; Kaler, E. W. *Adv. Mater.* **2001**, *13*, 396.

110. Liang, Z.; Susha, A. S.; Caruso, F. *Adv. Mater.* **2002**, *14*, 1160.

111. Vlasov, Y. A.; Yao, N.; Norris, D. J. *Adv. Mater.* **1999**, *11*, 165.

112. Subramanian, G.; Manoharan, V. N.; Thorne, J. D.; Pine, D. J. *Adv. Mater.* **1999**, *11*, 1261.

113. Yan, H.; Blanford, C. F.; Holland, B. T.; Parent, M.; Smyrl, W. H.; Stein, A. *Adv. Mater.* **1999**, *11*, 1003.

114. Yan, H.; Blanford, C. F.; Holland, B. T.; Smyrl, W. H.; Stein, A. *Chem. Mater.* **2000**, *12*, 1134.

115. Juarez, B. H.; Rubio, S.; Sanchez-Dehesa, J.; Lopez, C. *Adv. Mater.* **2002**, *14*, 1486.

116. Jiang, P.; Cizeron, J.; Bertone, J. F.; Colvin, V. L. *J. Am. Chem. Soc.* **1999**, *121*, 7957.

117. Lei, Z. B.; Zhang, Y. G.; Wang, H.; Ke, Y. X.; Li, J. M.; Li, F. Q.; Xing, J. Y. *J. Mater. Chem.* **2001**, *11*, 1975.

118. Yu, J. S.; Yoon, S. B.; Chai, G. S. *Carbon* **2001**, *39*, 1421.

119. Yu, J. S.; Kang, S.; Yoon, S. B.; Chai, G. *J. Am. Chem. Soc.* **2002**, *124*, 9382.

120. Kang, S.; Yu, J. S.; Kruk, M.; Jaroniec, M. *Chem. Commun.* **2002**, 1670.

121. Baumann, T. F.; Satcher, J. H. *Chem. Mater.* **2003**, *15*, 3745.

122. Zakhidov, A. A.; Baughman, R. H.; Khayrullin, I. I.; Udod, I.; Kozlov, M.; Eradat, N.; Vardeny, Z. V.; Sigalas, M.; Biswas, R. *Synth. Metals* **2001**, *116*, 419.

123. Eradat, N.; Huang, J. D.; Vardeny, Z. V.; Zakhidov, A. A.; Khayrullin, I. I.; Udod, I.; Baughman, R. H.; *Synth. Metals* **2001**, *116*, 501.

124. Gupta, A.; Ganin, A. Y.; Sharma, P.; Agnihotri, V.; Belova, L. M.; Rao, K. V.; Kozlov, M. E.; Zakhidov, A. A.; Baughman, R. H. *Pramana-J. Phys.* **2002**, *58*, 1051.

125. Egan, G. L.; Yu, J. S.; Kim, C. H.; Lee, S. J.; Schaak, R. E.; Mallouk, T. E. *Adv. Mater.* **2000**, *12*, 1040.

126. Chen, F.; Xia, C.; Liu, M. *Chem. Lett.* **2001**, 1032.

127. Xu, L.; Zhou, W.; Kozlov, M. E.; Khayrullin, I. I.; Udod, I.; Zakhidov, A. A.; Baughman, R. H.; Wiley, J. B. *J. Am. Chem. Soc.* **2001**, *123*, 763.

128. Xu, L.; Zhou, W. L.; Baughman, R. H.; Zakhidov, A. A.; Wiley, J. B. *Mat. Res. Soc. Symp. Proc.* **2001**, *636*, D9.16.1.

129. Yan, H.; Blanford, C. F.; Lytle, J. C.; Carter, C. B.; Smyrl, W. H.; Stein, A. *Chem. Mater.* **2001**, *13*, 4314.

130. Yan, H.; Blanford, C. F.; Smyrl, W. H.; Stein, A. *Chem. Comm.* **2000**, 1477.

131. Gu, Z. Z.; Hayami, S.; Kubo, S.; Meng, Q. B.; Einaga, Y.; Tryk, D. A.; Fujishima, A.; Sato, O. *J. Am. Chem. Soc.* **2001**, *123*, 175.

132. Lei, Z.; Li, J.; Ke, Y.; Zhang, Y.; Wang, H.; He, G. *J. Mater. Chem.* **2001**, *11*, 1778.

133. Luo, G.; Liu, Z. J.; Li, L.; Xie, S. H.; Kong, J. L.; Zhao, D. Y. *Adv. Mater.* **2001**, *13*, 286.

134. Rugge, A.; Becker, J. S.; Gordon, R. G.; Tolbert, S. H. *Nano. Lett.* **2003**, *3*, 1293.

135. Yang, S. M.; Coombs, N.; Ozin, G. A. *Adv. Mater.* **2000**, *12*, 1940.

136. Jiang, P.; Bertone, J. F.; Colvin, V. L. *Science* **2001**, *291*, 453.

137. Yablonovitch, E. *Phys. Rev. Lett.* **1987**, *58*, 2059.

138. John, S. *Phys. Rev. Lett.* **1987**, *58*, 2486.

139. Joannopoulos, J. D.; Meade, R. D.; Winn, J. N. *Photonic Crystals: Molding the Flow of Light*, Princeton University Press, **1995**.

140. Krauss, T. F.; De La Rue R. M. *Prog. Quant. Electron.* **1999**, *2*, 51.

141. Berger, V. *Curr. Opin. Solid. St. M.* **1999**, *4*, 209.

142. Yablonovitch, E. *Sci. Am.* **2001**, *285*, 46.

143. Busch, K.; John, S. *Phys. Rev. E* **1998**, *58*, 3896.

144. Zhukov, A. A.; Goncharov, A. V.; de Groot, P. A. J.; Bartlett, P. N.; Ghanem, M. A. *J. Appl. Phys.* **2003**, *93*, 7322.

145. Meiklejohn, W. H.; Bean, C. P. *Phys. Rev.* **1956**, *102*, 1413.

146. Krivorotov, I. N.; Yan, H. W.; Dahlberg, E. D.; Stein, A. *J. Magn. Magn. Mater.* **2001**, *226*, 1800.

147. Yin, J. S.; Wang, Z. L. *Adv. Mater.* **1999**, *11*, 469.

148. Zhou, Y.; Antonietti, M. *Chem. Comm.* **2003**, 2564.

149. Lee, Y. J.; Braun, P. V. *Adv. Mater.* **2003**, *15*, 563.

150. Yan, H. W.; Sokolov, S.; Lytle, J. C.; Stein, A.; Zhang, F.; Smyrl, W. H. *J. Electrochem. Soc.* **2003**, *150*, A1102.

151. Nishimura, S.; Abrams, N.; Lewis, B. A.; Halaoui, L. I.; Mallouk, T. E.; Benkstein, K. D.; van de Lagemaat, J.; Frank, A. J. *J. Am. Chem. Soc.* **2003**, *125*, 6306.

152. Baughman, R. H.; Zakhidov, A. A.; Khayrullin, I. I.; Udod, I. A.; Cui, C.; Sumanasekera, G. U.; Grigorian, L.; Eklund, P. C.; Browning, V.; Ehrlich, A. *Proc. Intl. Conf. Thermoelectrics* **1998**, Nagoya, Japan.

153. Sievenpiper, D. F.; Sickmiller, M. E.; Yablonovitch, E. *Phys. Rev. Lett.*, **1996**, *76*, 2480.

154. Sievenpiper, D. F.; Yablonovich, E.; Winn, J. N.; Fan, S.; Villeneuve, P. R.; Joannopoulos, J. D. *Phys. Rev. Lett.*, **1998**, *80*, 2829.

155. El-Kady, I.; Sigalas, M. M.; Biswas, R.; Ho, K. M.; Soukoulis, C. M. *Phys. Rev. B* **2000**, *62*, 15299.

156. Fleming, J. G., Lin, S. Y.; El-Kady, I.; Biswas, R.; Ho, K. M. *Nature* **2002**, *417*, 52.

157. Li, Z. Y.; El-Kady, I.; Ho, K. M.; Lin, S. Y.; Fleming, J. G. *J. Appl. Phys.* **2003**, *93*, 38.

158. Lin, S. Y.; Moreno, J.; Fleming, J. G. *Appl. Phys. Lett.* **2003**, *83*, 380.

159. Zheng, M.; Yu, M.; Liu, Y.; Skomski, R.; Liou, S. H.; Sellmyer, D. J.; Petryakov, V. N.; Verevkin, Yu. K.; Polushkin, N. I.; Salashchenko, N. N. *Appl. Phys. Lett.* **2001**, *79*, 2606.

160. Attard, G. S.; Bartlett, P. N.; Coleman, N. R. B.; Elliott, J. M.; Owen, J. R.; Wang, J. H. *Science* **1997**, *278*, 838.

161. Tessier, P. M., Velev, O. D.; Kalambur, A. T.; Rabolt, J.; Lenhoff, A. M.; Kaler, E. W. *J. Am. Chem. Soc.* **2000**, *122*, 9554.

162. Zhou, W. L.; Xu, L.; Zakhidov, A. A.; Baughman, R. H.; Wiley, J. B. *Mat. Res. Soc. Symp. Proc.* **2002**, *703*, V9.19.1.

163. Lellig, C.; Hartl, W.; Wagner, J.; Hempelmann, R. *Angew. Chem. Int. Edit.* **2002**, *41*, 102.

164. Deniskina, N. D.; Kalinin, D. V.; Kazantseva, L. K. *Gem Quality Opals: Synthetic and Natural Genesis*, Nauka, Novosibirsk, **1988** (in Russian).

165. Philipse, A. P. *J. Mater. Sci. Lett.* **1989**, *8*, 1371.

166. Darragh, P. J.; Gaskin, A. J.; Sanders, J. V. *Sci. Am.* **1976**, *234*, 84.

167. Cao, H. Q.; Tie, C. Y.; Xu, Z.; Hong, J. M.; Sang, H. *Appl. Phys. Lett.* **2001**, *78*, 1592.

168. Bao, J. C.; Tie, C. Y.; Xu, Z.; Ma, Q.; Hong, J. M.; Sang, H., Sheng, D. *Adv. Mater.* **2002**, *14*, 44.

169. Cullity, B. D. *Introduction to Magnetic Materials*, Addison-Wesley Publishing, **1972**, 383 and the references therein.

170. Sorensen, C. M. in *Nanoscale Materials in Chemistry*, edited by Klabunde, K. J., John Wiley & Sons Publishing, **2001**, 169.

171. Fedosyuk, V.M.; Danishevskii, A. M.; Kurdyukov, D. A.; Shuman, V. B.; Gordeev, S. K. *Phys. Solid State* **2003,** *45*, 1750.

172. Makhlouf, S. A.; Parker, F. T.; Spada, F. E.; Berkowitz, A. E. *J. Appl. Phys.* **1997**, *81*, 5561.

173. Kodama, R. H.; Makhlouf, S. A.; Berkowitz, A. E. *Phys. Rev. Lett.* **1997**, *79*, 1393.

174. Ichiyanagi,Y.; Wakabayashi, N.; Yamazaki, J.; Yamada, S.; Kimishima,Y.; Komatsu, E.; Tajima, H. *Physica B* **2003**, *329*, 862.

175. Ennas, G.; Falqui, A.; Piccaluga, G.; Solinas, S.; Gatteschi, D.; Sangregorio, C.; Benedetti, A. *Z Naturforsch A* **2000**, *55*, 581.

176. Khadar, M. A.; Biju, V.; Inoue, A. *Mater. Res. Bull.* **2003**, *38*, 1341.

177. Whitney, T. M.; Jiang, J. S.; Searson, P. C.; Chien, C. L. *Science* **1993**, *261*, 1316.

178. Néel, L. *Ann. Geophys.* **1949**, *5*, 99.

179. Dormann, J. L.; D'Orazio, F.; Lucari, F.; Tronc, E.; Prene, P.; Jolivet, J. P.; Fiorani, D.; Cherkaoui, R.; Nogues, M. *Phys. Rev. B* **1996**, *53*, 14291.

180. Meier, J.; Doudin, B.; Ansermet, J. P. *J. Appl. Phys.* **1996**, *79*, 6010.

181. Fiorani, D.; Dormann, J. L.; Cherkaoui, R.; Tronc, E.; Lucari, F.; D'Orazio, F.; Spinu, L.; Nogues, M.; Garcia, A.; Testa, A. M. *J. Magn. Magn. Mater.* **1999**, *197*, 143.

182. Dormann, J. L.; Cherkaoui, R.; Spinu, L.; Nogues, M.; Lucari, F.; D'Orazio, F.; Fiorani, D.; Garcia, A.; Tronc, E.; Jolivet, J. P. *J. Magn. Magn. Mater.* **1998**, *187*, L139.

183. Sun, X. C.; Dong, X. L. *Mater. Res. Bull.* **2002**, *37*, 991.

184. Li, F.; Xu, L.; Zhou, W. L.; He, J.; Baughman, R. H.; Zakhidov, A. A.; Wiley, J. B. *Adv. Mater.* **2002**, *14*, 1528.

185. Li, Y.; Meng, G. W.; Zhang, L. D.; Phillipp, F. *Appl. Phys. Lett.* **2000**, *76*, 2011.

186. Cassagneau, T.; Caruso, F. *Adv. Mater.* **2002**, *14*, 1629.

187. Cassagneau, T.; Caruso, F. *Adv. Mater.* **2002**, *14*, 1837.

188. Tanev, P. T.; Chibwe, M.; Pinnavaia, T. J. *Nature* **1994**, *368*, 321.

189. Lewandowski, K.; Murer, P.; Svec, F. Frechet, J. M. J. *Anal. Chem.* **1998**, *70*, 1629.

190. Wang, D. Y.; Caruso, F. *Adv. Mater.* **2001**, *13*, 350.

191. Yoshino, K.; Kawagishi, Y.; Tatsuhara, S.; Kajii, H.; Lee, S.; Fujii, A.; Ozaki, M.; Zakhidov, A. A.; Vardeny, Z. V.; Ishikawa, M. *Microelectron. Eng.* **1999**, *47*, 49.

192. Jiang, P.; Bertone, J. F.; Colvin, V. L. *Science* **2001**, *291*, 453.

193. Sumioka, K.; Kayashima, H.; Tsutsui, T. *Adv. Mater.* **2002**, *14*, 1284.

194. Masuda, H.; Fukuda, K. *Science* **1995**, *268*, 1466.

195. Hoyer, P.; Baba, N.; Masuda, H. *Appl. Phys. Lett.* **1995**, *66*, 2700.

196. Hoyer, P.; Masuda, H. *J. Mater. Sci. Lett.* **1996**, *15*, 1228.

197. Hoyer, P. *Langmuir* **1996**, *12*, 1411.

198. Yang, S. M.; Coombs, N.; Ozin, G. A. *Adv. Mater.* **2000**, *12*, 1940.

199. Rengarajan, R.; Jiang, P.; Colvin, V.; Mittleman, D. *Appl. Phys. Lett.* **2000**, *77*, 3517.

200. Scott, R. W. J.; Yang, S. M.; Coombs, N.; Ozin, G. A.; Williams, D. E. *Adv. Funct. Mater.* **2003**, *13*, 225.

201. Lei, Z. B.; Li, J. M.; Ke, Y. X.; Zhang, Y. G.; Zhang, H. C.; Li, F. Q.; Xing, J. Y. *J. Mater. Chem.* **2001**, *11*, 2930.

202. Lei, Z. B.; Zhang, H. C.; Ma, S. H.; Ke, Y. X.; Li, J. M.; Li, F. Q. *Chem. Commun.* **2002**, 676.

203. Kim, Y. N.; Chi, E. O.; Kim, J. C.; Lee, E. K.; Hur, N. H., *Solid State Commun.* **2003**, *128*, 339.

204. Yi, G. R.; Moon, J. H.; Manoharan, V. N.; Pine, D. J.; Yang, S. M. *J. Am. Chem. Soc.* **2002**, *124*, 13354.

205. Xu, L.; Zakhidov, A. A.; Baughman, R. H.; Wiley, J. B. *Mat. Res. Soc. Symp. Proc.* **2004**, *EXS-2*, M5.17.1.

206. Sun, S.; Murray, C. B.; Weller, D.; Folks, L.; Moser, A. *Science* **2000**, *287*, 1989.

207. Fraune, M.; Rudiger, U.; Guntherodt, G.; Cardoso S.; Freitas, P. *Appl. Phys. Lett.* **2000**, *77*, 3815.

208. Zhong, Z.; Yin, Y.; Gates, B.; Xia, Y. *Adv. Mater.* **2000**, *12*, 206.

209. Lederman, M.; O'Barr, R.; Schultz, S. *IEEE Trans. Magn.* **1995**, *31*, 3793.

210. Gau, J. S.; Brucker, C. F. *J. Appl. Phys.* **1985**, *57*, 3988.

211. Gau, J. S.; Yetter, W. E. *J. Appl. Phys.* **1987**, *61*, 3807.

212. Wan, H.; Hadjipanayis, G. C. *J. Appl. Phys.* **1991**, *70*, 6059.

213. Victora, R. H. *Phys. Rev. Lett.* **1987**, *58*, 1788.

214. Sun, L.; Searson, P. C.; Chien, C. L. *Appl. Phys. Lett.* **2001**, *79*, 4429.

215. Han, G. C.; Zong, B. Y.; Luo, P.; Wu, Y. H. *J. Appl. Phys.* **2003**, *93*, 9202.

216. Chikazumi, S. *Physics of magnetism*, John Wiley & Sons Publishing (New York), **1964**, 290.

217. Stoner, E. C.; Wohlfarth, E. P. *Phil. Trans. Roy. Soc. London A* **1948**, *240*, 599.

218. Bantu, A. K. M.; Rivas, J.; Zaragoza, G.; Lopez-Quintela, M. A.; Blanco, M. C. *J. Appl. Phys.* **2001**, *89*, 3393.

219. Ranjan, R.; Gau, J. S.; Amin, N. *J. Magn. Magn. Mater.* **1990**, *89*, 38.

220. Eagle, D. F.; Mallinson, J. C. *J. Appl. Phys.* **1967**, *38*, 995.

221. Liou, S. H.; Chen, C. H.; Chen, H. S.; Kortan, A. R.; Chien, C. L. *Mat. Res. Soc. Symp. Proc.* **1989**, *132*, 191.

222. Moroz, A. *Phys. Rev. Lett.* **1999**, *83*, 5274.

223. Moroz, A. *Europhys. Lett.* **2000**, *50*, 466.

224. Zhang, W. Y.; Lei, X. Y.; Wang, Z. L.; Zheng, D. G.; Tam, W. Y.; Chan, C. T.; Sheng, P. *Phys. Rev. Lett.* **2000**, *84*, 2853.

225. Wang, Z. L.; Chan, C. T.; Zhang, W. Y.; Ming, N. B.; Sheng, P. *Phys. Rev. B* **2001**, *64*, 113108.

226. Webpage: *http://www.aacg.bham.ac.uk/magnetic_materials/type.htm*.

227. Webpage: *http://hyperphysics.phy-astr.gsu.edu/hbase/solids/ferro.html#c2*.

APPENDIX A

BASIC CONCEPTS OF MAGNETISM

A.1 Classes of Magnetic Materials

The origin of magnetism lies in the orbital and spin motions of electrons and how the electrons interact with one another. The best way to introduce the different types of magnetism is to describe how materials respond to magnetic fields. The magnetic behavior of materials can be classified into the following five major groups:

Diamagnetism: Diamagnetic materials, which have no atomic magnetic moments, have no magnetization in zero field. When a field is applied a small, negative moment is induced on the diamagnetic atoms proportional to the applied field strength.

Paramagnetism: In a paramagnet the atoms have a net magnetic moment but are oriented randomly throughout the sample due to thermal agitation, giving zero magnetization. As a field is applied the moments tend towards alignment along the field, giving a net magnetization which increases with applied field as the moments become more ordered.

Ferromagnetism: Ferromagnetic materials exhibit parallel alignment of moments resulting in large net magnetization even in the absence of a magnetic field. As the temperature increases, thermal oscillation, or entropy, competes with the ferromagnetic tendency for moments to align. When the temperature rises beyond a certain point, called the Curie temperature, the system can no longer maintain a

spontaneous magnetization, although it still responds paramagnetically to an external field.

Antiferromagnetism: In materials that exhibit antiferromagnetism, the magnetic moments align in a regular pattern with neighboring moments pointing in opposite directions. This is the opposite of ferromagnetism. Generally, antiferromagnetic materials exhibit antiferromagnetism at a low temperature, and become disordered above a certain temperature; the transition temperature is called the Neel temperature. Above the Neel temperature, the material is typically paramagnetic.

Ferrimagnetism: A ferrimagnetic material is one in which the magnetic moment of the atoms on different sublattices oppose as in antiferromagnet but the opposing moments are unequal and a spontaneous magnetization remains.

Table A.1 shows summary of different types of magnetic behavior.

A.2 Magnetic Domains

Ferromagnetic materials exhibit a long-range ordering phenomenon at the atomic level which causes the unpaired electron spins to line up parallel with each other in a region called a domain. Within the domain, the magnetic field is intense, but in a bulk sample the material will usually be unmagnetized because the many domains will themselves be randomly oriented with respect to one another (Figure A.1a). A modest applied magnetic field can cause a larger degree of alignment of the magnetic moments with the external field, giving a large multiplication of the applied field. The microscopic evidence about magnetization indicates that the net magnetization of ferromagnetic materials in response to an external magnetic field may actually occur more by the growth of the domains parallel to the applied field at

Table A.1 Summary of different types of magnetic behavior. (Adapted from Ref. 226)

Type of Magnetism	Susceptibility	Atomic / Magnetic Behaviour		Example / Susceptibility
Diamagnetism	Small & negative.	Atoms have no magnetic moment		Au -2.74x10^{-6} Cu -0.77x10^{-6}
Paramagnetism	Small & positive.	Atoms have randomly oriented magnetic moments		β-Sn 0.19x10^{-6} Pt 21.04x10^{-6} Mn 66.10x10^{-6}
Ferromagnetism	Large & positive, function of applied field, microstructure dependent.	Atoms have parallel aligned magnetic moments		Fe ~100,000
Antiferromagnetism	Small & positive.	Atoms have mixed parallel and anti-parallel aligned magnetic moments		Cr 3.6x10^{-6}
Ferrimagnetism	Large & positive, function of applied field, microstructure dependent	Atoms have anti-parallel aligned magnetic moments		Ba ferrite ~3
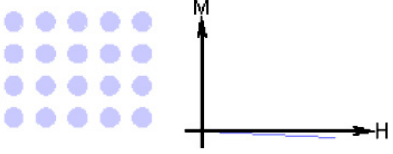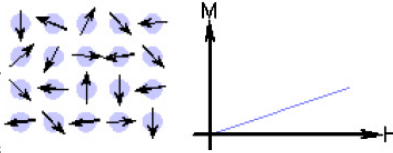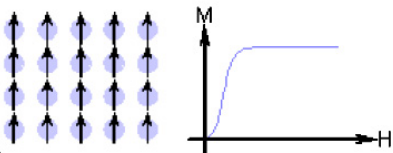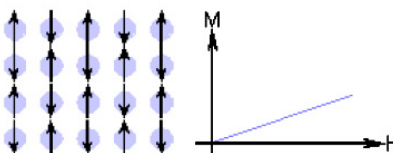
a)

In bulk material the domains usually cancel, leaving the material unmagnetized.

Externally applied magnetic field.

Iron will become magnetized in the direction of any applied magnetic field. This magnetization will produce a magnetic pole in the iron opposite to that pole which is nearest to it, so the iron will be attracted to either pole of a magnet.

b)

$B_{external} = 0$

$B_{external}$

$B_{external}$

No external field

Weak applied field

Strong applied field

Figure A.1 a) Illustration of orientation of the domains with and without external fields, b) sketch of growth of the domains under zero, weak and strong external fields. (Adapted from Ref. 227)

the expense of other domains (Figure A.1b) rather than the reorientation of the domains themselves as implied in the Figure A.1a.

A.3 Magnetic Hysteresis

When a ferromagnetic material is magnetized by an increasing applied field and then the field is decreased, the magnetization does not follow the initial magnetization curve obtained during the increase. This irreversibility is called hysteresis. An example of a full or major (i.e., M is taken to near M_s) hysteresis curve (or loop) is given is Figure A.2. At extremely high applied fields, the magnetization approaches the saturation magnetization, M_s. Then if the field is decreased to zero, the M verse H curve does not follow the initial curve but instead lags behind until, when $H = 0$ again, a remanent magnetization remains, the remanence M_r. If the field is now applied in the reverse direction (a negative field), M is forced to zero at a field magnitude called the coercivity, H_c. Increasing this negative field still further forces the magnetization to saturation in the negative direction. Symmetric behavior of this hysteresis curve is obtained as H is varied widely between large positive and negative values.

A.4 Magnetic Anisotropy

In many situations the susceptibility of a material will depend on the direction in which it is measured. Such a situation is called magnetic anisotropy. When magnetic anisotropy exists, the total magnetization of a ferromagnet M_s will prefer to lie along a special direction called the easy axis. Cystalline anisotropy and shape anisotropy are two types of important and common sources of anisotropy.
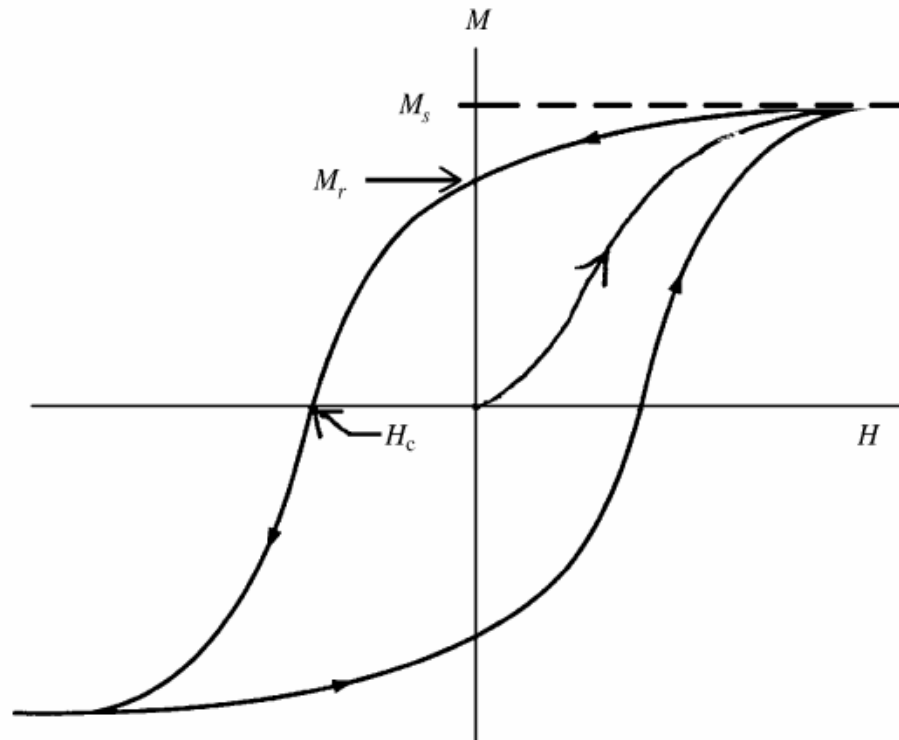
Figure A.2 A full-loop hysteresis curve. M_s is the saturation magnetization, M_r is the magnetization remanence (at $H = 0$), and H_c is the coercivity. (Adapted from Ref. 170)

Cystalline anisotropy: Cystalline anisotropy is an intrinsic property of a ferromagnet, independent of grain size and shape. In can be most easily seen by measuring magnetization curves along different crystal directions. Depending on the crystallographic orientation of the sample in the magnetic field, the magnetization reaches saturation in different fields. Crystalline anisotropy energy is the energy necessary to deflect the magnetic moment in a single crystal from the easy to the hard direction. The easy and hard directions arise from the interaction of the spin magnetic moment with the crystal lattice (spin-orbit coupling).

Shape anisotropy: This type of anisotropy is due to the shape of a magnetic grain. A magnetized body will produce magnetic charges or poles at the surface. This surface charge distribution, acting in isolation, is itself another source of a magnetic field, called the demagnetizing field. It is called the demagnetizing field because it acts in opposition to the magnetization that produces it. For a nonspherical piece of material, the demagnetizing field will be less if the magnetization is along the long axis than if is along one of the short axes. This produces an easy axis of magnetization along the long axis. A sphere, on the other hand, has no shape anisotropy.

A.5 Small Particle Magnetism

A.5.1 Superparamagnetism

Superparamagnetism is a phenomenon by which magnetic materials may exhibit a behavior similar to paramagnetism at temperatures below the Curie temperature.

Normally, coupling forces in magnetic materials cause the magnetic moments of neighboring atoms to align, resulting in very large internal magnetic fields. At temperatures above the Curie temperature, the thermal energy is sufficient to

overcome the coupling forces, causing the atomic magnetic moments to fluctuate randomly. Because there is no longer any magnetic order, the internal magnetic field no longer exists and the material exhibits paramagnetic behavior.

Superparamagnetism occurs when the material is composed of small particles. In this case even though the temperature is below the Curie temperature and the thermal energy is not sufficient to overcome the coupling forces between neighboring atoms, the thermal energy is sufficient to change the direction of magnetization of the entire particle. The resulting fluctuations in the direction of magnetization cause the magnetic field to average to zero. The material behaves in a manner similar to paramagnetism, except that instead of each individual atom being independently influenced by an external magnetic field, the magnetic moment of the entire particle tends to align with the magnetic field.

The energy required to change the direction of magnetization of a particle is called the anisotropy energy and depends both on the material properties and the particle size. As the particle size decreases, so does the anisotropy energy, resulting in a decrease in the so-called blocking temperature T_B, at which the material becomes superparamagnetic.

The blocking temperature can be easily measured with a magnetometer. The procedure is to cool the sample under zero applied field, so-called zero-field-cooled (ZFC), to a temperature well below T_B. Then apply a field (e.g. 100 Oe). If $T < T_B$, the individual particle's moments are bound to the particles, point in random directions, and will not be very susceptible, so the induced magnetization will be small. The system is then warmed at a uniform dT/dt. As T approaches T_B from below, the thermal ennergy will begin to loosen up the moments from the particles and induced M will rise. At T_B, the moments are unblocked and hence are free to align

with the applied field to yield a large total M. As T increases above T_B, M falls via the Curie law, M ~ 1/T because the system is a (super)paramagnet.

A.5.2 Coercivity of Small Particles

The coercivity of small ferromagnetic particles (e.g., 1 µm or less) has a striking dependence on their size. As the particle size is reduced, it is typically found that the coercivity increases, goes through a maximum, and then tends toward zero. Figure A.3 shows the schematic of the variation of coercivity with particle diameter D. Beginning at large sizes, the following regions can be distinguished:

Multidomain: For most, but not all, materials the size dependence of the coercivity is experimentally found to be given approximately by

$$H_c = a + \frac{b}{D} \tag{A.1}$$

where a and b are constants.

Single-domain: Below a critical diameter D_s, the particle become single domain, and in this size range the coercivity reaches a maximum. As the particle size decreases below D_s the coercivity decreases, because of thermal effects. Below a critical diameter D_{sp} the coercivity is zero, again because of thermal effects, which are now strong enough to spontaneously demagnetize a previously saturated assembly of particles. Such particles are called superparamagnetic.

The magnetic hardness of most small particles is due to the forces of shape and/or crystalline anisotropy. When shape anisotropy prevails, the coercivity decreases as packing fraction *p* (defined as the volume fraction of magnetic particles in the assembly) because of particle interaction. On the other hand, when crystalline anisotropy prevails, the coercivity is independent of *p*.
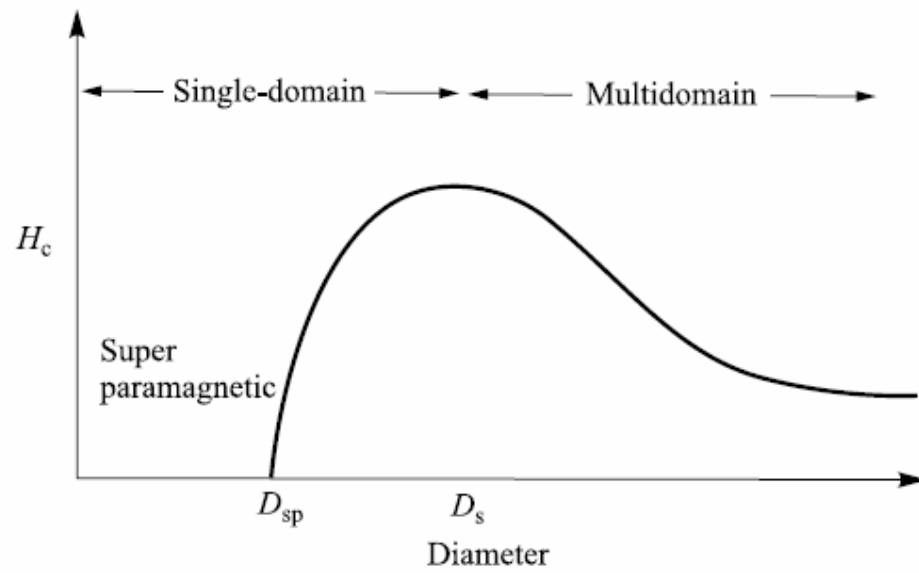
Figure A.3 Particle coercivity verse size (~ diameter). D_{sp} is the superparamagnetic size; D_s is the single-domain size. (Adapted from Ref. 170)

VITA

Lianbin Xu was born in Hubei, China in November 1970. He obtained his B. S. in Chemistry from Nankai University in 1991 and M. S. in Inorganic Chemistry from Peking University in 1994. Then he worked as a research assistant professor at the Institute of Photographic Chemistry, Chinese Academy of Sciences until the end of 1998. In 1999, he came to University of New Orleans as a graduate student and joined Professor John B. Wiley's solid state and materials group in the Chemistry Department.